

**Investigation into the thermal dehydroxylation and decomposition of
hydroxylapatite during atmospheric plasma spraying:
NMR and Raman spectroscopic study of as-sprayed coatings and coatings
incubated in simulated body fluid**

Von der Fakultät für Geowissenschaften, Geotechnik und Bergbau
der Technischen Universität Bergakademie Freiberg
genehmigte

DISSERTATION

Zur Erlangung des akademischen Grades
Doctor rerum naturalium
Dr.rer.nat.

vorgelegt

von Dipl.-Ing. Thi Hong Van TRAN
geboren am 16 Juli 1970 in Hanoi, Vietnam

Gutachter: Prof.Dr. Robert B. Heimann, Freiberg
Prof.Dr. Berthold Thomas, Freiberg
Dr. Georg Berger, BAM Berlin

Tag der Verleihung: 11.Feb.2005

Table of content

	page
Abbreviations	iii
Preface	1
Zusammenfassung	2
1. State-of-the-art of biomaterials	3
1.1. Biomaterials	3
1.2. Bioconductive ceramic materials	4
1.3. Calcium phosphates	5
1.3.1. Tricalcium phosphate	6
1.3.2. Tetra calcium phosphate	8
1.3.3. Hydroxylapatite	8
1.3.3.1. Crystal structure of hydroxylapatite	8
1.3.3.2. Thermal stability of hydroxylapatite	10
1.3.3.3. Non-stoichiometry of hydroxylapatite	11
1.4. Hydroxylapatite coatings	12
1.4.1. Plasma spraying technique	12
1.4.2. Plasma-sprayed hydroxylapatite coatings	15
1.4.3. <i>In-vitro</i> and <i>in-vivo</i> behaviour of hydroxylapatite coatings	16
1.4.4. Bond coat for hydroxylapatite coatings	20
1.5. Brief summary of literature study	22
2. Materials and investigation methods	22
2.1. Materials	22
2.1.1. Hydroxylapatite for bioconductive coatings	22
2.1.2. Titanium dioxide as a bond coat	23
2.1.3. Titanium alloy Ti-6Al-4V as a substrate	23
2.2. Preparation of coatings	24
2.2.1. Atmospheric plasma spraying	24
2.2.2. Incubation of coatings	25
2.2.3. Thermal post-treatment of coatings	26
2.3. Description of analytical methods	26
2.3.1. Nuclear magnetic resonance spectroscopy	26
2.3.2. Laser Raman microspectroscopy	30

2.3.3.	X-ray diffraction analysis	31
2.3.4.	Thermal analysis - Thermogravimetry	32
2.3.5.	Scanning electron microscopy, energy dispersive X-ray analysis	33
2.3.6.	Cathodoluminescence	34
3.	Results and discussion	35
3.1.	Structural analysis of as-sprayed and incubated coatings by NMR spectroscopy	36
3.2.	Characterization of coating surfaces by Raman spectroscopy	45
3.3.	Investigation of phases in coatings	53
3.4.	Differentiation between coating surface and coating boundary	57
3.5.	Changes of the coating composition and morphology during incubation	64
3.6.	Probing the behaviour of the HA coating during the incubation process by cathodoluminescence	69
3.7.	Characterization of as-sprayed coatings in cross-section	71
3.8.	Effect of thermal post-treatment on the microstructure of coatings	73
3.9.	Influence of the bond coat thickness on the coating structure	75
3.10.	Behaviour of coatings in different incubation solutions	85
4.	Conclusion	91
5.	Outlook and future work	94
6.	Acknowledgements	97
7.	References	98
8.	Curriculum vitae	113

Abbreviations

am-CP/I:	<u>a</u> morphous <u>c</u> alcium <u>p</u> hosphates caused by rapid quenching in a plasma-spray process (dry way)
am-CP/II:	<u>a</u> morphous <u>c</u> alcium <u>p</u> hosphates which form by a precipitation process (wet way)
BC	<u>B</u> ond <u>c</u> oat
Ca-def HA:	<u>C</u> alcium <u>d</u> eficient <u>h</u> ydroxylapatite
CHA	<u>C</u> arbonat <u>o</u> hydroxylapatite
CL	<u>C</u> athod <u>o</u> luminescence
CP	<u>C</u> alcium <u>p</u> hosphate
EDS	<u>E</u> nergy <u>d</u> ispersiv <u>e</u> <u>s</u> pectroscopy
EDX	<u>E</u> nergy <u>d</u> ispersiv <u>e</u> <u>X</u> -ray
HA:	<u>H</u> ydroxylapatite, $\text{Ca}_{10}(\text{PO}_4)_6(\text{OH})_2$
HETCOR	<u>H</u> eteronuclear <u>c</u> orrelation
LRS	<u>L</u> aser <u>R</u> aman <u>s</u> pectroscopy
MAS	<u>M</u> agic <u>a</u> ngle <u>s</u> pinning
NMR	<u>N</u> uclear <u>m</u> agnetic <u>r</u> esonance spectroscopy
ns- HA:	<u>n</u> on- <u>s</u> toichiometric <u>h</u> ydroxylapatite
OA	<u>O</u> xyapatite
OHA:	<u>O</u> xyhydroxylapatite, $\text{Ca}_{10}(\text{PO}_4)_6(\text{OH})_{2-2x}\text{O}_x$
R-SBF	<u>R</u> evised <u>s</u> imulated <u>b</u> ody <u>f</u> luid
SBF	<u>S</u> imulated <u>b</u> ody <u>f</u> luid
SEM	<u>S</u> canning <u>e</u> lectron <u>m</u> icroscopy
TCP:	<u>T</u> ri <u>c</u> alcium <u>p</u> hosphate, $\text{Ca}_3(\text{PO}_4)_2$
TEM	<u>T</u> ransmission <u>e</u> lectron <u>m</u> icroscopy
TG	<u>T</u> hermogravimetry
TTCP:	<u>T</u> etra <u>c</u> alcium <u>p</u> hosphate, $\text{Ca}_4(\text{PO}_4)_2\text{O}$
FWHM	<u>F</u> ull <u>w</u> idth at <u>h</u> alf <u>m</u> aximum height
XRD	<u>X</u> -ray <u>d</u> iffractometry
ΔW	Weight change

Preface

The present dissertation was completed during my PhD study within the research group of Professor Dr.R.B. Heimann at the Department of Mineralogy, TU Bergakademie Freiberg between 2001 and 2004.

Total hip replacement (THR) has been well established for many decades and used successfully in surgical application, with a high healing chance (>90%) and a long service life (≥ 15 years) /135/. The number of patients receiving these implants is increasing. Every year more than 1 million hip endoprostheses, many of them coated with bioconductive ceramics such as hydroxylapatite (HA), are being implanted worldwide. However, long-term stability still is a major problem, in particular as the number of cases showing aseptic implant loosening increase with increasing number of implantations but with some delay. Frequently bioconductive hydroxylapatite coatings will be applied by plasma-spraying to the stem of hip endoprostheses to facilitate improved implant integration. Many studies and experiments have been performed to optimize the properties of these HA coating in terms of osseointegration, phase composition, mechanical adhesion strength as well as implant lifetime. *In-vivo* investigations were also performed to show the biological response of the implant and bone ingrowth into the implant coating. It is known that chemical stability and integrating capability of the bioconductive coating are associated closely with the phase composition and microstructure of the coating. Thermal decomposition of hydroxylapatite was mostly investigated by XRD, where HA, TCP, TTCP, CaO and amorphous phases were identified. However, only few studies can be found in the literature related to structural characterization of the decomposition products and to the reconstruction of plasma-sprayed hydroxylapatite *in-vitro*. Hence, in depth knowledge of structural changes of the surface of bioconductive coatings in contact with simulated body fluid is missing up to now. The present study will apply sensitive analytical techniques such as nuclear magnetic resonance (NMR) spectroscopy and Raman spectroscopy (LRS) to as-sprayed plasma-sprayed hydroxylapatite coatings and coatings incubated in simulated body fluid and thus contribute to the improvement of biomedical knowledge.

Zusammenfassung

Hydroxylapatit (HA) wird seit etwa 30 Jahren als biokonduktives Beschichtungsmaterial für medizinische Hüftgelenks- und Zahn-Implantate verwendet. Die Beschichtung erfolgt häufig mit der Plasmaspritztechnologie. Dabei ändert sich die Struktur und die Zusammensetzung der Hydroxylapatitphase beträchtlich.

In der vorliegenden Arbeit wurden die Zusammensetzung und die Eigenschaften von plasma-gespritzten HA- Schichten nach *in-vitro* – Inkubationsversuchen untersucht. Der Mechanismus der mikrostrukturellen Umwandlung von defektem zu gut rekristallisiertem HA wurde eingehend beleuchtet. Außerdem wurde der Einfluß einer Haftvermittlerschicht auf die Struktur der HA-Schichten charakterisiert.

In den analytischen Arbeiten kamen NMR-Spektroskopie, Laser-Raman-Spektroskopie, Röntgenphasenanalyse, Rasterelektronenmikroskopie, Thermogravimetrie und Kathodolumineszenz zum Einsatz.

Folgenden wesentliche Erkenntnisse wurden erhalten:

- Das Plasmaspritzen verursacht erhebliche Änderung der HA-Struktur und die Bildung von feinen Kristallen. Unterschiedliche Calciumphosphatphasen koexistieren in den plasma-gespritzten HA- Schichten. Verschiedene lokale elektronische Protonenzustände wurden mittels NMR festgestellt. Oxyhydroxylapatit kann als Hydroxylapatit mit einer Defektstruktur betrachtet werden.
- OH⁻ - Ionen diffundieren während der *in-vitro*-Inkubation in simulierter Körperflüssigkeit aus der wässrigen Lösung in die Schichten. Als Ergebnis wird HA mit einer Defektstruktur allmählich in HA mit einer Perfektstruktur umgewandelt. Ein Haftvermittler aus TiO₂ scheint diesen Prozeß zu beschleunigen.
- Die Umstrukturierung von Defekt- HA zu gut-kristallinem HA dauert lange. Selbst nach einem *in-vitro*- Test von 24 Wochen wurde immer noch Oxyhydroxylapatit in der HA-Schicht nachgewiesen.
- Die Inkubation von plasma-gespritzten HA-Schichten in einer proteinfreien körpereigenen Lösung (simulated body fluid – SBF) ermöglicht eine Bildung von feinen knochenähnlichen Apatitkristallen auf der HA-Schichtoberfläche. Sie können vorteilhaft für die Integration des mit HA-beschichteten Implantats mit dem Knochen nach der Operation sein. Die Verwendung eines Ti_nO_{2n-1} – Haftvermittlers wirkt sich ausgesprochen positiv auf diese Bildung neuer Kristalle aus.
- Die Stärke der Haftvermittlerschicht soll 40 µm nicht überschreiten.
- Innerhalb der HA- Schicht gibt es eine deutliche Differenzierung zwischen den Phasen an der Substrat (Haftvermittler)/ HA-Schicht – Grenzfläche und den Phasen nahe der Schichtoberfläche.
- Eine thermische Nachbehandlung von HA-Schichten führt zu einer Verringerung bzw. zu einer vollständigen Beseitigung der Defektstruktur von HA. Dadurch werden biokeramischen Schichten aus Hydroxylapatit mit hoher Kristallinität erhalten. Die optimalen Behandlungsparameter ergeben sich aus den Thermogravimetrie- Daten.

1. State-of-the-art of biomaterials

1.1. Biomaterials

Biomaterials are synthetic materials used in medicine. They replace a part or a function of a living system and hence contact with living tissue and body fluid. In use, biomaterials have to fulfil several requirements. They must be safe, body acceptable and able to integrate progressively with living tissue. All those requirements are characterized by interaction at the interface between the living tissue and the biomaterial. Considering the mentioned interaction at the interface, biomaterials are classified into three groups (Tab.1) /1/:

Table 1: Classification of implant materials according to the material influenced reactions in the surrounding bony tissue.

Class of materials	Kind of influence	Tissue reaction	Typical materials in this class
Biotolerant	Ions and/or monomers go into solution, biochemical effects on differentiation and proliferation	Distance osteogenes	Stainless steels, polymethylmethacrylate (PMMA bone cement), cobalt based alloy, polyethylene
Bioinert	No matter influencing the adjacent tissue goes into solution	Contact osteogenes	Al ₂ O ₃ ceramics, carbon, titanium
Bioconductive	Bond formation by not yet completely understood processes	Bonding osteogenes	Calcium phosphate based ceramics and calcium phosphate containing glasses and glass-ceramics

In the following, the work will focus on joint replacement systems, in particular bioconductive ceramic coatings. According to their chemical compositions, materials used in joint replacement are made of metals, ceramics, polymers, or composites. A summary of these implant materials is given in Tab.2.

Table 2: Summary of materials used in total joint replacement /2/

Materials	Application
<i>Metals:</i>	
Stainless steels: 316L	Femoral stems, femoral heads.
Cobalt-based alloys:	Porous coatings, femoral stems, femoral heads, tibia components.
Cast Co-Cr-Mo Wrought Co-Ni-Cr-Mo Wrought Co-Cr-W-Ni	
<i>Titanium-based materials:</i>	
C.P.Ti	Porous coatings, 2 nd phase in composites and PMMA composites.
Ti-6Al-4V	Femoral stems, femoral heads, tibial components, porous coatings.
Ti-5Al-2.5Fe	Femoral stems, femoral heads.
Ti-6Al-7Nb	Femoral stems, femoral heads.
<i>Ceramics:</i>	
<i>Bio-inert ceramics:</i>	
Carbon	Coating on metallic femoral stems, 2 nd phase in composites and bone cement
Alumina	Femoral stems, femoral heads, acetabular cups
Zirconia*	Femoral heads
<i>Bioconductive ceramics:</i>	
Calcium phosphates	Coatings on metallic and ceramic femoral stems, scaffold materials, 2 nd phase in PMMA and UHMWPE composites
Bioglasses	Coatings on metallic and ceramic femoral stems
<i>Polymers</i>	
PMMA	Bone cement
UHMWPE/HDPE	Acetabular cups, tibial plateaus, patellar components, porous coatings on metallic femoral stems
Polysulfone	Femoral stems, porous coatings on metallic femoral stems
PTFE	Femoral stems, porous coatings on metallic femoral stems
<i>Composites</i>	
Femoral stems	
<i>Polymer-based:</i>	
Polysulfone/carbon	
Polycarbonate/carbon	
Polysulfone/Kevlar	
Polycarbonate/Kevlar	
<i>Ceramic-based:</i>	
Carbon/carbon	

* Recent results have shown that the use of zirconia as a material for femoral heads should be discouraged owing to a lack in hydrolytic stability *in-vivo*.

1.2. Bioconductive ceramic materials

Bioconductive ceramics are bioconductive glasses, glass ceramics and calcium phosphate ceramics, which have poor mechanical fatigue, but extremely high biological compatibility. When bioconductive ceramics are implanted in the body, a biochemical and biophysical reaction occurs at the interface between the implant and the tissue. After short time implantation, the bioconductive ceramics form a layer of carbonatohydroxylapatite (CHA) on their surface. The CHA phase has the same

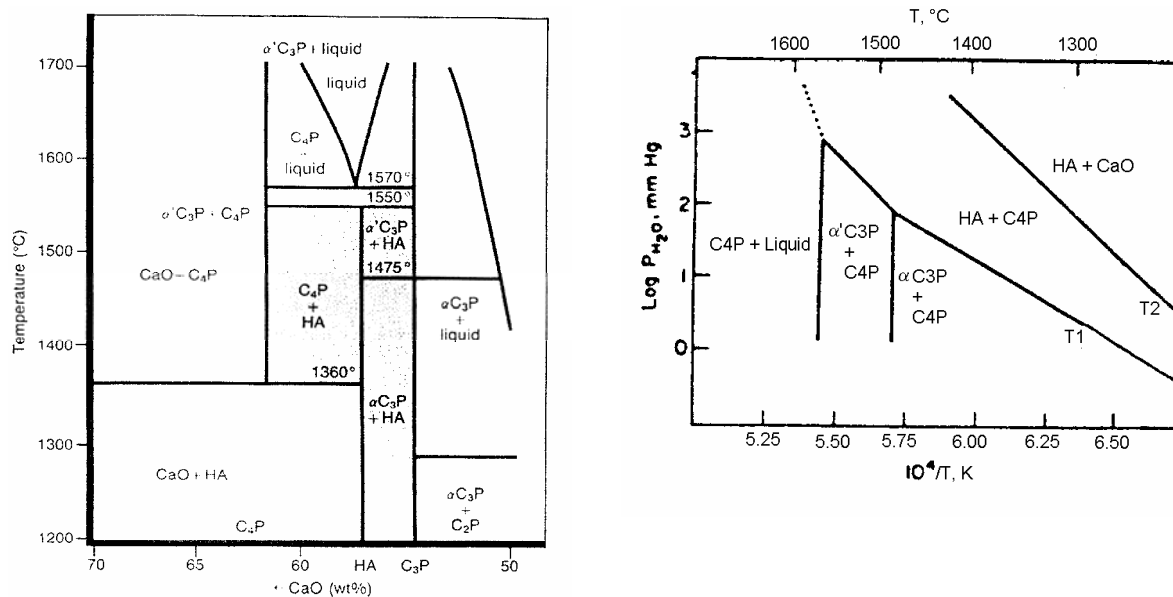
mineral structure as the mineral phase of bone and promotes steady interface bonding /3,4,5/. To overcome the mechanical limitations, bioconductive calcium phosphate ceramics are often coated onto high strength, sufficiently bioinert metal substrates such as cp-Ti and Ti6Al4V.

Bioconductive glass and glass ceramics: contain specific amounts of SiO₂, CaO, Na₂O and P₂O₅. When a bioconductive glass is incubated in a solution, Na⁺, K⁺, Ca²⁺ ions tend to leach out, leaving a silicate-rich layer at the surface of the glass. A calcium –phosphate rich, amorphous apatite layer will form on top of the silicate-rich layer and develop to hydroxylapatite crystal. Hence, the chemical composition affects the degree of activities and physiologic response of the glass *in-vivo* /2/.

Calcium phosphate ceramics: Calcium phosphate ceramics are ceramic materials with different calcium to phosphate ratios. A comprehensive overview on calcium phosphates can be found in Ref./6/. Some compounds like hydroxylapatite (HA), tricalcium phosphate (TCP) and octacalcium phosphate (or tetracalcium phosphate (TTCP)) have found wide use as bulk ceramics, granules, biocement or coatings for medical and implant applications. Since calcium phosphate is able to bond directly to bone, it is very attractive for surgical application /7,8/.

1.3. Calcium phosphates

In the system CaO-P₂O₅- (H₂O) (Fig.1), there are three stable phases: tricalcium phosphate, tetracalcium phosphate and hydroxylapatite. The temperatures T1 and T2 are dependent on the partial pressure of water vapour, as shown in Fig.1b. It is known that some transitional phases of calcium phosphates (CP) exist in aqueous systems, but their characteristics are not presented here. For detailed information, see Ref./6/.



a) Phase diagram of the system CaO-P₂O₅-(H₂O); HA: hydroxylapatite, C₃P: tricalcium phosphate, C₄P: tetracalcium phosphate /136/ and b) influence of water vapour partial pressures on the equilibrium temperatures. At temperature T1 HA exists in equilibrium with C₃P + C₄P + xH₂O. T2 separates HA + CaO from HA + C₄P /119/.

1.3.1. Tricalcium phosphate

Tricalcium phosphate has the chemical formula Ca₃(PO₄)₂. Four modifications of TCP are known. β -TCP is stable below 1125°C. Above 1125°C β -TCP converts to the high temperature phase α -TCP. α -TCP is stable to 1430°C. α' -TCP forms in the temperature range between 1430°C and the melting point, 1756°C, but it does not survive quenching to room temperature. γ -TCP is known as a high-pressure polymorph. α -TCP and β -TCP have the same chemical composition, but they are different in crystallographic structure /6,9/.

α -TCP belongs to the monoclinic space group P2₁/a (Fig.2a) with unit cell parameters a = 1.2887(2) nm, b = 2.7280(4) nm, c = 1.5219 nm, β = 126.20(1)°, with 24 formula units per unit cell. Ca²⁺ and PO₄³⁻ ions are packed along the c-axis into two kinds of column, one kind is Ca²⁺-Ca²⁺ and the other is Ca²⁺-PO₄³⁻. Especially, α -TCP possesses a crystal structure comparable to the structure of apatite. The b-axis parameter of α -TCP corresponds to the a-axis parameter of apatite, whilst half of the c-axis parameter of α -TCP corresponds to the c-axis parameter of apatite. Thus,

α -TCP can change readily to apatite by replacing the cation-cation columns at the corners of the cell by anion columns /6,10/.

β -TCP has a structure of the rhombohedral space group R3c (Fig.2b) with unit cell parameters $a = 1.0439(1)$ nm, $c = 3.7375(6)$ nm, $Z = 21$ (hexagonal setting) /10/. The β -TCP structure is similar to $Ba_3(VO_4)_2$, but the Ca^{2+} size is smaller than the Ba^{2+} size. Hence the number of oxygen atoms coordinated to the cations is reduced and has three formula units per hexagonal unit cell less. β -TCP also has two kinds of column; both types contain cations and anions. Ceramics of β -TCP are being used as bone substitute for many years.

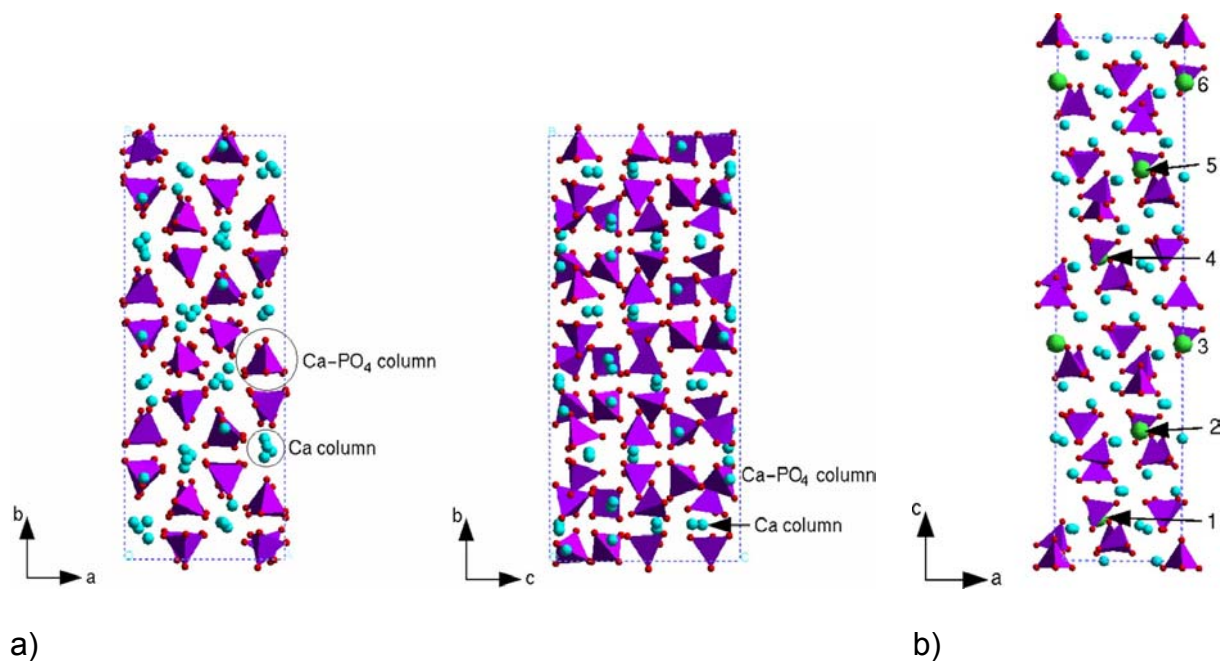


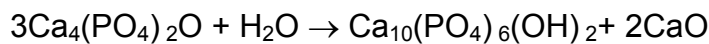
Figure 2: Unit cell of TCP: Tetrahedra represent PO_4^{3-} , blue balls are Ca atoms /24/.

- a) α -TCP: Projected onto the (a,b) plane (left); Projected onto the (b,c) plane
- b) β -TCP: Projected on the (a,c) plane. Big balls (1-6) indicate Ca atoms with half occupancy

Each formula unit occupies 18 nm^3 in α -TCP compared with 16.8 nm^3 in β -TCP form, so α -TCP is easier to change the structure and to react with water than β -TCP. α -TCP is more biocompatible and biodegradable than β -TCP. A major difference between the structure of α - and β -TCP is the lack of cation-cation columns in β -TCP, so IR spectra of α - and β -TCP differ at $\nu_4(PO_4)$. α -TCP has a single broad band at 600 cm^{-1} , but the spectrum of β -TCP splits into 2 bands at 550 and 616 cm^{-1} . There are weak, distinct bands in α -TCP at 460 and 740 cm^{-1} , but absent in β -TCP /6/.

1.3.2. Tetracalcium phosphate

Tetracalcium phosphate has the chemical formula $\text{Ca}_4(\text{PO}_4)_2\text{O}$. It is monoclinic with the space group P2_1 with $a = 0.7023(1)$ nm, $b = 1.1986(4)$ nm, $c = 0.9473(2)$ nm and $\beta = 90.90(1)^\circ$ at 25°C /10/. In TTCP, Ca^{2+} and PO_4^{3-} are located in four sheets, which are perpendicular to the b-axis. Each sheet in the a-axis direction has one cation column Ca^{2+} - Ca^{2+} and two cation-anion columns Ca^{2+} - PO_4^{3-} . TTCP melts at 1720°C . Comparing the lattice parameters of TTCP and HA, it is evident that TTCP and HA have similar lattice dimensions. TTCP is stable in water at room temperature for some time, but easily reacts with water at high temperature by transformation to HA /6/:



In several dental cement systems, tetracalcium phosphate finds a very important application /11/. In bone cement, TTCP is mixed with either dicalcium phosphate dihydrate (DCPD, brushite) or dicalcium phosphate anhydrous (DCPA, monetite), that are major ingredients which form HA in the presence of water.

1.3.3. Hydroxylapatite

1.3.3.1. Crystal structure of hydroxylapatite

Apatite represents a fairly large group of chemically different substances. Their structure is deduced from the hexagonal space group $\text{P6}_3/\text{m}$, with the general chemical formula:



whereas,

M is a one- to threevalent cation, (e.g.: Ca^{2+} , Pb^{2+} , Cd^{2+} , Sr^{2+} , Ni^{2+} , Al^{3+} , Y^{3+} , La^{3+} , Ce^{3+} , K^+ , Na^+)

Z is a three – sevenvalent ion forming anion complexes, (e.g.: P^{5+} , V^{5+} , As^{5+} , Cr^{3+} , Si^{4+} , C^{4+} , Al^{3+} , S^{6+} , Re^{7+})

and X is a zero- to threevalent anion (e.g.: OH^- , F^- , Cl^- , Br^- , I^- , O^{2-} , N^{3-} , CO_3^{2-} , or H_2O and vacancies)

The crystal structure of hydroxylapatite with $M=Ca^{+2}$, $Z=P^{+5}$ and $X=OH^-$ possesses the lattice parameters $a(=b)= 0.9432$ nm and $c= 0.68814$ nm, $z=2$ (Fig.3). The chemical formula of stoichiometric hydroxylapatite is $Ca_{10}(PO_4)_6(OH)_2$.

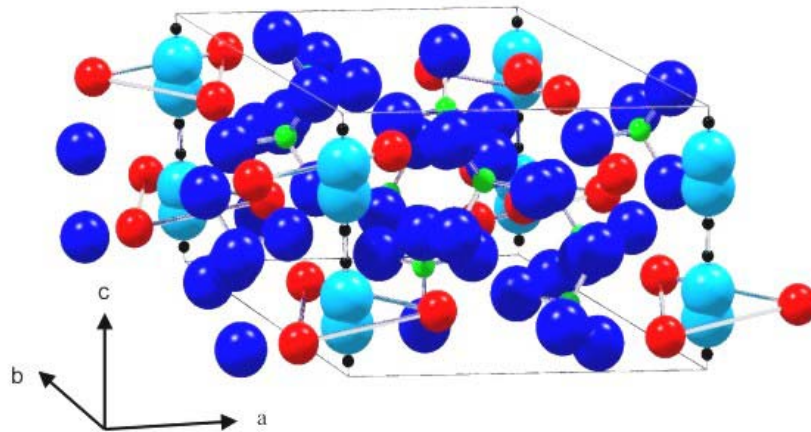


Figure 3: Structure of hydroxylapatite. Each OH position (light blue) is statistically occupied at 50 %. Six of the Ca^{2+} ions (red) are coordinated with hydroxyl ions and form triangles perpendicularly to the OH columns. The tetrahedron is represented by P (green) and O (blue).

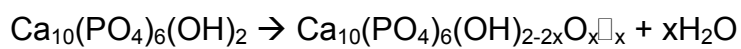
Two oxygen atoms of the PO_4^{3-} tetrahedron are located on mirror planes through $z= 1/4$ and $z= 3/4$. The other two order symmetrically above and below the mirror planes. The Ca^{2+} ions occur in two different positions: one ion row at $z= 0$ and $1/2$, and screw axis ions at $z= 1/4$ and $3/4$, respectively. Three Ca^{2+} ions of the screw axis form a triangle at the mirror plane. It results in a screw axis parallel to the c-axis. The OH^- ions are ordered along the screw axis. Because of this structure, there are direction-dependent differences in the mobility of ions. Ca^{2+} and OH^- ions are very mobile along the c-axis /13,14/. This finding is of great importance for later explanations. Since the ion OH^- can be replaced by F^- or Cl^- or by a vacancy, etc. The hexagonal hydroxylapatite is probably never strictly stoichiometric.

Stoichiometric hydroxylapatite crystallizes in the monoclinic space group $P2_1/b$ with lattice parameters $a = 0.94214$ nm, $b= 2a$, $c = 0.68814$ nm, $\gamma= 120^\circ$, $z=4$, i.e, and twice the number of formula units per unit cell as in the hexagonal unit /15/. The

monoclinic structure is closely related to that of the hexagonal form, but with no restrictions imposed by the mirror symmetry. There is no disordering of the OH⁻ ions in the monoclinic form. The monoclinic modification forms only under favourable thermal conditions /10/.

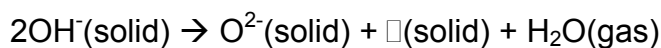
1.3.3.2. Thermal stability of hydroxylapatite

During heat treatment, hydroxylapatite starts to decompose by partial loss of OH⁻ groups to form oxyhydroxylapatite (OHA) at nearly 800°C. Complete loss of OH⁻ generates oxyapatite. The decomposition can be described by:



with $0 \leq x \leq 1$, □ represents the lattice vacancies.

The existence of oxyapatite (OA) was a subject of controversy for many years. However, its formation is now well established /16,17/. A recent study revealed that a small amount of OH⁻ is always present in the structure of oxyapatite /19/. In this study it was demonstrated by X-ray diffraction (XRD) that HA can lose a substantial amount of water by strong heating, whilst the integrity of the lattice was maintained. A loss of up to 75 % of the chemically bound water does not change the channel structure of apatite. Oxyapatite should really be considered as oxyhydroxylapatite. According to Hartmann et al. /18/, oxyhydroxylapatite prepared by thermal heating represents a special type of non-stoichiometric hydroxylapatite (ns-HA) with a partially distorted structure. The water content of $\text{Ca}_{10}(\text{PO}_4)_6(\text{OH})_{2-2x}\text{O}_x\text{□}_x$ at equilibrium with water vapour of partial pressure p (mmHg) has been discussed as a function of temperature. The following reaction is considered:

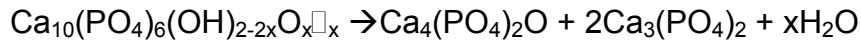


The equilibrium constant of the above reaction, $k(T)$, was found /20/ to be:

$$k(T) = 1.2 \cdot 10^9 \cdot e^{-\Delta H / R \cdot T},$$

where R is the gas constant, and ΔH is the experimentally determined enthalpy change.

At higher temperatures and low water pressure, destruction of the apatite structure occurs, and TTCP and α -TCP are formed according to the reaction:



The temperature at which equilibrium for the above reaction exists depends on the partial pressure of water vapour. Higher pressure of water vapour shifts the decomposition to higher temperatures, e.g.: 1598 \pm 10 K at 0.613 kPa, 1750 \pm 10 K at 9.81 kPa, and 1838 \pm 10 K at 101.3 kPa. Finally, TCP melts at 1756°C, whereas TTCP melts incongruently at 1720°C leaving CaO as a residual solid /6/.

1.3.3.3. Non-stoichiometry of hydroxylapatite

Because of its crystal structure, hydroxylapatite is able to incorporate other ions by substituting Ca^{2+} cations and OH^- and PO_4^{3-} anions without distortion of the lattice. A surprising example for that is the biological apatite /21/. Here calcium is substituted partially by Sr, Na, K, Mg, and some trace elements (Pb, Ba, Zn and Fe). CO_3^{2-} substitutes some PO_4^{3-} tetrahedra. Some OH^- can be exchanged by Cl^- , F^- , or CO_3^{2-} . This exchange ability of hydroxylapatite causes its high bioconductivity in medical application /22/.

Stoichiometric hydroxylapatite possesses a molar Ca/P ratio of 1.67 and water content of 1.79 %. Hydroxylapatite, which forms in an aqueous solution, exhibits often a non-stoichiometric composition. There is a large number of different synthetic routes and approaches demonstrating the difficulty of making stoichiometric hydroxylapatite /23/. The non-stoichiometry can be described by the chemical formula /24,25,26/:



But, the anion (OH^- , Cl^- , F^-) positions in apatite can also be substituted by O^{2-} or by a vacancy or by a combination of the mentioned ions. In the stoichiometric form each anion takes up its own particular location. However, when two or more of these ions are present at the same time, they interact with each other to produce effects not predicted from the knowledge of the structures and the end-member alone /27,28,29/.

In the present thesis implants with a bioconductive coating, especially with HA for load-bearing bone replacements will be discussed in more detail.

1.4 Hydroxylapatite coatings

Metals are being used in load-bearing orthopaedic applications. Cobalt-based alloys and titanium-based alloys are widely used, particular Ti-6Al-4V, because of its superior high strength, low specific weight, biocompatibility and excellent corrosion resistance. However, many problems posed by metallic materials in the human body are related to corrosion, wear and negative interaction with the tissue /30/. The metal ions from corrosion products, such as Co, Cr, Ni, Al and V can have seriously toxic consequences. Those ions may cause inflammation, tissue damage and fibrosis of tissue surrounding the implants and may eventually result in implant failure /31/. Many methods have been applied to modify the surface of titanium alloy and make it suitable for biological purposes (passivation, anodization, ion implantation, and coating). The main method used is coating with calcium phosphate materials, mostly with hydroxylapatite. There are different methods to coat HA, e.g. ion beam dynamic mixing, radiofrequency, liquid immersion techniques, plasma spraying, sintering, gluing, etc. Heimann et al. gave a thorough overview over those coating methods in /32/. Among those coating methods, plasma spraying is very popular. Plasma spraying of calcium phosphate coatings was described in /33/. A short introduction to this coating technology will be given below.

1.4.1 Plasma spraying technique

Plasma spraying is a relatively old coating technology. The plasmatron is pictured schematically in Fig.4, comprising a copper anode and tungsten cathode, both of which are water-cooled.

Most plasmatrons operate at powers between 20-80 kW, some special devices can operate at powers as high as 250 kW. A pressurized gas is passed between the electrodes where it is heated to very high temperature, dissociated and ionized to form a plasma jet, consisting of electrons, ions, neutral particles and photons. The temperature of the plasma just outside of the nozzle can be as high as 15000 K depending on the type of gas used and the power input. The plasma temperature

drops off rapidly when exiting the anode. The gas frequently used is argon, but hydrogen, nitrogen and helium are also used as auxiliary gases /35/. The energy content of these gases is shown as a function of the temperature in Fig.5.

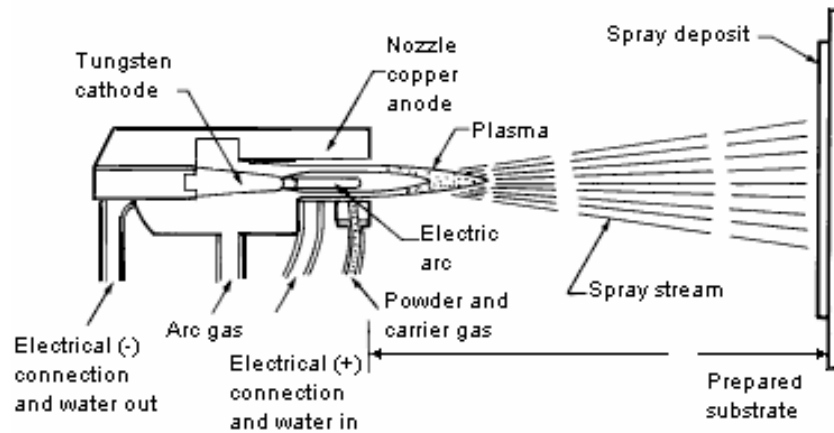


Figure 4: Schematic of plasmatron /34/

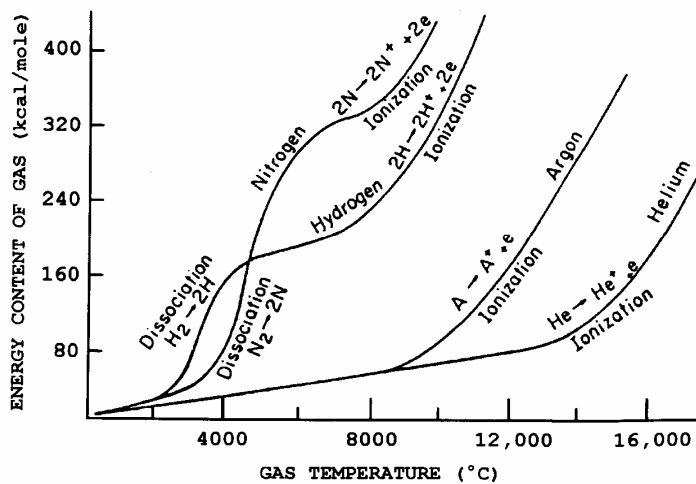


Figure 5: Energy content of some plasma gases as a function of temperature /36/

The properties of the plasma and hence the deposited coatings are influenced by many parameters. These factors are extrinsic, for example the spray distance and intrinsic, such as the plasma characteristics. The latter one is a complex factor of the type of gases, the ionization degree, the plasma velocity and the plasma length. The residence time of particles within the jet is very important. It depends on the velocity of the spray particles, which is dependent on the gas velocity, and on the flight path of the particle in the jet. Figure 6 shows the temperature and the axial velocity of a typical plasma arc /37/. The maximum temperature is found to be in the core of the jet close to the nozzle exit and along the centre line.

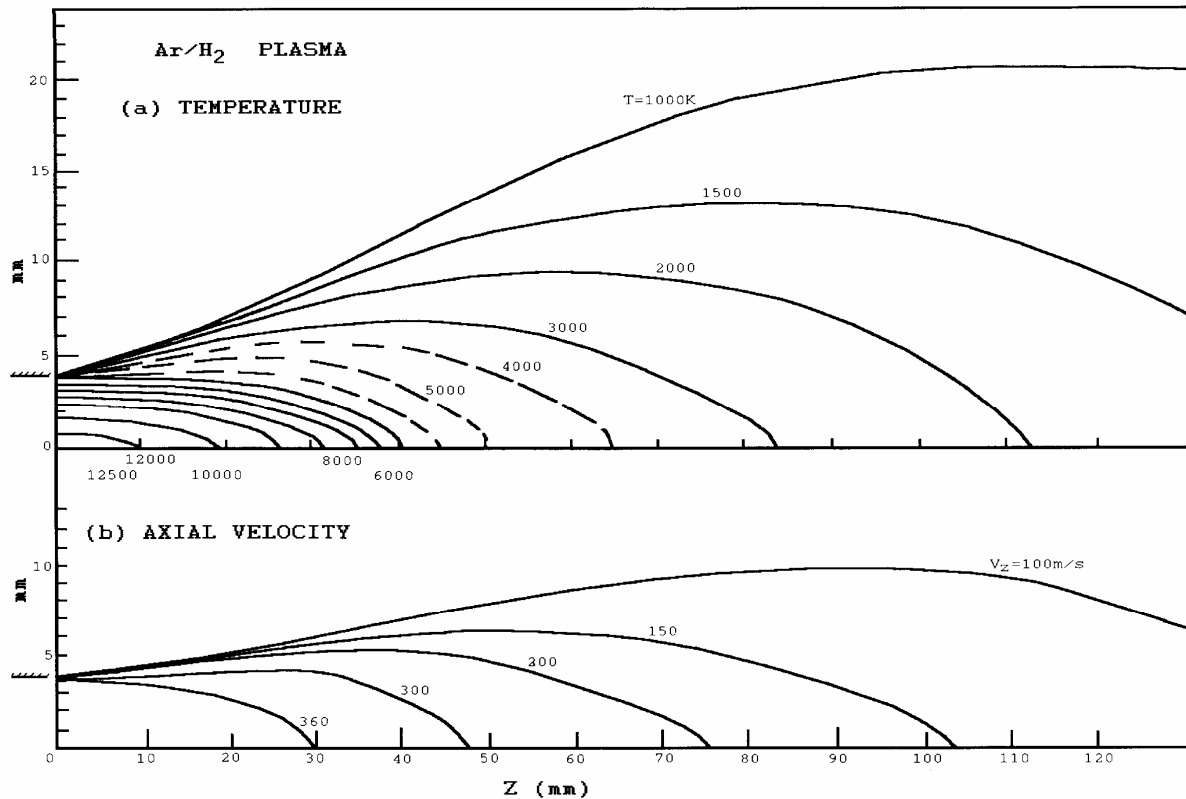


Figure 6: Temperature and axial velocity distribution of a d.c. argon/hydrogen plasma arc along the direction of propagation /37/

The plasma spraying process is based on the spraying of molten or thermally softened materials onto a surface of a substrate to provide a coating. A granulated coating material is fed into the plasma jet most commonly via an external powder port near the anode nozzle exit. The powder is rapidly heated, melts and is propelled towards the substrate with high velocity. The molten droplets then solidify and flatten quickly. This process is repeated many millions of time and a layer-by-layer build up takes place through interparticle bonding/anchoring and sintering reactions. The bonding strength, density and microstructure of the coating are influenced by the velocity and contact temperature of the molten particles upon the substrate material, by the particle distribution of the starting material, as well as by the process parameters /35/.

Plasma spraying can be applied in air or in a special atmosphere (vacuum chamber, controlled atmosphere, etc.). In special atmosphere some of the properties of coatings are improved.

1.4.2 Plasma-sprayed hydroxylapatite coatings

Since hydroxylapatite is the main mineral of teeth and bone, it does not cause any toxic effects when incorporated into the body. Hence, hydroxylapatite provides excellent biocompatibility. In several studies it is indicated that HA coatings can hasten the initial biological response to the implant devices and can form a good biological base for bone ingrowth and interfacial stability. Bone was found to grow directly into a HA layer, without an intervening layer /38,39,40,41/. Also, an HA coating can decrease the release of metal ions from the implant to the body /42/ and protects metal surface from attack by corrosive body fluid.

Although plasma spraying represents state-of-the-art in implantology, one essential drawback of plasma spraying of HA should be mentioned: the extreme hot plasma jet causes partial decomposition of HA. The following effects have been observed:

- The XRD pattern of HA coating is different to that of the starting material. The intensity of the HA peaks reduces, the line shape broadens, and some impurity phases like TCP, TTCP, CaO appear additionally /43,44,45/.
- Observing the plasma-sprayed HA coating by infrared spectroscopy (IR), Park et al. /46/ found that the spectrum has new shoulders at 990, 942 and 550 cm^{-1} , and it loses a band at 960 cm^{-1} . The latter indicates that the structural environment around the phosphate ion changes after plasma spraying. The new band at 942 cm^{-1} can be attributed to the asymmetric stretching mode of the P-O bond of β -TCP.
- With IR the dehydroxylation of HA was noted by the decreased intensity of the OH stretching vibration band at 3571 cm^{-1} and loss of the OH librational band at 630 cm^{-1} . The IR analysis did not show HA, so the peak of HA in XRD can be ascribed to extremely dehydroxylated oxyapatite, because the structural water can be lost while still retaining the HA structure /46,47/. The HA and OHA or OA have only small differences in lattice parameters, which produces peak overlapping in the X-ray pattern. Hence, the XRD is not suitable to distinguish between HA and OHA.
- A much more powerful analytical method for this distinction is ^1H and ^{31}P – Magic Angle Spinning - Nuclear Magnetic Resonance spectroscopy. The ^1H spectra provide information on the position and environment of the hydroxyl

groups, ^{31}P spectra provide information on the positions of the PO_4^{3-} . It was found that the spectra of HA coatings have additional peaks compared with the original HA powder spectra. Plasma spraying causes significant change of the HA structure /48,49/.

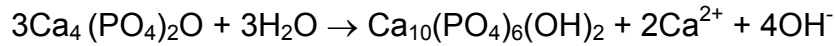
When the molten HA droplets impact onto the substrate surface, their temperature reduces to around 1000°C , because usually the substrate has a low temperature and a high thermal conductivity. Rapid cooling freezes the molten particles under non-equilibrium conditions and a part of the bioceramic coating re-crystallizes so fast, that it becomes more or less amorphous. This amorphous phase is characterized by a band at 952 cm^{-1} in the Raman spectra /50/, appearing as weak shoulder at the low frequency side of the PO_4^{3-} band at 962 cm^{-1} . By transmission electron microscopy (TEM), the amorphous phase was also found mostly at the interface of the coating and substrate. Results of energy dispersive X-ray analyses indicated that the amorphous phase is composed of calcium, phosphorus and oxygen, with a Ca/P ratio of about 0.8 /43,51/. The components in plasma sprayed coatings include HA, OHA, TTCP, TCP, CaO and amorphous phases. The composition and the quality of coating depend strongly on the spray parameters, the purity and the particle size of the hydroxylapatite powder /33,52,53,54/.

1.4.3 *In-vitro* and *in-vivo* behaviour of hydroxylapatite coatings

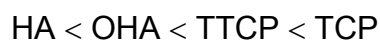
Plasma-sprayed HA coating has a composition and crystallinity differing from stoichiometric HA, that in turn affects its bioconductivity and long-term stability when it is implanted into the body.

In-vitro and *in-vivo* experiments are a very important part of implant materials research. Such tests will supply fundamental knowledge on the interaction between the implant and the living tissue. Furthermore, they help to optimize the implant properties and thereafter to increase the osteoconductivity and osteointegration of the implant. Therefore, *in-vitro* experiments have been carried out to investigate the effects of structural changes. *In-vitro* tests with salt solutions, which simulate the body conditions, are used to observe the behaviour of implants after certain incubation time. These experiments can help to understand the behaviour of the implant, before expensive and protracted *in-vivo* tests will be conducted.

The structure of incubated HA coatings was evaluated by X-ray diffractometry. It was found that the TTCP phase disappeared and the amount of TCP was reduced /55, 57, 62/. TCP and TTCP can transform in aqueous solutions as follows /6/:



Also by XRD, the intensity of the HA peak was found to increase, whereas the amorphous phase slightly decreases. This suggests an increase in crystallinity /56,57,58/. TTCP, TCP and the amorphous phases dissolve in solution to create such a level of the calcium and phosphorus ion concentration, that a re-precipitation or ion exchange reaction will occur and a completely new layer forms on the HA coating surface. XRD and IR analyses indicated that this new layer is akin to bone-like apatite. In the new layer, CO_3^{2-} was obviously incorporated into the apatite lattice, and the thickness of the new layer increased with immersion time /58,59/. The bone-like apatite layer pre-formed on the HA coating will assist the bone attachment by promoting faster bone bonding with living tissue and hence increases the longevity of the coating on implanting *in-vivo* /60/. However, the dissolution would also leave a porous structure in the coating, that weakens the interlamellar layers, and subsequently decreases the mechanical strength of the coating /61,62/. The dissolution behaviour of the plasma-sprayed coating depends on their phase composition. The solubility of calcium phosphates decreases in the order /63/:



The physico-chemical and biological processes determining the transformation of a bioconductive ceramic surface into bone can be divided in four steps /137/:

- First, the calcium phosphate layer is partially dissolved which enhances the concentration of Ca^{2+} and PO_4^{3-} ions at the interface between the coating and tissue /138,122/.
- In the next step, new HA micro-crystals form due to biomimetic mechanisms /57,92/. This HA consumes biological ions from the surrounding fluid such as Ca^{2+} and PO_4^{3-} . It also incorporates other ions such as CO_3^{2-} , Mg^{2+} and Na^+ into its lattice.

- Adsorption of non-collagenous proteins onto the HA micro crystals. Such proteins are e.g. proteoglycane, which are coupled through chondroitin sulfate bonds (Fig.7) to the OH⁻ ions of the HA structure, glycoproteins (sialoproteins), osteonectin and osteocalcin /39,12/. The non-collagenous proteins form only a small part of the organic bone matrix (appr. 5 %), but they play an essential role in the mineralization process.
- Adoption of the microcrystals into the collagen matrix of newly formed bone.

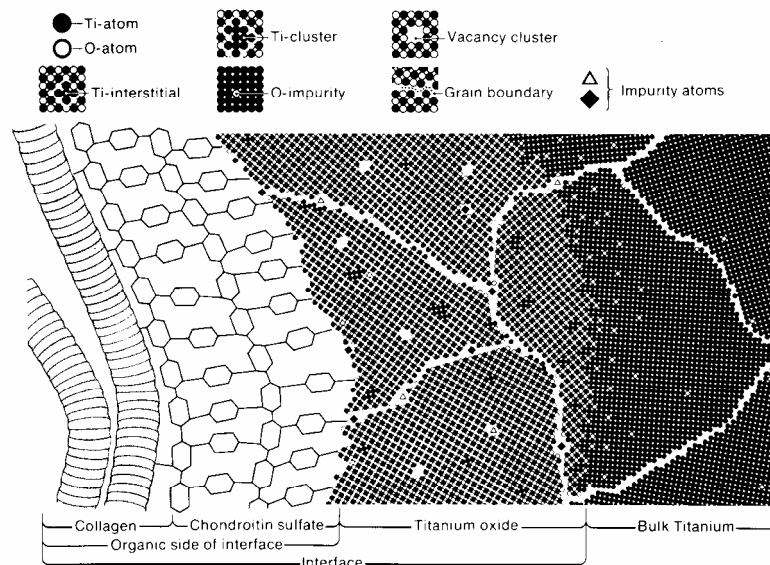


Figure 7: Model of bonding of bone cells onto a Ti-implant. Collagen fibrilles attach to the protein layer (chondroitin sulfate) which is adsorbed at the oxide layer formed at the implant surface /95/.

The bonding ability of proteins to calcium phosphates has been estimated by the presence of charged groups on the proteins and on the apatitic surfaces /64/. It has been suggested that proteins compete with Ca²⁺ and PO₄³⁻ ions for the same surface binding sites /65,66,67/. Thus proteins can cover the surface sites and block the growth sites of nucleated calcium phosphate /67,68/. It is possible that proteins still continue to bind Ca²⁺ ions after adsorption, since more than one functional group may be available in proteins to bind to Ca²⁺ ions. This means that even though proteins block the natural binding sites on the calcium phosphate surface, the adsorbed proteins may still provide additional binding sites. Thus, the proteins can function as sites for calcium phosphate nucleation from solution /65,66,67,69/. They can be considered defects of the previous calcium phosphate surfaces and help

actively in nucleation and growth of new crystals. Hence, this model can explain the high integration and fast bone ingrowth into implant with a hydroxylapatite coating. The intimate association of the inorganic mineral (incl. calcium phosphate) and organic macromolecules, including proteins is an essential feature of bone. Many studies have confirmed essential advantages of calcium phosphate coatings on implant. Such coatings demonstrate osteoconducting properties with bone formation in direct contact with the coating /70/.

During application of the implant, coating thickness was observed to be reduced, but a faster fixation of the implant into bone is induced /71/, and no intermediate soft tissue layer is seen between the bone and the implant surface /41,72/. Histological investigations showed that CP coated implants appear to induce more bone formation than non-coated implants /73/. Geesink et al. /74/ found that plasma-sprayed hydroxylapatite coatings can form a chemical bond with high strength comparable to cortical bone itself. At the begin of the healing process the hydroxylapatite coating is better for creating earlier and strong fixation with bone /72,75/. The *in-vivo* behaviour of implants is among others influenced by the crystallinity of the hydroxypatite coating. Coatings with high crystallinity show a higher shear strength and remained integrated for long term stability, while coatings with low crystallinity are easily separated from the metallic implant, but the low crystallinity can helpfully support the initial fixation of bone /76/. A further important feature of bioconductive ceramic coatings is that the bone has a higher affinity to the bioconductive ceramic materials than to titanium and polymers. Not only direct accumulation of bone at the implant surface is known, but also the newly formed bone penetrates deeply into implant cavities /77/. Consequently, bone contacts much more to the HA surface than to the surface of titanium substrate as well as to a porous plasma-sprayed titanium layer /78,79/.

A recent study by Lintner et al. /80/ confirmed the increased formation of new bone on the surface of implants with an HA coating in comparison to the implant without an HA coating, where the thickness of the coating decreases continuously by resorption. Even, when the HA coating has been completely degraded, the new bone contacts directly to the surface of the titanium alloys. This process leads to further (secondary) stabilization of the implant.

1.4.4 Bond coat for hydroxylapatite coatings

The *in-vivo* stability of implants with a bioconductive coating is of great importance. It depends on porosity, sufficient resorption resistance, chemical purity, phase composition, crystallinity, fracture toughness, and adhesive strength of HA coatings. To optimize these characteristics, many methods have been proposed, such as heat treatment of the coating before implanting /81,82, 83/, optimization of plasma spray parameters /54,62,84/, or utilization of a bioinert bond coat between HA and metal substrate /85,86/.

Applying a bioinert bond coat (BC) between HA and metal substrate has been chosen to improve the quality of the HA coating, for the following reasons /87/:

- The bond coat binds well to both the metal and the HA coating. Hence, the risk of the formation of a gap between metal and coating that promotes invasion of acellular connecting tissue and hence implant loosening will be considerably reduced.
- The hydroxylapatite coating itself can absorb ion metals released from Ti6Al4V and stainless steel implants /42,88,89/. However the plasma-sprayed HA coating is not stable *in-vitro* and *in-vivo* because the coating contains TCP and TTCP and amorphous phases. Those phases dissolve easily in solution. The coating thickness will be reduced and the metal ions can still be released to the surrounding living tissue. The bond coat will reduce or prevent completely the release of metal ions diffusing from the substrate to the living tissue, which cause hypersensitivity, toxicity and carcinogenic reactions /31/.
- The BC prevents the direct contact between the metallic substrate and HA since this could catalyse the thermal decomposition of HA towards tri- or tetracalcium phosphate or even undesirable CaO,
- The BC reduces the heat transfer rate of the substrate, so that the molten splats have enough time to crystallize and hence to improve *in-vivo* performance, e.g. longevity of implants. The heat transfer rate is not only related to the thermal conductivity, but is also dependent on the porosity of the bond coat. The surface roughness affects the heat transfer also.

- The BC alleviates the gradient of the coefficients of thermal expansion between the substrate and the coating hence minimizing crack generation, chipping and/or delaminating, as well as,
- The BC decreases the damage initiated by cyclic micro-motions of the implant during movement of the patient in the initial healing process.

Since the failure of HA coating/Ti alloy - bone specimens under tensile testing usually occurs at the interface HA coating/Ti alloy, it indicates clearly that the interface bonding between the HA coating and the Ti alloy is not strong enough. Filiaggi et al. /83/ found that the surface roughness of the Ti alloy correlates with bonding strength and fracture toughness. When TiO₂ and ZrO₂ were applied as a bond coat, the adhesion strength of the bond coat systems determined by peel tests increased by 50 to 100% when compared with the HA coating without a bond coat /90/. Other studies /86/ also observed a higher adhesion strength of the coating in case of a ZrO₂ bond coat (36.2±3.02 MPa with the ZrO₂ bond coat in comparison with 28.6±3.22 MPa without a bond coat). The roughness of the bond coat measured by the authors in /86/ is higher than that of the substrate after grit blasting. As a consequence, mechanical interlocking between the HA coating and the bond coat is better than between the HA coating and the metal substrate. Hence the adhesion strength of the bond-coat systems increases.

In a recent study /142/, it is thought that the bond coat acts as a thermal barrier suppressing the fast quenching of superheated spray particles at the cool substrate surface that results in 'amorphous' calcium phosphate (ACP?) and various distorted and crystallographically ill-defined intermediate thermal decomposition products. The hydroxyapatite remaining after 4 weeks incubation in R(revised)-SBF is highly crystalline and ordered thus possessing a high degree of resorption resistance towards the aggressive action of body fluid *in vivo*. Consequently, the application of such bond coats to Ti alloy implants will improve significantly both the adhesive strength of the 'duplex' coating to the implant material and the chemical stability of the coating. This improvement prevents formation of gaps between implant and coating that give rise to aseptically loosening of the implant.

1.5 Brief summary of literature study

Although hydroxylapatite has been plasma-sprayed on Ti6Al4V alloys for implants for quite a while, some knowledge is still missing in the literature. The following essential questions should be answered by the present thesis:

- Plasma spraying considerably changes the structure of hydroxylapatite. Such micro structural changes and the dehydroxylation/ decomposition products will be characterized more extensively.
- How does the incubation process affect the reconstruction of distorted hydroxylapatite *in-vitro* and *in vivo*? Because of limitation of time and resources, only *in-vitro* experiment will be conducted in this thesis.
- An explanation of the mechanisms of transformation of distorted (oxy)hydroxylapatite to well-ordered hydroxylapatite should be given in this work.
- The advantage of applying a bond coat to the implant system has been discussed so far only from a mechanical point of view. Beside of the above questions, the influence of a TiO₂ bond coat on the structure and behaviour of the bioconductive coating will be highlighted.
- Finally, the possibility of achieving hydroxylapatite coatings with a high chemical stability will be shown.

2 Materials and investigation methods

2.1 Materials

2.1.1 Hydroxylapatite for bioconductive coatings

Hydroxylapatite powders with the following properties were used for plasma spraying (Fig.8):

Powder 1:

- Mn-doped hydroxylapatite (DePuy Bioland, Toulouse, France)
- Particle size: +80-160 μm (information by supplier).
- Mn content: 188 ppm.

- Mineral phases analysed by XRD: 91.7 ± 0.6 % hydroxylapatite , 8.3 ± 0.6 % β -tricalcium phosphate

Powder 2:

- Hydroxylapatite (Plasma Biotal Limited, North Derbyshire, United Kingdom)
- Particle size: +100-140 μm (information by supplier)
- Mineral phases analysed by XRD: 100% hydroxylapatite

The Mn-doped hydroxylapatite powder (Powder 1) was used to provide a basis to compare the results previously reported in cathodoluminescence studies by Hildebrandt /91/ and Götze et al. /92/. After exhaustion of this powder, the powder 2 was used for further experiments.

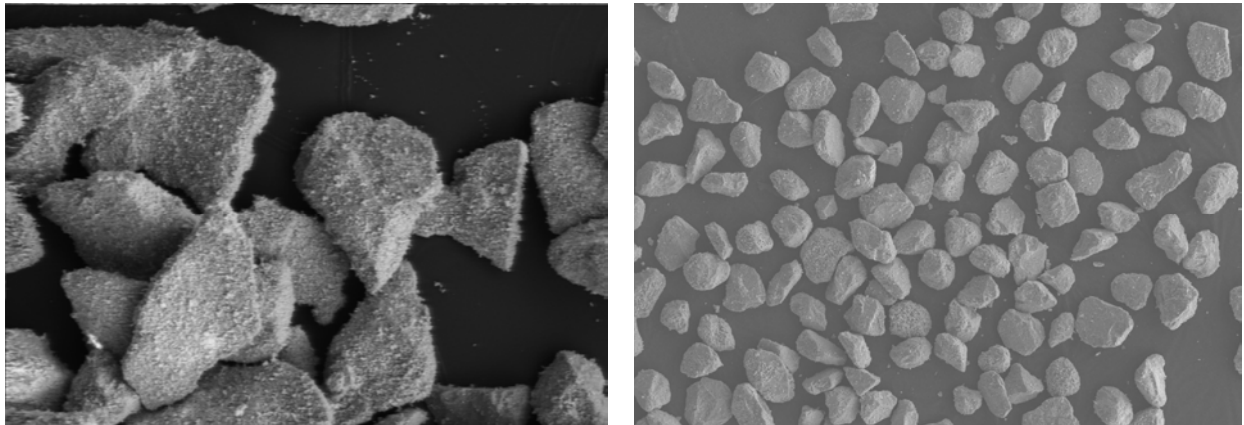


Figure 8: HA powders used for coatings in the present thesis: a) powder 1 and b) powder 2. Note: The pictures have different scale of magnification.

2.1.2 Titanium dioxide as a bond coat

A titania powder (trade name AMDRYTM 6500; Sulzer Metco GmbH) with a grain size of 5-22 μm was applied to produce the bond coat. This powder was also used in other studies /91,85/.

2.1.3 Titanium alloy Ti-6Al-4V as a substrate

A commercially available Ti6Al4V alloy sheet was used as substrate for coatings. From this sheet coupons of dimensions 50 x 20 x 2 mm were cut.

2.2 Preparation of coatings

2.2.1 Atmospheric plasma spraying

Before coating, the surface of the coupons was blasted by corundum grit (grain size 0.5-1.0 mm) with 4.0 bar compressed air, cleaned with deionized water in an ultrasonic bath, then dried in air.

Sprayed coupons were prepared with or without a bond coat of TiO₂.

All coating experiments were performed by atmospheric plasma spraying (APS) using a PT M-1000 system equipped with a Sulzer Metco PT MB plasmatron at the Department of Mineralogy, TU Bergakademie Freiberg. The applied parameters were optimized in earlier studies by the research group of Prof. Heimann /57,91/ and are listed in Tab.3:

Table 3: Plasma spray parameters used in this work

Parameters	Units	TiO ₂ bond coat	HA coating
Plasma power	kW	39	32
Hydrogen flow rate	l/min	12	6.5
Argon flow rate	l/min	40	45
Powder carrier gas (Ar)	l/min	3	5
Disk rotation	%	8	20
Stirrer rotation	%	40	40
Translation speed	m/min	20	6
Spray distance	mm	100	90

Two sets of coatings were prepared:

Set 1:

- A bioconductive coating was sprayed with HA powder 1 (Mn-doped)
- The thickness of the TiO₂ bond coat was adjusted to 15 µm.

Set 2:

- A bioconductive coating was sprayed with HA powder 2
- The thickness of the TiO₂ layer varied between 0, 15, 30, 40 and 50 µm.

Actually the bond coat consists of substoichiometric Ti_nO_{2n-1} (Magnéli) phases. However, for sake of convenience the term “ TiO_2 bond coat” will be retained throughout this thesis.

In both sets 1 and 2, the plasma-sprayed hydroxylapatite coating was about 150 μm thick.

2.2.2 Incubation of coatings

A revised protein-free simulated body fluid (r-SBF) was used in the *in-vitro* experiment. This solution was prepared in conformance with recommendation in /93/, because it should enable a high activity in nucleating precipitated HA crystals on the coatings immersed. Furthermore, a high content of HCO_3^- ions in this r-SBF could favour formation of carbonated bone-like apatite /94/. Table 4 shows the composition of the r-SBF. Before incubating, the samples were carefully washed with methanol and deionized water to remove dusty and fatty contamination. Coatings were immersed in the r-SBF, in covered boxes for 1, 2, 4, 8, 12 or 24 weeks at $37 \pm 0.5^\circ C$. The quantity of solution was calculated to be 0,3 ml per 1 mm^2 coating surface. After different immersion times, the samples were removed from the solution, washed with deionized water, and dried in dust free air at $105^\circ C$ for 24 h.

Table 4: Ion concentration of the revised simulated body fluid in comparison with blood plasma /93/

Ions	Blood plasma (mmol/l)	r-SBF (mmol/l)
Na^+	142.0	142.0
K^+	5.0	5.0
Mg^{2+}	1.5	1.5
Ca^{2+}	2.5	2.5
Cl^-	103	103
HCO_3^-	27	27
HPO_4^{2-}	1.0	1.0
SO_4^{2-}	0.5	0.5

The buffer agents HEPES (2-(4-(2-hydroxyethyl)-1-piperazinyl) ethane sulfonic acid [C₈H₁₈N₂O₄S]) (11.928 g/l) and NaOH 1M (15 ml /l) (both substances were analytical grade from Merck Eurolab GmbH, Dresden) served to stabilize the solution for the entire immersion period.

2.2.3 Thermal post-treatment of coatings

Two powder samples were scratched of the plasma-sprayed HA coatings without and with a bond coat. These powders were then subjected to thermal post-treatment at 630°C for 24 h in air. Since under these conditions no decomposition of HA and other calcium phosphates would occur /95,96/, the transformation of amorphous phases into crystalline phases was expected. During this treatment, TCP may react with TTCP and water vapour to form HA. The goal of the experiment is to characterize the influence of post-firing on the structural changes.

2.3 Description of analytical methods

In this chapter, the analytical methods used in this study will be briefly introduced.

2.3.1 Nuclear magnetic resonance spectroscopy

Nuclear Magnetic Resonance spectroscopy: NMR. The nucleus of all elements carries a charge and rotates about an axis. It possesses a nuclear or intrinsic angular momentum P , quantified by /97/:

$$P = \sqrt{I(I + 1)} \frac{h}{2\pi}$$

where h is Planck's constant and I is the angular momentum number, called the nuclear spin. The spin has usually values from 0 to 6 ($I = 0, \frac{1}{2}, 1, \frac{3}{2}, \dots, 6$), but the highest spin values can be $I=7$ (¹⁶⁶Ho and ¹⁷⁶Lu), $I=9$ (¹⁸⁰Ta).

P is associated with μ , the magnetic moment, and both P and μ are vector quantities.

$$\mu = \gamma P = \gamma \sqrt{I(I + 1)} \frac{h}{2\pi}$$

where γ is a proportionality factor and is constant for each nuclide.

When the nucleus is placed in a strong external magnetic field B_0 , some nuclei act as magnets, aligning either parallel or antiparallel to the external magnetic field. The magnetic moment will orientate to the z-axis along the direction of the external field at a certain rate or frequency (Fig.9).

$$P_z = m \frac{h}{2\pi}$$

where m is the magnetic or directional quantum number, that takes values $m = I, I-1, \dots, -I$. Hence m can have $2I + 1$ values and equals the number of possible orientations of the angular momentum and the magnetic moment in the external magnetic field.

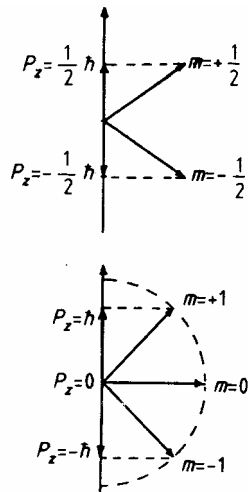


Figure 9: Directional quantization of the angular momentum P in the magnetic field for nuclei with $I=1/2$ and 1 /97/

The energy of a magnetic dipole in an external magnetic field B_0 is

$$E = -\mu_z B_0 = -m\gamma \frac{h}{2\pi} B_0$$

Because the nucleus has $(2I + 1)$ possible orientations, the nucleus has also $(2I + 1)$ energy states. The energy difference between two adjacent levels is:

$$\Delta E = \gamma \frac{h}{2\pi} B_0$$

When the nuclei are irradiated with a superimposed field B_1 of the correct quantum energy, the nuclei will reside between two energy levels. The transitions occurs only when ν_1 is chosen so that (Fig.10):

$$h\nu_1 = \Delta E$$

ν_1 : frequency of electromagnetic wave

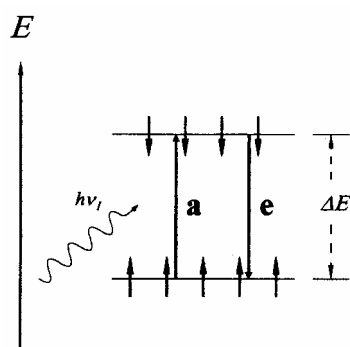


Figure 10: Energy scheme for a system of nuclei with spin $I=1/2$. Irradiation with the frequency ν_1 such that $h\nu_1 = \Delta E$ induces absorption (a) and emission (e) transitions /97/.

When the transition occurs the nuclei are said to be in resonance, hence the name Nuclear Magnetic Resonance. From NMR spectra, three parameters are obtained: chemical shifts, indirect spin-spin coupling, and intensities.

Since solid-state NMR spectra are very broad and weak, the broadness of solid-state NMR spectra makes it more difficult to interpret signals, which give information on the molecular structure. Magic-angle spinning in solid-state NMR is one method (MAS-NMR), invented by Andrew /98/, to deal successfully with the signals of solid state. MAS-NMR can eliminate the broadening due to the anisotropy of the chemical shift. In MAS-NMR the sample is rapidly rotated about an axis at an angle of $\beta_M = 54.74^\circ$ relative to the direction of the external magnetic field B_0 (Fig.11). This angle solves the equation:

$$3\cos^2\theta - 1 = 0,$$

and is known in NMR as the magic angle. In the experiment, the sample is packed into a small ceramic cylinder (rotor), which is spun rapidly around the magic angle axis in a stream of air about a few thousand revolutions per second.

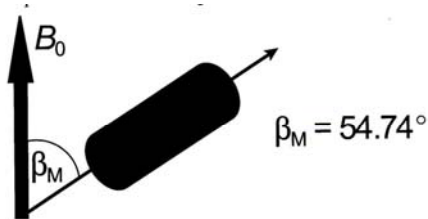


Figure 11: Magic-angle spinning introduces artificial motion by placing the axis of the sample rotor at the magic angle (54.74°) /98/.

Cross-polarization (CP) is one of the most important techniques, which is used in solid state NMR. In this method, the polarization from abundant spins such as ^1H and ^{15}F is transferred to dilute spins such as ^{13}C , ^{15}N and ^{31}P . The CP will indicate which nuclei are dipolar coupled to one another /139/

Two-dimensional NMR spectroscopy (2D-NMR) is an important tool for chemical analysis. All 2D-NMR methods are based on the coupling between nuclear dipoles. One of the 2D techniques is HETCOR (Heteronuclear Correlation). In the HETCOR spectrum, the 1D NMR of one kind of nucleus is plotted on one axis, and the 1D-NMR of another nucleus is presented on the other axis. If a signal of one axis interacts with a signal of the other axis, then a cross peak is observed at the intersection of the two axes. The cross peak in the HETCOR spectrum indicates interaction of the two kinds of nuclei /99/.

NMR is very powerful and widely used in natural sciences, from solid state to liquid, all branches of chemistry, biochemistry, biology and medicine. NMR is used for determining the composite content and molecular structure of a sample.

In the present work, the NMR experiments in chapter 3.1-3.9 were conducted with a BRUCKER AMX 400 and a TECMAG (300 MHz) spectrometer, at the Department of Optic and Quantum Electronics, University of Jena. The one-dimensional ^1H and ^{31}P spectra were obtained using Magic Angle Spinning (MAS) with rotation rates up to $f(\text{max})= 12.5$ kHz, typical $\pi/2$ pulse length of $t_w = 2$ μs , and repetition rates of 200 s. The chemical shifts were referred to a solution of phosphoric acid (85%) for ^{31}P and tetramethylsilane for ^1H NMR, respectively. The ^1H - ^{31}P 2D HETCOR spectra were acquired using cross polarization (CP) with variable contact magnitude of the ^{31}P contact pulse (contact time $t_{\text{cp}} = 5$ ms).

2.3.2 Laser Raman microspectroscopy

Laser Raman MicroSpectroscopy: LRS. Raman spectroscopy bases on the principle of the Raman scattering effect, discovered by the Indian physicist V.C.Raman, that a small fraction of the radiation scattered by certain molecules is different to that of the incident beam, when electromagnetic radiation passes through materials. The Raman scattering principle is shown in Fig.12a.

Raman spectra (Fig.12b) are obtained by inelastic scattering of light at molecules /100/. A monochromatic laser source in the visible or near infrared range is used to produce the necessary excitation of molecules. Approximately 10^{-8} parts of the incident radiation are elastically scattered and form the so-called Rayleigh line with the same frequency as the exciting radiation (ν_0). About 10^{-10} parts are consumed to excite vibrational and rotational levels of the electronic ground state (N_c) of the molecules. This brings about an energy loss of the incident radiation and induces a band shift to longer wavelength (ν_r^-) than the Rayleigh line (Stokes shift). Anti-Stokes lines have higher frequencies (ν_r^+) than the incident radiation and occur when the molecules were in an excited level (N_s , e.g., at higher temperatures) before interaction with the laser source. At room temperature these anti-Stokes lines are very weak. Hence, only the Stokes part of the spectrum is generally used. Furthermore, the abscissa of the spectrum is often labelled as simple frequency in cm^{-1} rather than as wavelength shift (Raman shift). Raman-scattered light can be shifted by as much as 4000 cm^{-1} from the incident light /101/.

Raman scattering is a versatile characterization technique for molecular analysis of bulk samples, surface or near surface species identified by their characteristic vibration frequencies. Raman spectroscopy can work with solid, liquid or gas samples, if they can be inserted into the spectrometer. Raman spectroscopy needs only a small amount of sample and very little sample preparation in comparison with another analysis methods.

All LR spectra of plasma-sprayed coatings were recorded with a Raman microprobe model T64000, Jobin Yvon at the Department of Theoretical Physics at the TU Bergakademie Freiberg. A monochromatic Ar^+ - laser with a beam diameter of ca. $3 \mu\text{m}$, energy of 5 mW and with a wavelength of 514.5 nm were used.

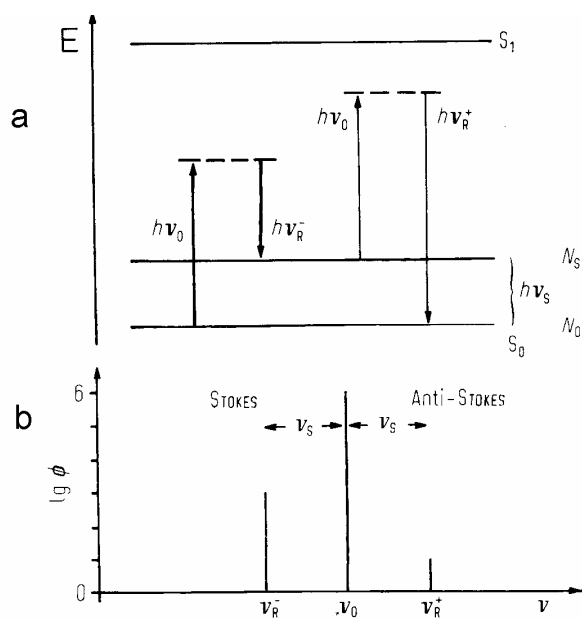


Figure 12: Principle of Raman scattering. a) Quanta with energy $h\nu_{R^-} = h\nu_0 - h\nu_s$ are scattered, when molecules are subjected to irradiation with light and go from the vibrational excited state to the vibrational ground state. Since some molecules are already in the excited state, the release of quanta of larger energy $h\nu_{R^+} = h\nu_0 + h\nu_s$ is also possible. S₀ and S₁ are the electron shells 0 and 1 of the molecule. b) Raman spectrum /102/.

2.3.3 X-ray diffraction analysis

X-Ray Diffraction analysis: XRD. X-rays are electromagnetic radiation with a very short wavelength in the range of 10^{-6} nm to 10 nm. A high-energy electron beam directed onto a cooled metal target in either an X-ray tube or synchrotron usually produces X-rays. The atomic planes of a crystal cause an incident beam of X-rays to interfere with one another as they leave the crystal. This phenomenon is called X-ray diffraction. Diffraction can occur only when Bragg's law is satisfied /103/:

$$2 \cdot d \cdot \sin \theta = n \lambda$$

λ : wavelength of the X-ray

θ : scattering angle

n : integer representing the order of the diffraction peak

The diffraction of X-ray by a crystal is illustrated in Fig.13, where the atom layers scatter certain portion of the beam.

Because the wavelength of X-rays is comparable to the size of atoms, they are ideally suited for probing the structural arrangement of atoms and molecules in a wide range of materials. X-ray diffraction is an efficient analytical technique to identify, characterize and quantify unknown crystalline materials in a mixture. XRD can be used to analyse all kind of materials, from fluid, to powder, to perfect crystals.

Each crystalline material has a characteristic atomic structure; hence it will diffract X-rays in a unique pattern. To quantify a phase a minimum content of 5% is necessary in a mixture [104,52].

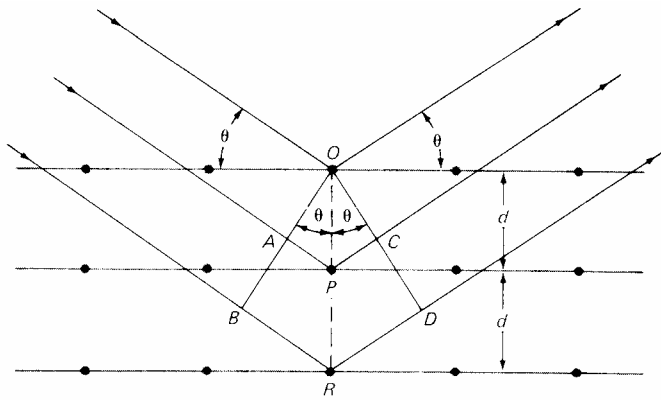


Figure 13: Diffraction of X-rays by a crystal [103]

To analyze the coatings, a Philips PW3020 diffractometer and a URD-6 diffractometer was used. CoK_{α} -radiation with secondary beam graphite monochromator was applied in the XRD analysis. The program “BGMN Autoquan” (Department of Mineralogy, TU Bergakademie Freiberg) enables quantifying the phases occurring in coatings. Rietveld refinement was carried out using structural data of different calcium phosphate phases given in the Inorganic Crystal Structure Database (ICSD).

The content of the amorphous phase was determined by mixing 80 % HA coating with 20 % SRM 676 (alumina internal standard), whereas the crystallographically disordered material fraction was determined from the discrepancy between the ratio of the crystalline phases of the coating to alumina determined from Rietveld refinements.

2.3.4 Thermal analysis - Thermogravimetry

ThermoGravimetrie (TG) is a technique by which the mass of a sample is monitored as a function of temperature or time, while the sample is subjected to a temperature control program. By this method one can determine sample purity, water, carbonate and organic content, or study the thermal reactions of sample at different temperatures.

Differential Thermal Analysis (DTA) is a method to measure the difference of temperature between a sample and an inert reference material, when both are subjected to a controlled temperature programme. DTA can therefore be used to study thermal properties and phase change /105/.

For measuring TG, an apparatus TGA 92-16.16 from SETARAM-France was used. The samples were heated from 25°C to 1400°C in air, with a heating rate of 10 K/min.

2.3.5 Scanning electron microscopy, energy dispersive X-ray analysis

The Scanning Electron Microscopy (SEM) is most widely used for surface mapping techniques. SEM uses an electron beam generated in the electron gun, which is located at the top of a column. Two electron beams are used. One beam strikes the surface of the specimen to be examined, another strikes a cathode ray tube (CRT) viewed by the operator. When the incident beam impacts on the specimen, it generates many low energy secondary electrons that are converted into photons by a CRT. The secondary electrons are collected, detected and amplified, so that a big collected signal produces a bright spot on the CRT, a small signal produces a dimmer spot. The two beams are scanned synchronously, so that every point on the specimen will have a corresponding point on the CRT (Fig.14). The whole surface will be scanned corresponding to a grid /106/.

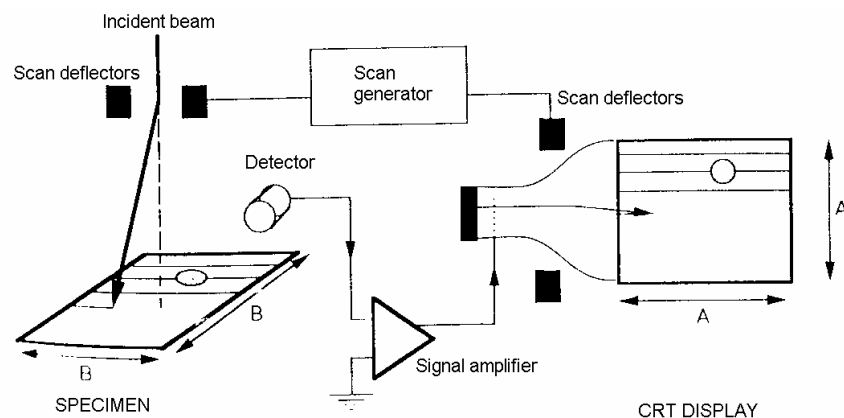


Figure 14: Schematic diagram showing the basic principles of the scanning electron microscope /106/

The SEM has large depth of field, which allows a large amount of the sample to be focused at a time. The SEM is useful for studying surface morphology.

The elemental make-up of the portion of the specimen illuminated by the beam may be determined via an X-ray energy dispersive spectrometer (Energy Dispersive X-ray analyser - EDX) attached to the SEM. When an incident beam passes through the sample, it is creating secondary electrons. It leaves the sample atoms with holes in the electron shells, where the secondary electrons used to be. Other electrons quickly neutralize those holes. In the neutralization process, an X-ray with an energy characteristic of the parent atom is emitted. By collecting and analyzing the energy of these X-rays, the elements of the sample can be determined.

The microstructure of the surface and the cross section of coatings were studied by a scanning electron microscope JEOL 6400. This SEM is equipped with an energy dispersive spectrometer (EDS, NORAN). The acceleration voltage was adjusted to 20 kV for all EDX experiments, with a take-off angle of 40°.

2.3.6 Cathodoluminescence

The Cathodoluminescence (CL) process is based on the generation of visible radiation excited when an external electron beam is radiated through a solid sample. The energy of the beam ranges from 5-25 kV, the depth of penetration is 1-3 μm . The wavelength of the CL emission corresponds to visible light from ultraviolet (UV) to the infrared (IR) when the beam returns to low energy (Fig.15). The colour and intensity of CL result from a variety of defects and impurities in the crystal structure of a mineral /107,108/.

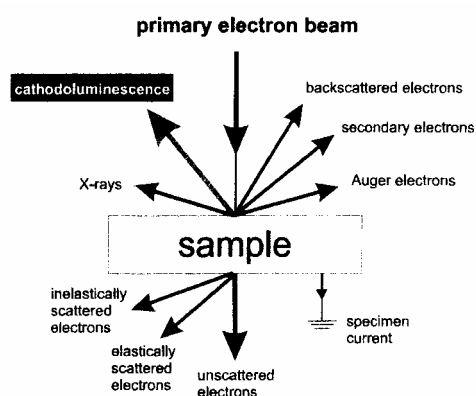


Figure 15: Schematic illustration of the interactions of an electron beam with a solid surface /108/

The cathodoluminescence can be used in mineralogical and petrological investigations of crystallographic and typomorphic properties of minerals (real structure, zonation, etc.), for identifying the minerals and mineral distribution, the reconstruction of mineral- and rock-forming processes. Furthermore, CL can provide information about phase distribution and phase transformation of technical products.

The CL analysis was conducted on thin sections (appr. 30 μm thick), which were prepared from cross section of the coating and coated with carbon to avoid electrostatic charging. A hot cathode CL microscope of type HC1-LM was used. The acceleration voltage and the electric current were 14 kV and 10 $\mu\text{A}/\text{mm}^2$, respectively. A digital video camera (KAPPA 961-1138 CF 20 DXC) recorded the CL microphotos.

3 Results and discussion

Before results of experiments will be presented, two types of amorphous calcium phosphate (am-CP) should be distinguished:

- One type originates from rapidly quenched HA particles in the plasma-spray process (am-CP/I). The chemical composition of this am-CP/I may correspond to OHA, TCP, TTCP, CaO, defect HA and/or stoichiometric nano-scaled HA.
- The other type forms on contact with an aqueous solution (am-CP/II) during either *in-vitro* incubation in simulated body fluid or *in-vivo* reaction with protein-containing body fluid.

Oxyapatite still contains a small amount of OH (chapter 1.3). Therefore, no distinction between oxyapatite and oxyhydroxylapatite will be made. Both mineral phases are collectively called oxyhydroxylapatite during the following discussion.

Two types of oxyhydroxylapatite with different amounts of vacancies were prepared by heating a stoichiometric hydroxylapatite powder at 900°C, or 1000°C for 24 h in a dry nitrogen atmosphere. A heating rate of 10 K/min was chosen. Before the powder was put in the furnace, 20 l/h of nitrogen were led through the furnace for 1 h. A nitrogen stream of 10 l/h was applied during the entire treatment process. The

oxyhydroxylapatites obtained were denoted HAP900 and HAP1000, respectively. These materials serve as references for some investigations by LRS, XRD and TG.

3.1 Structural analysis of as-sprayed and incubated coatings by NMR spectroscopy

It is well known that plasma spraying induces changes in the structure of hydroxylapatite. The characterization of such changes is difficult due to the formation of amorphous and distorted crystalline phases in the coatings. The frequently discussed oxyhydroxylapatite cannot be distinguished from stoichiometric hydroxylapatite by X-ray diffraction. However, solid-state NMR spectroscopy allows analysing the short and intermediate range structure of inhomogeneous bioconductive coatings. A two-dimensional ^1H - ^{31}P -NMR plot will give much information on the relationship between ^1H and ^{31}P of calcium phosphates in the coatings.

Figure 16 shows the ^1H and ^{31}P MAS NMR spectra of crystalline stoichiometric hydroxylapatite used as standard reference material. NMR spectra of as-sprayed coatings and of coatings immersed in r-SFB for different times are presented in Fig.17, 18.

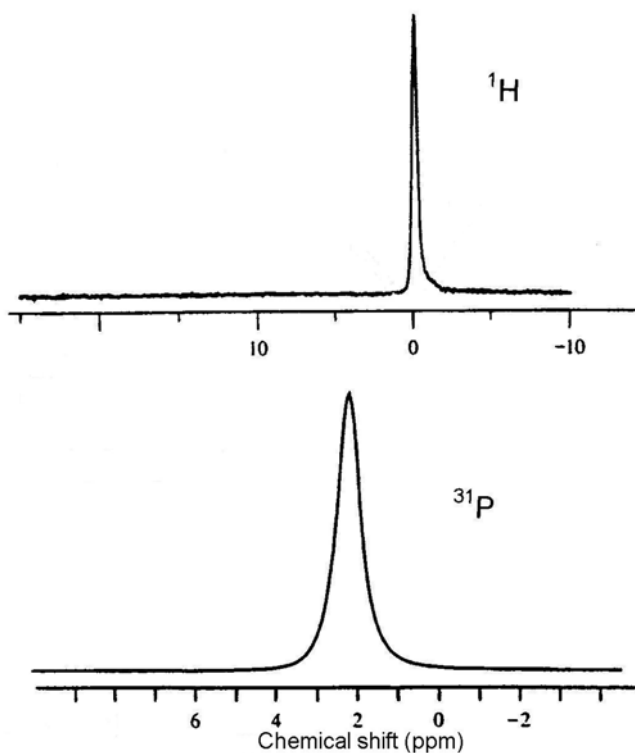


Figure 16: ^1H and ^{31}P MAS NMR spectra of crystalline hydroxylapatite

The NMR spectra of stoichiometric hydroxylapatite are characterized by only a single band position at -0.09 ppm for ^1H and at 2.3 ppm for ^{31}P , respectively. However, several additional band positions can be seen in analogous spectra of plasma-sprayed HA coatings. These band positions mark significant changes in the structure of HA caused by the high heat input during plasma-spraying, and still remain in HA coatings incubated in r-SBF at 37°C for up to 24 weeks (Fig.18). Hartmann et al. /18,48/ elaborately investigated thermally treated hydroxylapatite by NMR to simulate plasma-spraying conditions. Heat treatment results in the occurrence of four bands (A-D) in the ^{31}P spectra. The authors suggested from the double quantum ^1H correlation spectrum that all NMR bands may belong to only one dehydroxylated oxyhydroxylapatite single phase. Furthermore, in /18,48/ the relative intensity ratio of the bands C and D is nearly 2:1 at all temperatures, suggesting again only one type of phosphorus short-range structure. However, the idea of this work group that heat-treated samples are analogous to plasma-sprayed material, cannot be confirmed in the present work. The plasma-sprayed HA coatings shown in the present thesis clearly prove that different types of phosphorus-short range structures exist since the ratio of bands C and D in the ^{31}P NMR spectra varies much. The discrepancy between the thermal treatment and the plasma spraying is well understood considering that the heat treatment generates equilibrium of thermal decomposition of HA, because the sample was prepared by relatively slow heating and cooling, and therefore, it may have a more ordered distribution of cations and vacancies in the central channel of the unit cell compared to plasma-sprayed coatings. However, non-equilibrium always exists during the plasma spray process, where rapid quenching of molten particles freezes several intermediate structural states of decomposition products. It should also be mentioned that shock waves associated with impacting molten particles onto the substrate surface lead to extremely high compressive stress within the coating material /35,109/, thus intensifying the deformation and damage of the HA crystal structure.

In the coating samples immersed for up to 12 weeks, the PO_4^{3-} group of tetracalcium phosphate and β -tricalcium phosphate may contribute to the C and D bands (see also XRD results of the coatings). Moreover, poorly crystalline hydroxylapatite possesses a band at 3 ppm (corresponding to band C) in the NMR spectra too /110/.

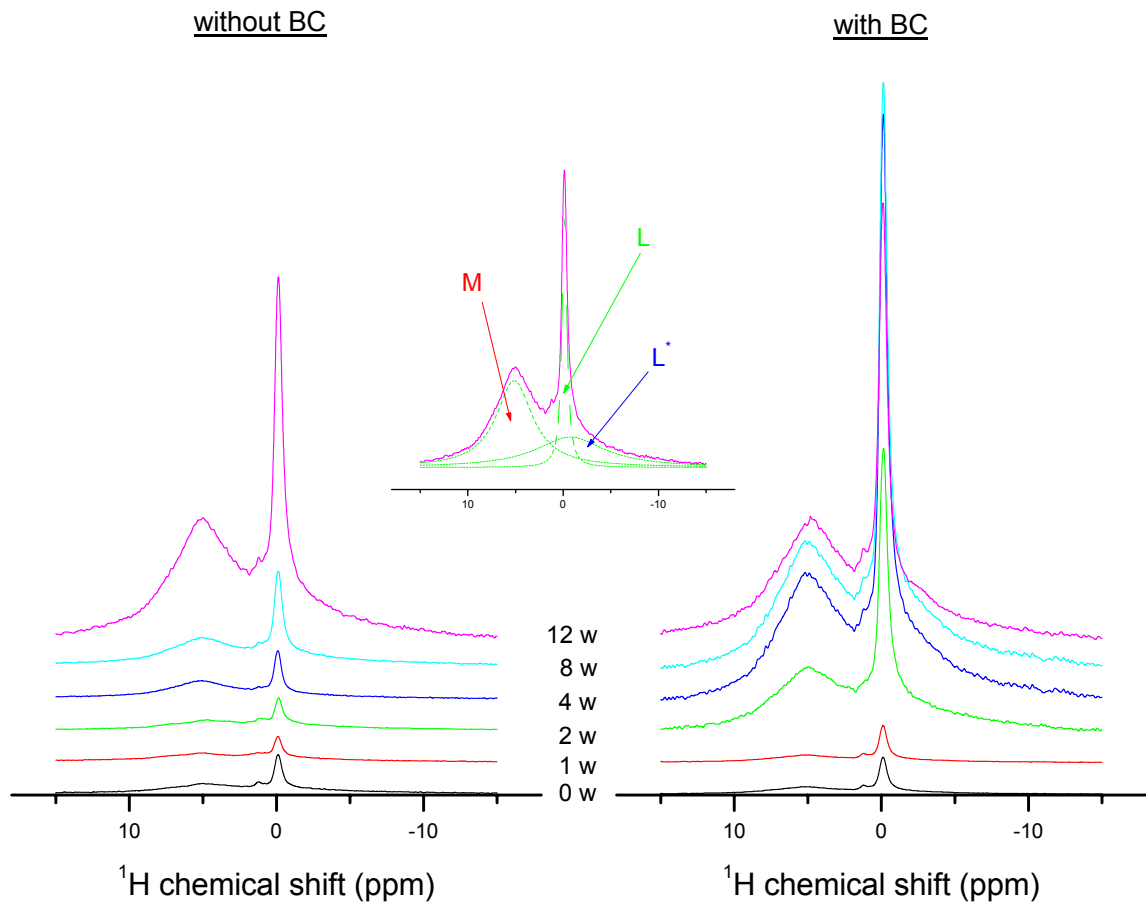


Figure 17: ^1H MAS NMR spectra of as-sprayed coatings and of coatings immersed in r-SFB for different times; L at -0.1 ± 0.1 ppm, M at 5.2 ± 0.2 ppm, L^* at -1.3 ± 0.3 ppm. Left panel: hydroxylapatite without a bond coat. Right panel: hydroxylapatite with a titania bond coat

Being incubated in r-SBF for a long time (24 weeks), the HA coatings without and with a bond coat still reveal the four characteristic band positions A, B, C and D (Fig. 18). This means that a certain quantity of distorted hydroxylapatite remains in the coatings even after long-term exposure to r-SBF. This finding can be explained by the fact that well-crystallized hydroxylapatite and distorted hydroxylapatite are very closely mixed in the dense plasma-sprayed coatings. The dense structure of the bioconductive coatings is visible in SEM images (see chapter 3.5). Consequently, owing to the dense microstructure well-crystallized HA will substantially reduce the resorption of distorted HA (including oxyhydroxylapatite), although it was reported that decomposition products of HA (such as TCP, TTCP and dehydroxylated HA) should immediately react with water vapour to form crystalline phases with

hydroxylapatite structure /111/. How can this discrepancy be explained? It must be noted that Weng et al. /111/ performed the experiment at 125°C, so that the diffusion activity of OH⁻ ions through the rather dense bioconductive coatings may be strongly enhanced. Since they determined phases by XRD, a clear distinction between oxyhydroxylapatite and hydroxylapatite was entirely missing.

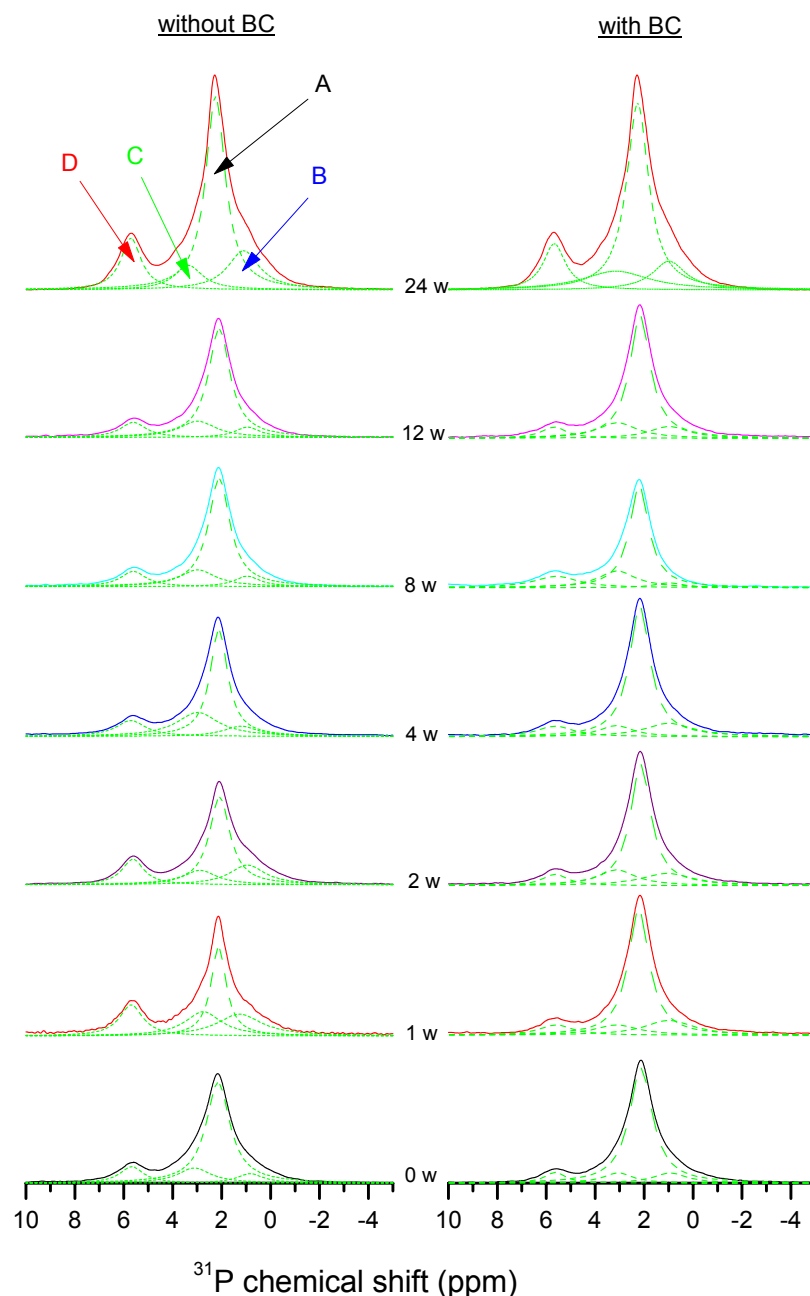


Figure 18: ³¹P MAS NMR spectra of as-sprayed coatings and of coatings immersed in r-SFB for different times; A at 2.3±0.1 ppm, B at 1.5±0.2 ppm, C at 3.0±0.2 ppm, D at 5.6±0.2 ppm
Left panel: hydroxylapatite without a bond coat. Right panel: hydroxylapatite with a titania bond coat

Hence the stability improvement of oxyhydroxylapatite found above can be considered a notable feature of the plasma spraying of bioceramics.

In the ^1H NMR spectra (Fig.17), the band L represents the well-known proton band position of the crystalline stoichiometric hydroxylapatite, while the isotropic shift band L^* could be attributed to protons in distorted HA short-range structures. The band M relates to OH^- positions missing only one neighbouring OH^- ion and indicates the existence of isolated pairs of strongly coupled protons in the channel structure. The signal N at 7.5 ppm found by Hartmann et.al. /18/ and attributed to isolated OH^- group in the channel of sintered HA is not found in the coatings examined here. Its absence obviously depends on the applied plasma spray parameters.

Typical 2D- ^1H - ^{31}P HETCOR spectra of coatings without and with a TiO_2 bond coat are shown in Fig.19. The peak A-L unambiguously belongs to an undisturbed stoichiometric hydroxylapatite short-range ordered structure. The broad band L^* correlates to the phosphorous position A too, but the intensity of that correlation peak is very low. The Lorentzian deconvolution of the peak A-L shown in Fig.20 highlights the triple nature of this peak (C-L; A-L and B-L). This fact suggests that the band B is associated with large distorted domains, but undistorted OH^- . This assignment of B is contrary to the study of Hartmann et al. /18,48/, who proposed distorted PO_4^{3-} tetrahedra at this band position located in an environment with nearby OH^- . According to /18/ and to own analyses the PO_4^{3-} environment of the coatings in the present work shows several non-equivalent positions that can be assigned to a variety of states:

- $A(^{31}\text{P}) + L(^1\text{H}) \rightarrow$ ideal hydroxylapatite (stoichiometric)
- $A(^{31}\text{P}) + L^*(^1\text{H}) \rightarrow$ undistorted PO_4^{3-} , but perturbed OH^-
- $B(^{31}\text{P}) + L(^1\text{H}) \rightarrow$ distorted PO_4^{3-} , but undistorted OH^-
- $B(^{31}\text{P}) + M(^1\text{H}) \rightarrow$ distorted PO_4^{3-} with isolated paired OH^-
- $C(^{31}\text{P}) + L(^1\text{H}) \rightarrow$ strongly distorted PO_4^{3-} , but undistorted OH^-
- $C(^{31}\text{P}) + M(^1\text{H}) \rightarrow$ strongly distorted PO_4^{3-} with paired OH^-
- $D(^{31}\text{P}) \rightarrow$ very strongly distorted PO_4^{3-} with no nearby OH^-

As shown in the HETCOR spectra (Fig.19), the peaks B-M and C-M gradually disappear with increasing incubation time. The environment around OH⁻ ions obviously tends to a proton-balanced state, where vacancies along the OH⁻ channels are partially or entirely filled. This process is enabled by diffusion of OH⁻ ions from the simulated body fluid into the coating. Definitively, the progress of such structural changes develops more rapidly in coatings with a bond coat than in one without a bond coat. Hence, due to its low heat transfer coefficient the TiO₂ bond coat plays an important role in decreasing the heat loss of molten particles during the deposition process, which essentially facilitates the reconstruction of oxyhydroxylapatite towards stoichiometric hydroxylapatite.

The analysis of the cross section of the HETCOR spectrum at the proton frequency of the band L by fitting to a Lorentzian function underscores the triplet nature of the peak in the ³¹P dimension (Fig.20). The state “undistorted PO₄³⁻, but perturbed OH⁻” is responsible for both shoulder peaks in the cross section. This finding coincides well with the result of ¹H NMR that a certain amount of distorted hydroxylapatite was not removed from the coating even when incubated for very long time up to 24 weeks.

Aue et al. /110/ reported that the introduction of CO₃²⁻ groups has a pronounced effect on the ³¹P MAS NMR line widths of calcium phosphates. In accordance with this, the line width should be approximately 5 ppm. Figure 21 shows the line full widths at the half maximum height (FWHM) at the positions A-D. Concerning the relatively small values (< 1.63 ppm) in the plasma-sprayed coatings in this work, only a small amount of carbonatohydroxylapatite was formed during the *in-vitro* test. Furthermore, the relative amount of the newly formed hydroxylapatite layer is small in comparison to that of the bulk coating. Because of that clear broadening of the peak is not expected. House /112/ found that CO₂ may affect the precipitation of HA by blocking phosphate nucleation sites.

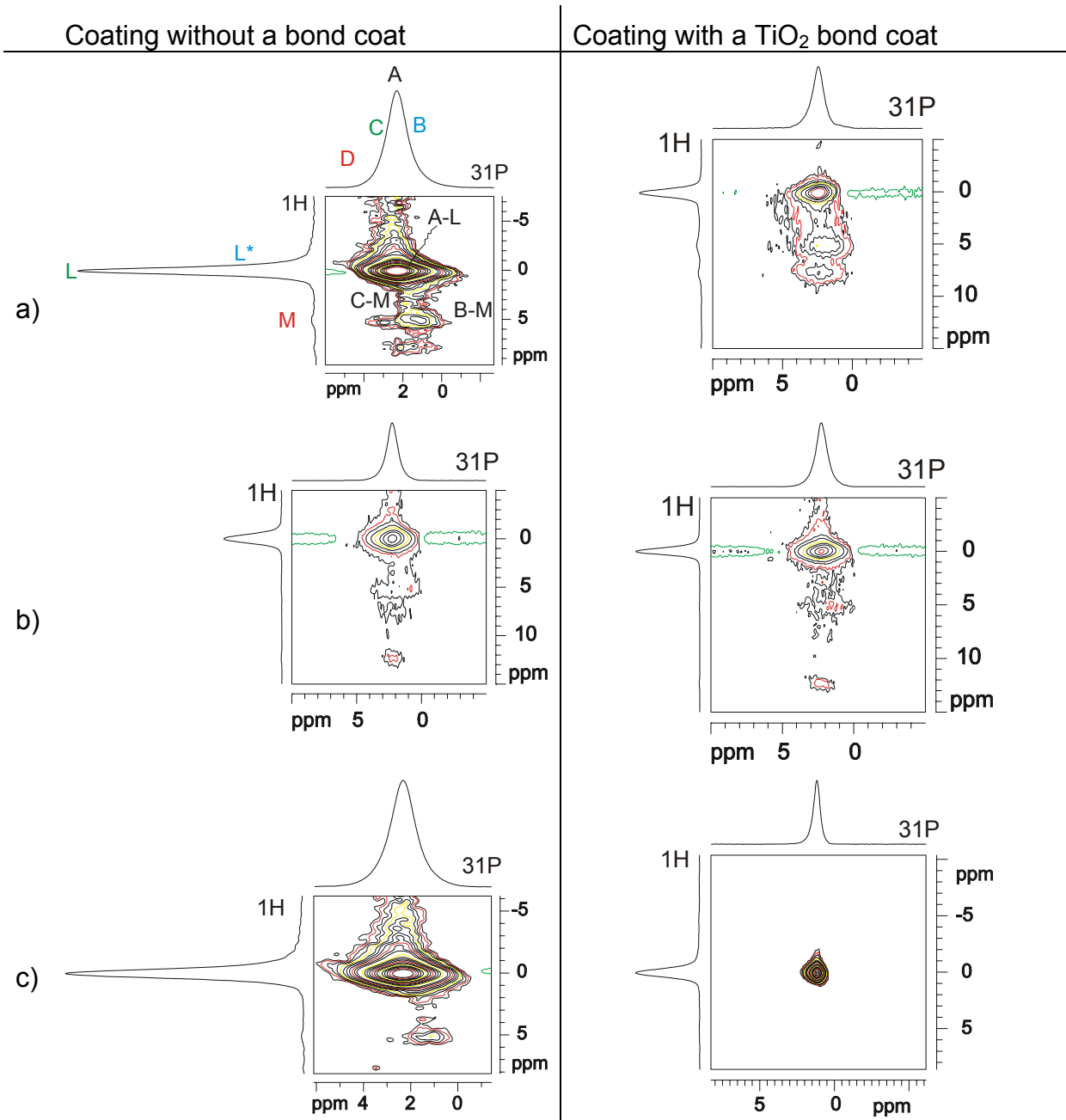


Figure 19: Typical 2D-¹H-³¹P HETCOR spectra of coatings without and with a TiO₂ bond coat immersed for a) 0 week; b) for 1 week and c) for 12 weeks

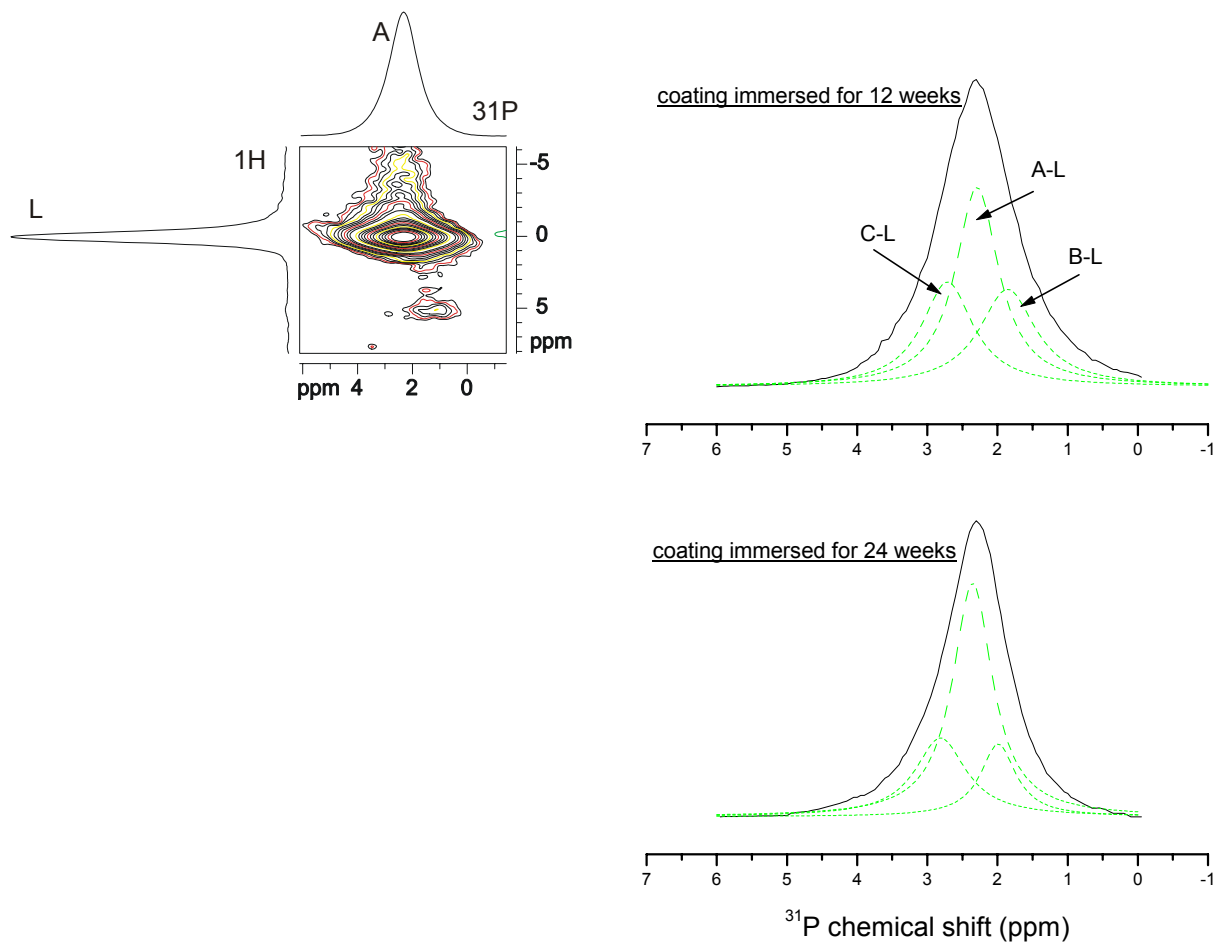


Figure 20: Fitted cross section of the 2D- ^1H - ^{31}P HETCOR spectrum at the proton frequency of band L of samples immersed in r-SBF for 12 weeks and 24 weeks, respectively. (The HETCOR spectrum of the sample incubated for 24 weeks was unfortunately lost, when the NMR group at the Department of Optics and Quantum Electronics at the Jena University was dissolved).

Figure 22 renders the relative integral intensity of the four band positions A, B, C and D of the plasma-sprayed coatings immersed in r-SBF for different periods. The intensity changes of the band position shown no systematic correlation with the immersion time. A reason for this may be the interaction between dissolution of the coating and precipitation of the new hydroxylapatite layer, whose kinetics is unknown until now. It must also be noted that all incubation experiments were conducted in closed boxes without matter exchange with the outside.

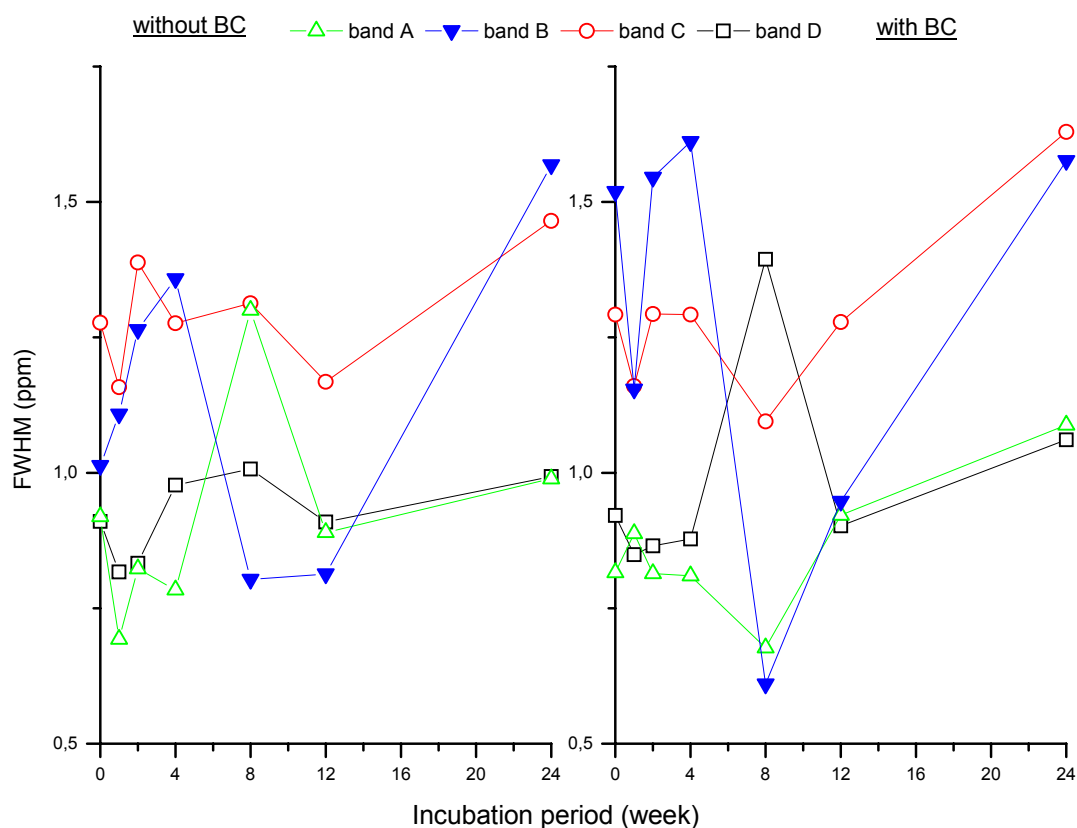


Figure 21: The full widths at half maximum height (FWHM) at the band positions A-D of coatings without and with a bond coat as a function of the incubation time.

Summarizing the NMR results, one can say that plasma spraying causes clear changes in short- and long- range structure of hydroxylapatite materials. It evokes different local environments of OH^- and PO_4^{3-} groups. The existence of these environments is strongly influenced by the set of plasma spray parameters. Rapid quenching of molten HA/ OHA particles and shock waves associated with large compressive stress complicate the structural distortion of bioceramic coatings. A long-term *in-vitro* test up to 24 weeks still shows states with distorted PO_4^{3-} / undistorted OH^- , as confirmed by NMR spectroscopy. The distorted states gradually rearrange with increasing immersion time. The 2D ^1H - ^{31}P HETCOR spectra support the assumption of a rearrangement of the phases in the HA coatings without and with a TiO_2 bond coat.

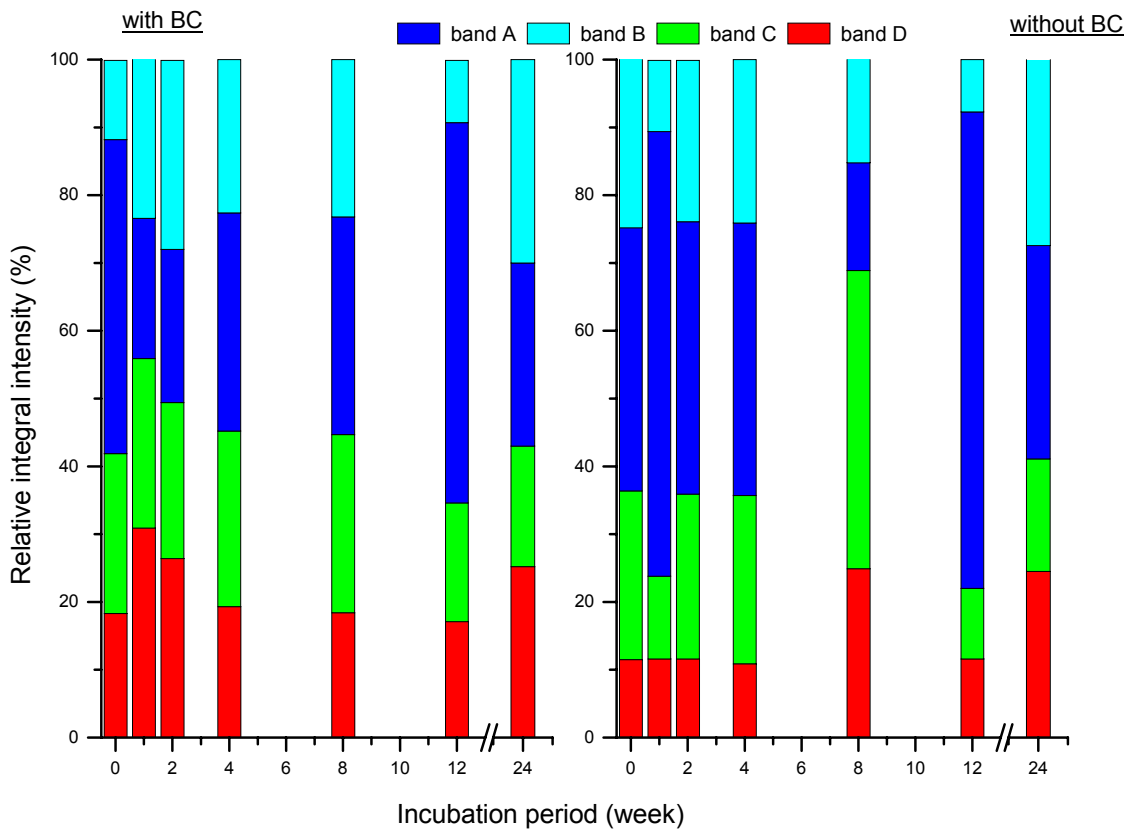


Figure 22: Influence of the incubation time on the relative integral intensity of the four band positions A, B, C and D of the plasma sprayed coatings with (left) and without a bond coat (right)

3.2 Characterization of coating surfaces by Raman spectroscopy

Laser Raman spectra of the coatings were recorded. Because of low lateral resolution of the LRS, the results obtained from the incubated bulk coatings pertain exclusively to the information about newly formed calcium phosphates. These calcium phosphates consist of nearly 100% am-CP/II (for a definition see p.35).

The vibrational normal modes of the PO_4^{3-} -tetrahedron are well known and characterized by four different frequencies: ν_1 , ν_2 , ν_3 and ν_4 (Fig.23). ν_1 at 940 cm^{-1} corresponds to the symmetric stretching mode of the P-O bonds. The ν_3 frequency arises at 1020 cm^{-1} from the triply degenerate mode involving asymmetric P-O stretching and also P motion. The ν_2 frequency at 420 cm^{-1} belongs to the doubly degenerate O-P-O bending modes, and the ν_4 at 560 cm^{-1} is due to the triply

degenerate modes of mainly O-P-O bending character. The values of the normal-mode frequencies of PO_4^{3-} -tetrahedra were obtained from LRS measurement on phosphate ions in an aqueous solution [113]. In molecular crystals, such as HA, the crystal field induces distortions of the PO_4^{3-} -tetrahedra, which give rise to shifts and splitting of the PO_4^{3-} -normal modes.

Figures 23 and 24 represent the Raman spectra of stoichiometric HA powder and of the surfaces of the prepared coatings (as-sprayed coatings and incubated coatings), respectively.

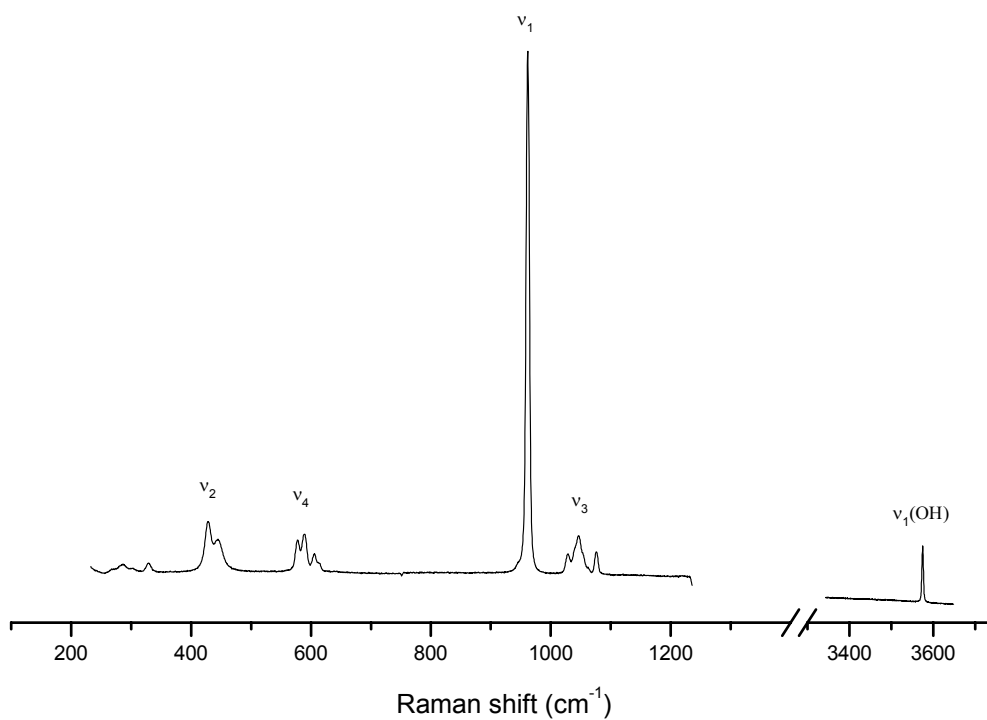


Figure 23: Laser Raman spectrum of stoichiometric HA.

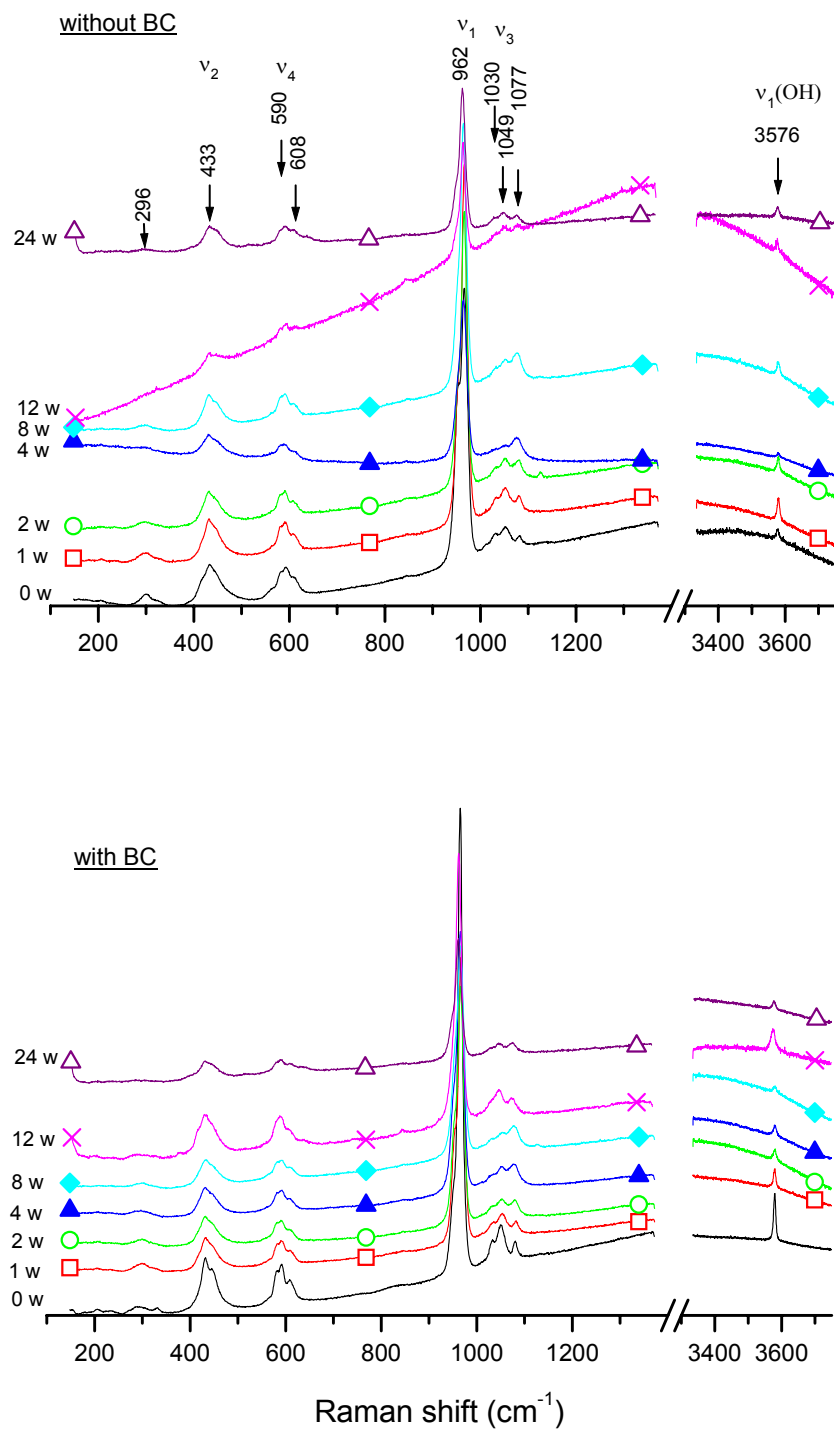


Figure 24: Raman spectra of the as-sprayed HA coatings (0w) without or with a bond coat (BC), and coatings incubated for up to 24 weeks.

It can be said that prolonging the immersion time leads to strong broadening of individual peaks of the bands ν_2 , ν_3 and ν_4 (Fig. 24). Hence the LRS spectra are

typical of very fine hydroxylapatite crystals newly formed on the coating surfaces. These small precipitates have been confirmed during the microstructural investigations (s. chapter 3.5).

The Raman spectra of the samples were analysed using a suitable mathematical model for fitting particular peaks. This analysis approach permits to detect hidden (superimposed) shoulder peaks and should supply further information on the coating structure. A Lorentzian-Gaussian deconvolution function was applied to fit the peak of band ν_1 (962 cm^{-1}), because this model delivers the best result in term of the standard deviation /116/. An example of the fitting analysis is shown in Fig.25.

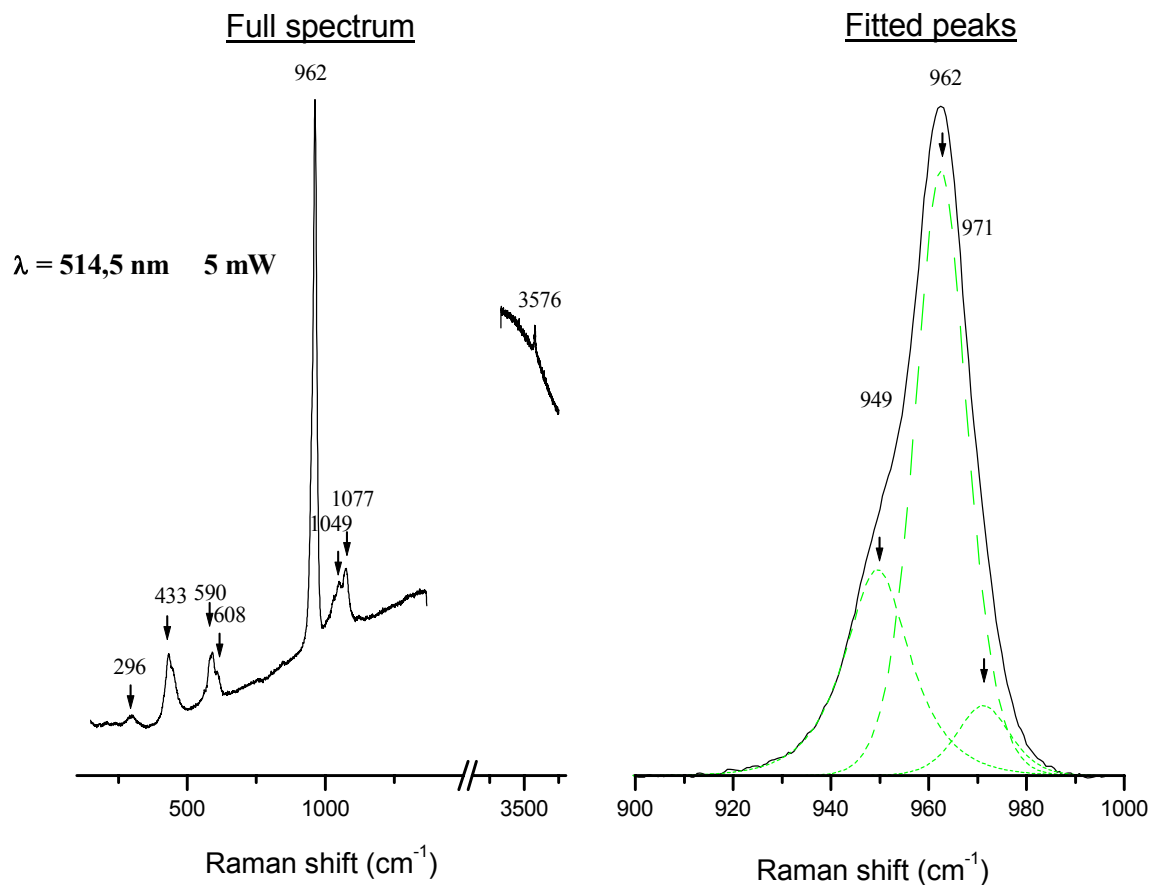


Figure 25: An example for fitting the peak of the band $\nu_1(\text{PO}_4)$ with a Lorentzian-Gaussian function.

In all samples (as-sprayed coatings with or without a bond coat, as well as incubated coatings), three typical deconvolution peaks of the band ν_1 located at 949, 962 and 971 cm^{-1} were found. Previous investigations by other authors (for example /50/)

ascribed a peak at 952 cm^{-1} (that to the standard deviation of the measurement also corresponds to 949 cm^{-1}) to an amorphous phase which always exists in plasma-sprayed hydroxylapatite coatings. In the present work, the peak at 949 cm^{-1} was also found in the spectra of the coating surface and of the thermally treated HA powders HAP900 and HAP1000 (see chapter 3). According to the XRD results, HAP900 and HAP1000 contain exclusively the crystalline phases hydroxylapatite/oxyhydroxylapatite. It can be concluded that the peak 949 cm^{-1} is also connected with changes of the environment around the PO_4^{3-} - tetrahedra, which are caused by OH^- vacancies in oxyhydroxylapatite. The intensity of the peaks at 949 cm^{-1} and 971 cm^{-1} increases with rising amount of OH^- vacancies (Fig.26; HAP1000 contains more vacancies than HAP900). On other side, hydroxylapatite formed by an aqueous process (such as secondary HA precipitated on the coating surface) provides no OH^- deficiencies. Nevertheless, the spectra of this hydroxylapatite (in the samples immersed in r-SBF for different times) present the shoulder peaks at 949 cm^{-1} and 971 cm^{-1} . Consequently, the splitting of the band ν_1 results from both a deformation of the PO_4^{3-} - tetrahedron and the nano-crystalline structure of secondary HA precipitated from the r-SBF during incubation (size effect?). A suitable condition for forming nano-crystalline phases is often achieved in the plasma-sprayed bioceramic coatings.

The calculation of the integral peak intensities at 949 , 962 and 971 cm^{-1} is used in an attempt to determine the quantitative composition of phases. The results are presented in Fig.27. The composition of the phases at the surface seems to hardly change during the immersion period of samples in r-SBF. There is an assumption that the peak intensity at 962 cm^{-1} indirectly gives information on the degree of ordering of the crystal structure of stoichiometric hydroxylapatite, i.e the higher the intensity, the higher the degree of ordering. Based on this finding, the new hydroxylapatite layer formed on the coating during immersion is less crystalline up to 4 weeks immersion, but increases in crystallinity thereafter (Tab.5). Considering the intensity ratios $I(962)/I(949)+I(971)$ it becomes obvious that in the presence of a bond coat the degree of crystallinity of hydroxylapatite is considerably higher than without bond coat (Tab.6). This is a result of the reduced distortion of the hydroxylapatite coating during plasma spraying in the presence of a bond coat. As shown in Tab.5 this is particularly obvious for the peak at 971 cm^{-1} (Fig.27).

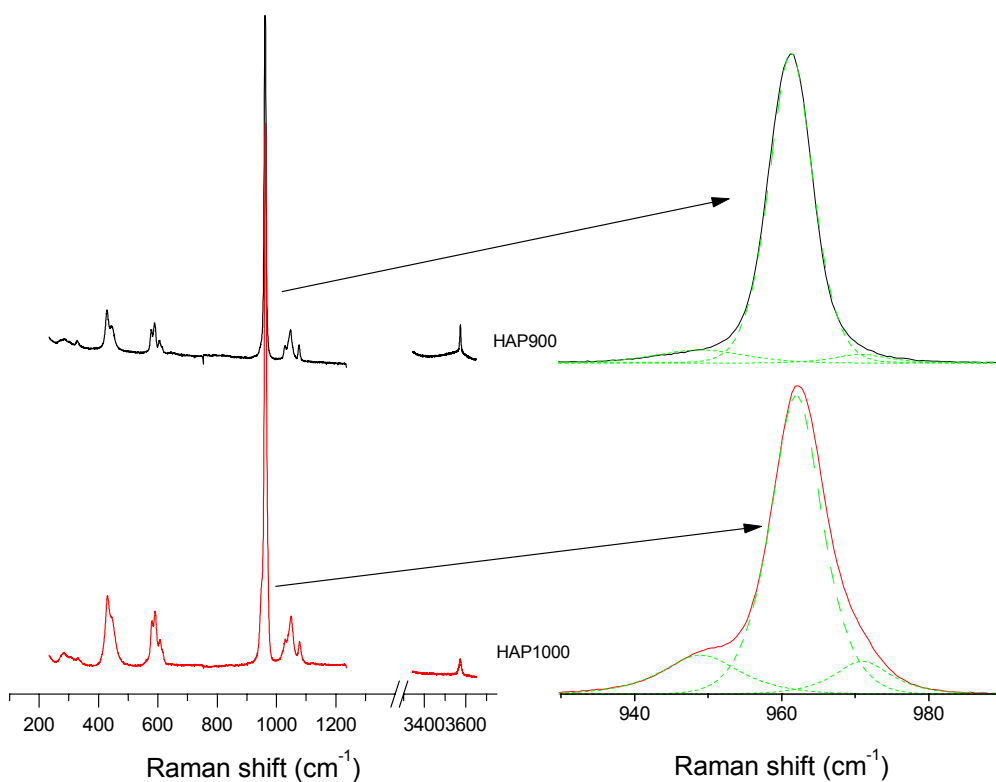


Figure 26: Raman spectra and their Lorentzian-Gaussian deconvolution of hydroxylapatite powder tempered at 900°C (HAP900) and 1000°C (HAP1000), respectively.

Table 5: Relative integral intensity (%) of HA coatings without and with a bond coat as a function of the incubation time

Incubation time (weeks)	Values are given in (%)					
	HA coating without BC			HA coating with a BC		
	Peak 949	Peak 962	Peak 971	Peak 949	Peak 962	Peak 971
0	25.6	63.4	11.0	21.8	71.6	6.6
1	30.2	57.9	11.9	31.4	60.9	7.7
2	32.1	58.7	9.2	27.9	70.0	2.1
4	33.5	56.5	10.0	28.5	69.2	2.3
8	29.3	63.7	7.0	19.8	68.2	2.0
12	29.3	60.5	10.2	25.3	71.7	3.0
24	26.9	62.1	11.0	22.2	70.1	7.7

Table 6: Integral intensity ratio $I(962)/I(949)+I(971)$ as a function of the incubation time of HA coatings without and with a Ti_2O bond coat.

Incubation time (weeks)	HA coating without BC	HA coating with a BC
0	1.73	2.52
1	1.41	1.55
2	1.42	2.33
4	1.30	2.25
8	1.75	3.12
12	1.53	2.53
24	1.64	2.34

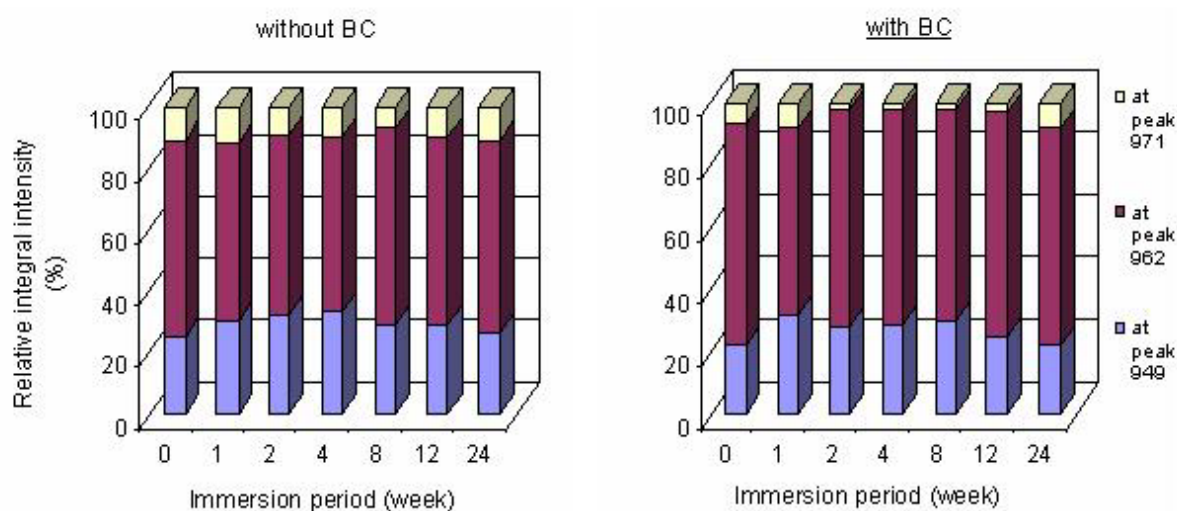


Figure 27: Relative integral intensities of the peaks at 949, 962 and 971 cm^{-1} .

It was observed that plasma spraying causes distortion of hydroxylapatite and formation of fine crystals. Hence, broadening of the FWHM of peak ν_1 (962 cm^{-1}) occurs (compare the FWHM of the HA spray powder with that of the as-sprayed coatings). Such an increase of the FWHM is also seen in the LR spectra of the thermally treated HA powders (Fig. 28).

Generally, the FWHM of the peak ν_1 of the layer newly formed on the coating surfaces decreases with increasing incubation time (> 8 weeks) of the coatings in the

r-SFB. This suggests recrystallization of a precipitated layer of secondary (bone-like) Ca-deficient hydroxylapatite. The bond coat shows no clear effect on the FWHM of peak at 962 cm^{-1} , because the Raman spectra were recorded only on the newly formed layer.

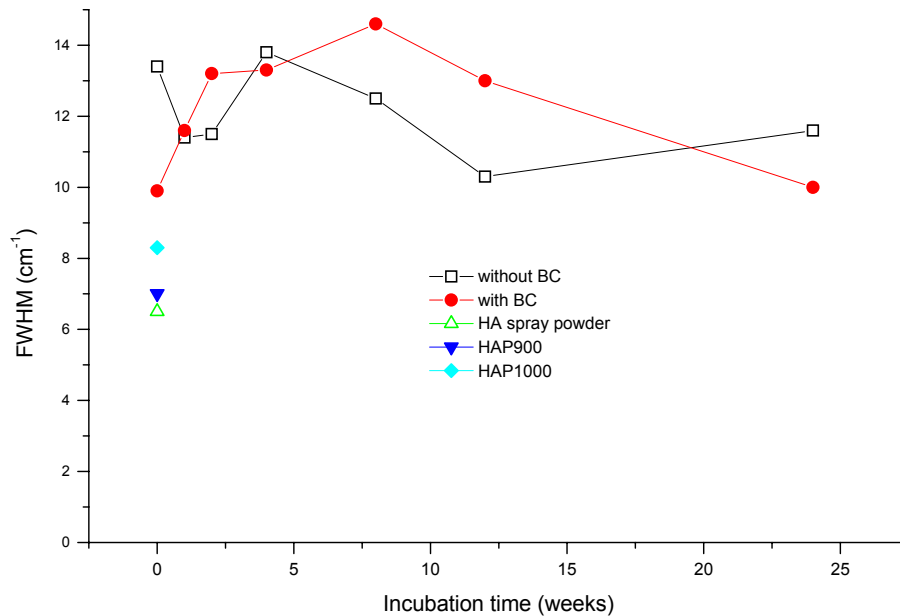


Figure 28: Full width at half maximum height (FWHM) of the 962 cm^{-1} peak of the HA coatings incubated for up to 24 weeks in comparison to that of the spray powder and of HA powders tempered at 900°C (HAP900) and 1000°C (HAP1000), respectively.

Identifying the presence of CO_3^{2-} ions in the precipitated hydroxylapatite appears to be difficult, because the band $\nu_3(\text{PO}_4)$ is strongly superimposed on $\nu_1(\text{CO}_3)$. Nelson and Williamson /117/ and de Mul et al. /118/ found a linear relationship between the FWHM of $\nu_1(\text{PO}_4^{3-})$ and a small carbonate content. CO_3^{2-} incorporation into the hydroxylapatite crystal leads to broadening of the $\nu_1(\text{PO}_4)$ - FWHM. Figure 28 evidently shows a higher $\nu_1(\text{PO}_4^{3-})$ - FWHM of the new HA layer compared to that of the spray powder. Combining this result with findings of the previous studies in /117,118/, one can draw the conclusion that the newly formed hydroxylapatite on the incubated coatings retains some CO_3^{2-} ions. This newly formed layer provides bone-like apatite.

3.3 Investigation of phases in coatings

Heimann /140/ and Graßmann & Heimann /141/ proposed a model of thermally induced phase transformation in a spherical hydroxylapatite powder particle during a short residence time of the particle in the plasma jet (Fig.29). A parabolic temperature gradient is considered according to Fourier's Law. The innermost core is still at a temperature below 1550 °C showing HA and OHA. The next shell has been heated to a temperature above the incongruent melting point of hydroxylapatite (1570 °C), and consists of tri- and tetracalcium phosphates. The outermost shell of the particle consists of CaO (as the only unmelted compound) + melt (L). In this shell, evaporation of P₂O₅ shifts the composition along the liquidus towards CaO – richer phases. The temperature increases to well beyond 1800 °C. When the particle impacts onto the implant surface to be coated the each shells are mixed to others. This leads to an inhomogeneous layer in which HA, OHA, TCP (α' - and β -TCP), TTCP and CaO are interspersed. At the immediate interface to the solid substrate a very thin layer of amorphous calcium phosphate (ACP) is formed by rapid quenching of the outermost melt layer.

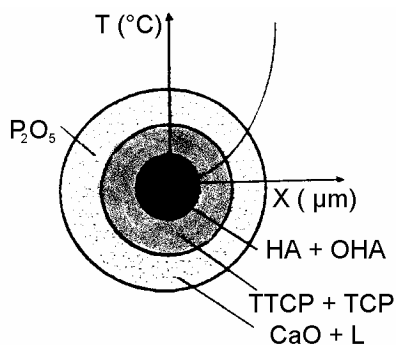


Figure 29: Schematic model of the thermal decomposition of a spherical hydroxylapatite particle subjected to high temperature in a plasma jet /140, 141/.

It should be noted that XRD is unable to distinguish between hydroxylapatite and oxyhydroxylapatite with different OH content. In this chapter, all these phases are considered as HA. It means that when hydroxylapatite is mentioned, it also stands for OHA or mixtures of HA/OHA.

The XRD patterns of plasma-sprayed HA coatings without and with a bond coat are given in Fig.30. The patterns seem to be similar to that of HA powder, but interplanar spacings of TCP, TTCP and CaO are also found in the coating. Broadening of the HA interplanar spacings in the patterns of plasma-sprayed coatings was induced in

comparison to the HA powder. This enhanced reflex width is principally caused by lattice distortion as well as by crystal sizes in the nanometre range.

A quantitative phase analysis using Rietveld refinement was performed on the diffractograms obtained. It was observed that the contents of CaO, β -TCP and TTCP decrease noticeably with increasing incubation time of up to 12 weeks with consecutive increase of the HA content (Fig.31). The reason for this is the higher solubility of these phases (Fig.32). Moreover, the reaction of TCP and TTCP to HA contributes to lower their amount.

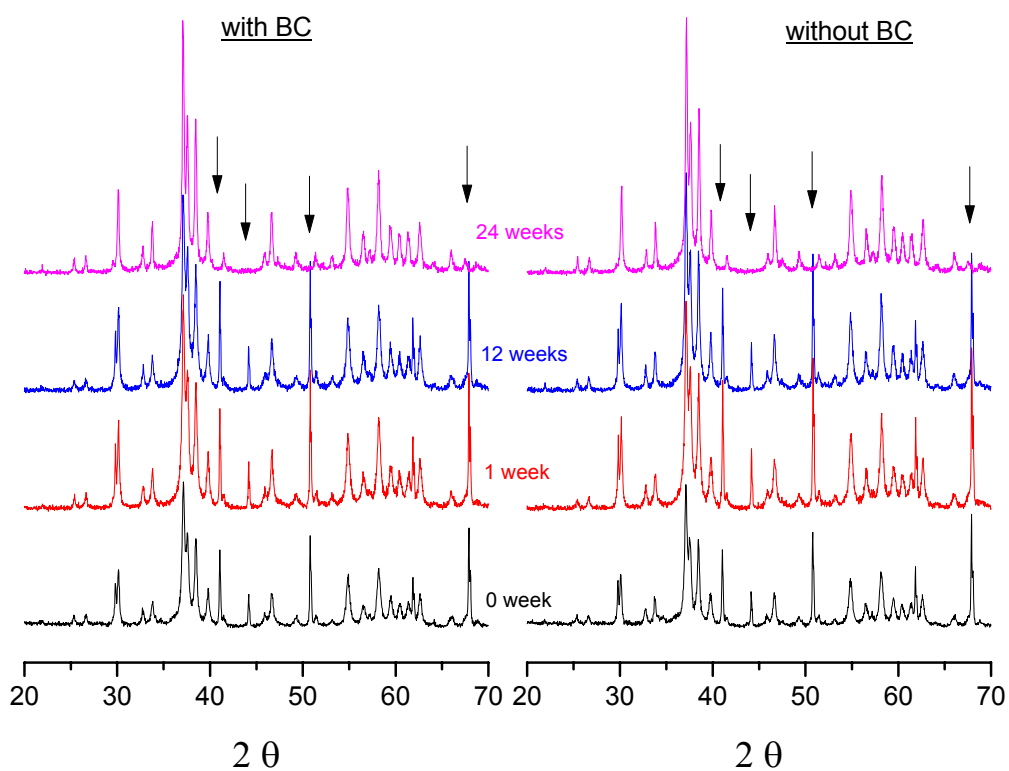


Figure 30: XRD pattern of plasma-sprayed coatings without and with a bond coat (BC) immersed for different times. Arrows mark reflexes of corundum, which was added to the powder to determine the quantity of amorphous phases. Reflexes of TCP, TTCP and CaO are not marked in the figure.

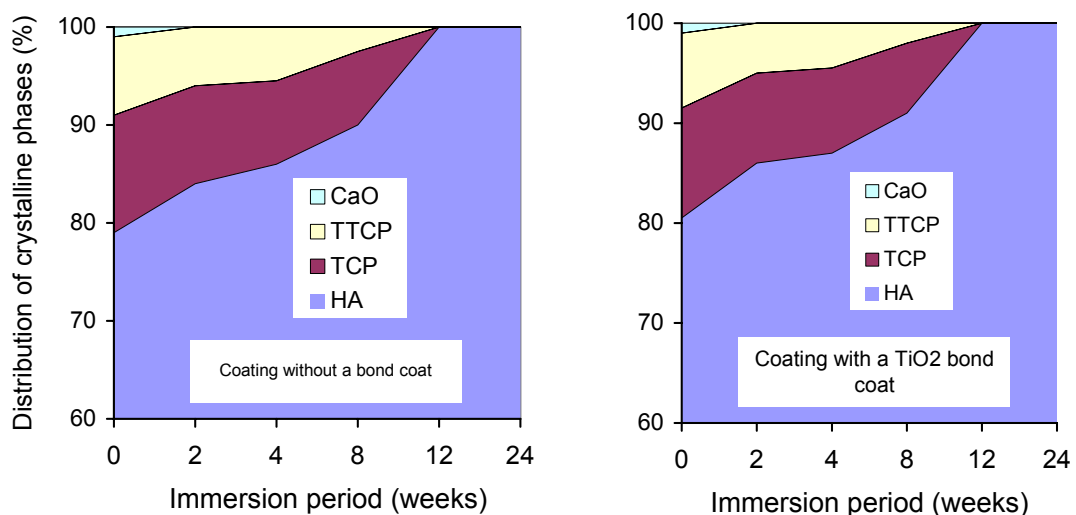


Figure 31: Percentage distribution of crystalline phases in coatings as a function of immersion time in r-SBF at 37°C.

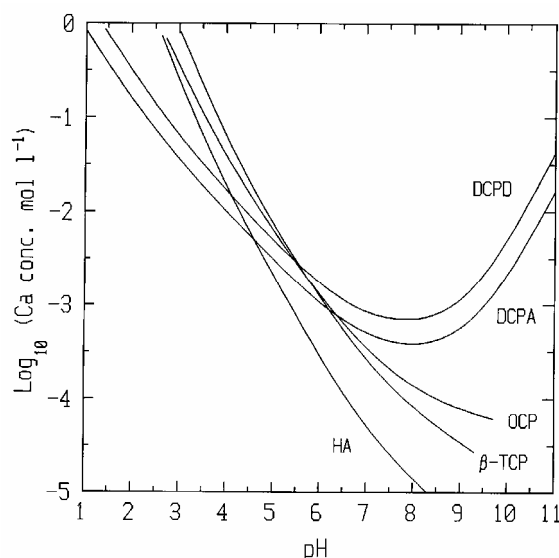


Figure 32: Solubility isotherms of calcium phosphate phases in the system $\text{Ca}(\text{OH})_2\text{-H}_3\text{PO}_4\text{-H}_2\text{O}$ at 37 °C. DCPA: dicalcium phosphate anhydrate (monetite); DCPD: dicalcium phosphate dihydrate (brushite); HA: hydroxylapatite; OCP: octacalcium phosphate; β -TCP: tricalcium phosphate (whitlockite) /6/.

After immersion for > 12 weeks the coatings contain only HA and amorphous calcium phosphate (ACP). It is obvious that the loss of OH^- group during plasma spraying and the incorporation of OH^- from water into the lattice of OHA or by participating in the reaction of $\text{TCP} + \text{TTCP}$ is a reversible process. Weng et al. /133/ showed the essential role of water in the conversion process from amorphous to crystalline

apatite in plasma-sprayed coatings. In their study /133/, an increase in crystalline HA was explained not due to removing the amorphous calcium phosphate by dissolution, but by reconstruction by uptake of water of decomposition products such as TCP, TTCP and amorphous phases to crystalline HA. Moreover, the water molecules also combine with amorphous oxyhydroxylapatite, so that the OH⁻ groups re-occupy the lattice vacancies on the missing OH⁻ sites. All that leads to raising the amount of HA in a water-treated plasma-sprayed coating. Furthermore, it was observed in the present thesis that the reaction of TCP, TTCP and water to hydroxylapatite in the coating evolves faster than the conversion of distorted HA to well-crystallized HA. While TCP and TTCP are absent after 12 weeks incubation (Fig.31), distorted HA is still present up to 24 weeks incubation time (chapter 3.1, Fig.17, 18)

A quantitative XRD analysis was conducted on the as-sprayed coatings and on the coatings leached in r-SBF for 1 and 12 weeks, respectively to determine the amount of the amorphous phase. The results are presented in Fig.33.

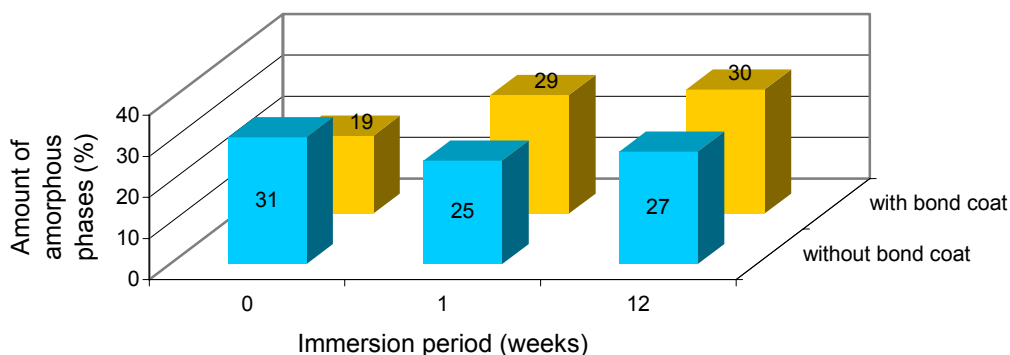


Figure 33: Amount of amorphous phases in the HA coatings determined for several incubation periods.

In these samples an amorphous phase was always detected. The nature of the amorphous phase is different for the as-sprayed coating and the incubated coatings. On one side, the amorphous phase in the as-sprayed coatings belongs to type am-CP/I and contains a large concentration of OH⁻ vacancies. On the other side, the amorphous phase in the coatings incubated in an aqueous solution consists mainly

of type am-CP/II and perhaps residual am-CP/I. The type am-CP/II consists of very fine crystals and thus appears amorphous to the X-ray. It forms by a precipitation process, and OH⁻ vacancies are absent in this amorphous phase. This means that as the immersion period extends, the content of am-CP/I is decreasing and the content of am-CP/II is increasing. The full quantitative XRD can only determine the total amount of the both amorphous phases, but cannot distinguish between am-CP/I and am-CP/II. Figure 33 shows that the TiO₂ bond coat efficiently reduces the content of the amorphous phase (type am-CP/I) in the as-sprayed bioconductive coating. However, the sum of the amorphous phases (am-CP/I and am-CP/II) in the bond coat system is roughly the same as that of the system without the bond coat after immersion for more than 1 week in r-SBF. This finding leads to the result that the system with a TiO₂ bond coat can considerably promote the formation of new HA crystals, which enables a high integrating potential of the implant with bone. The high bioactivity of the implant system with a bond coat is demonstrated here. Concerning this aspect, an implant based on a TiO₂ bond coat offers decisive advantage compared to implants without a bond coat.

When being immersed for > 12 weeks, the plasma-sprayed coatings provide solely hydroxylapatite (or in other words calcium phosphates with the same lattice parameters as HA, e.g. oxyhydroxylapatite or non-stoichiometric HA) as crystalline phase (Fig.31).

3.4 Differentiation between coating surface and coating boundary

To differentiate the material at the coating surface and at the boundary HA/ bond coat, some TG experiments were performed with following samples:

- Samples prepared from surface area and from boundary area of the as-sprayed coating with a bond coat. These samples are marked as “surface/ as-sprayed” and “boundary/ as-sprayed”
- Samples prepared from surface area and from interfacial area of the coating with a bond coat, whereas the coating was immersed in r-SBF for 12 weeks. These samples are marked as “surface/12w” and “boundary/12w”

- Powders HAP900 and HAP1000 were also involved in the TG. This will facilitate some additional insight into the coating behaviour.

The surface area and the boundary area for sample preparation is shown in Fig.34.

TG will deliver some background information, which explains the existence of OH-free calcium phosphate in the coatings. Moreover, the diffusion kinetics of OH⁻ ions into the lattice of OHA may be estimated.

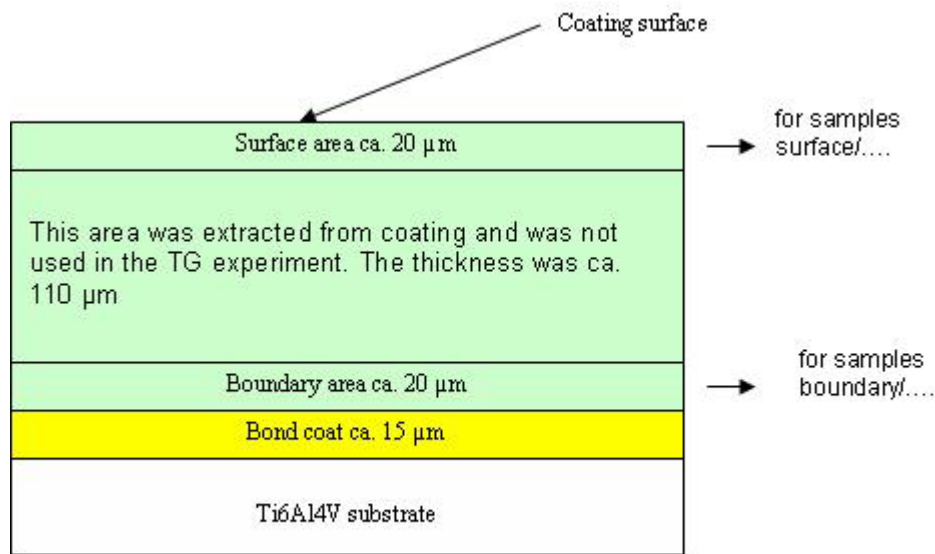


Figure 34: Schematic cross-section of plasma-sprayed coatings indicating the areas from which the samples were prepared for the TG experiment.

Figure 35a shows the behaviour of the powder materials prepared from the coatings and the tempered powders HAP900/ HAP1000 during heating in an air atmosphere.

On heating below 900°C, the samples will gain weight. This weight gain accounts for the hydroxylation of OHA by incorporating OH⁻ from surrounding humidity. The degree of an increase in weight depends strongly on the thermal history of the treated HA. The results reveal that the powder treated at 1000°C absorbs more water vapour than the one treated at 900°C. The powders from as-sprayed coatings (samples surface/as-sprayed and boundary/as-sprayed) also increase their weight during the TG test. However, their behaviour is more distinct than that of HAP900/ HAP1000. The reason is the extremely high temperature in the plasma jet /35,119/. Furthermore, if HA powder was treated at higher temperature, the position of maximum weight gain shifts to a higher temperature (compare: 500°C for HAP900,

620°C for HAP1000 and 840°C for surface/as-sprayed and boundary/as-sprayed). This finding confirms that the reactivity of thermally treated hydroxylapatite powders (HAP900, HAP1000 and powder from the as-sprayed coating) depends directly on the degree of distortion of the crystal structure. The distortion degree increases in the order: HAP900 < HAP1000 < powder from the as-sprayed coating.

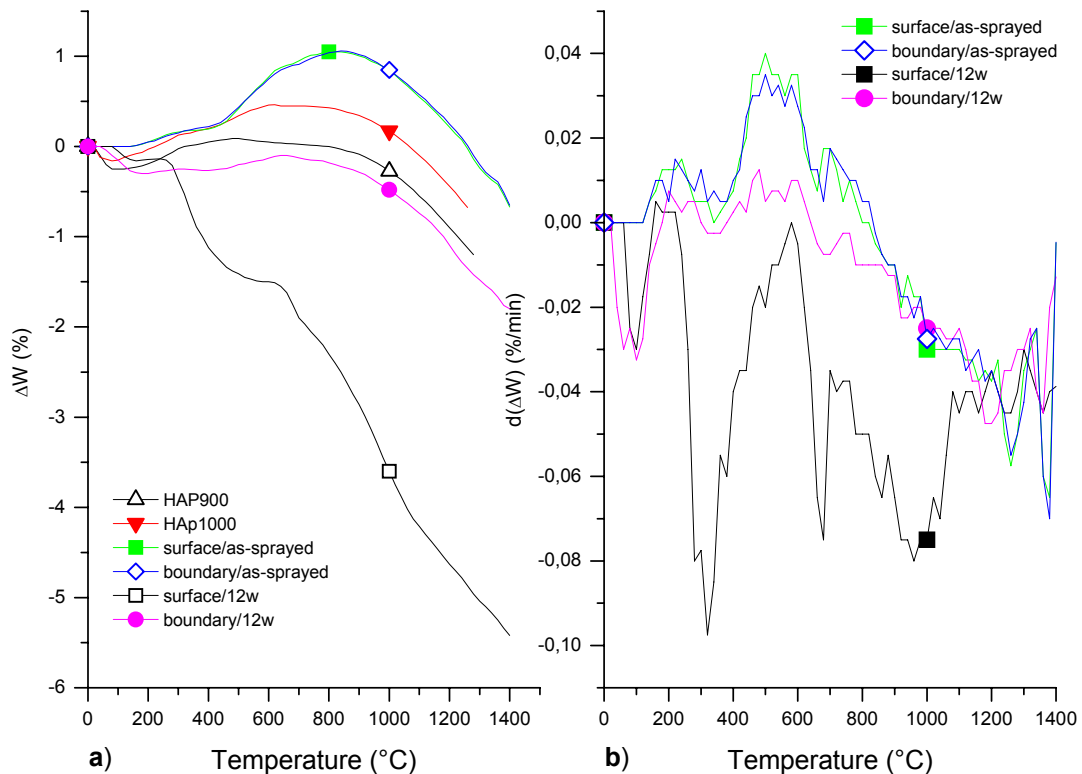


Figure 35: a) Weight changes (ΔW) of the samples during heating; b) weight change rate $d(\Delta W)$ of some selected samples during heating at a rate of 10 K/ min.

Concerning the TG results of the as-sprayed coatings, the powders prepared from the surface and from the boundary between coating/ substrate do not differ. However, microstructural analysis by Laser Raman spectroscopy suggests a different crystal structure of mineral phases in both powders (s. chapter 3.7). Obviously, while the powders contain the same amount of remaining OH^- ions, but they have different structures. Hence the TG curve suggests that the HA spray powder lost about 1.06 % (of a total of 1.79 % in the structure of HA, i.e. 60%) of water during plasma spraying.

The difference between the maximum and the minimum value in the TG curve is 1.70 – 1.71 % for the samples surface/as-sprayed, boundary/as-sprayed or boundary/12w (Fig.35a). This difference is nearly the same as the total content of water in stoichiometric HA (1.79%). In fact, the loss of water (accurately: OH⁻ ions) can be compensated by thermal treatment of the HA coatings in an environment. The process takes place very quickly, e.g. within a few minutes during the TG test. An optimal treatment temperature is essentially determined by the thermal distortion degree of the HA. At this temperature and at a given heating rate (10 Kmin⁻¹) a maximum content of distorted HA is converted in the coating, i.e. at 840°C in the as-sprayed coating and at 660°C in a coating immersed in r-SBF for 12 weeks.

Assuming that the maximum of weight gain corresponds to 100 % conversion of OH-deficient HA to stoichiometric HA, the relationship between the degree of conversion and the temperature can be described in Fig.36 for an applied heating rate of 10 Kmin⁻¹.

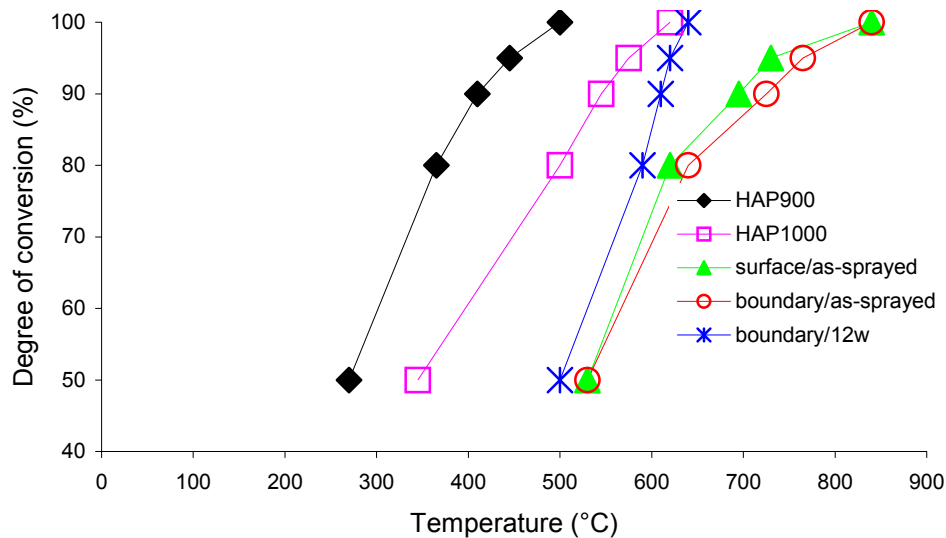


Figure 36: Relationship between the temperature and the degree of conversion of hydroxylapatite in samples prepared from bioceramic coatings in comparison with the HA powders tempered at 900°C (HAP900) and 1000°C (HAP1000).

It is clear that at the same heating rate of 10 Kmin⁻¹ a higher temperature is necessary for an increased conversion degree. The temperature for maximum conversion (100%) shifts to a higher level, if the temperature during the thermal

history of hydroxylapatite increased (Fig.36; the temperature during the thermal history increases in the order: sample boundary/as-sprayed > HAP1000 > HAP900). Incubation of the plasma-sprayed HA coating leads to the lower amount of OH⁻ vacancies. Therefore, the conversion temperature of the surface of the incubated sample is slightly lower than that of the sample boundary/incubated.

After the bioceramic HA coatings have been brought in contact with simulated body fluid, the thermal behaviour of the coatings changes drastically (compare TG of samples surface/as-sprayed with surface/12w and boundary/12w, Fig.35a). The coating surface gradually loses weight during temperature increase. The relatively high weight loss is attributed to the fact that the nano-crystalline precipitated calcium phosphates have a very high specific surface, which physically bounds a lot of water molecules /98/. This water is fully released during thermal heating. Moreover, the r-SBF contains an organic buffer compound (HEPES). A part of that compound is enclosed in the coating and burnt out during the TG test. A broad exothermic peak of the heat flow curve (Fig.37) suggests burnout of organic compounds. Furthermore, chemicals from the r-SBF like carbonates and sulfates precipitating within the coating also evaporate during heating of the TG sample. All that causes additional weight loss. In contrast to the material from the surface, the material at the boundary shows only a slight increase in weight during heating from 200°C up to 680°C (Fig.35a). At higher temperature the mass of the boundary sample decreases. This points to the still present OH-deficient hydroxylapatite at the boundary. It means that the peaks detected at around 1.3 and 5.2 ppm by ¹H-MNR in the sample immersed for 12 weeks (s. chapter 3.1) originate mainly from the boundary material. One explanation for the presence of such an OH-deficient HA at the boundary could be that the dense structure of the coatings identified by SEM hinders the diffusion of OH⁻ ions into deeper coating areas. Keller /120/ discussed the diffusion kinetics of OH⁻ ions. From available data, the reaction constant at 37°C can be calculated. The value is extremely low (ca. $1.34 \cdot 10^{-18}$). The total weight loss of the coating boundary is nearly 1.8% (including 0.3 % physically adsorbed water), evidence that no other compounds than OH⁻ diffused through the coating to the boundary. Hence, at the boundary HA coating/ bond coat, the reconstruction process of hydroxylapatite is controlled predominantly by incorporating OH⁻ ions and by re-combination of TCP and TTCP.

Using the mass change rate to indicate the OH^- diffusion rate (the higher the mass change, the higher the OH^- diffusion), the temperatures at which the high diffusion rate of OH^- starts are similar for all samples (HAP900, HAP1000, surface/as-sprayed, boundary/as-sprayed, boundary/12w). This point is located at 460-480°C (Fig.35b). If annealing of the bioceramic composite HA/ BC/ Ti6Al4V would be performed within the temperature range 460-480°C, high crystallinity could be obtained without compromising the strength of the implant, because the hexagonal-cubic transformation in Ti6Al4V takes place only around 880°C [121].

According to [120,14], the diffusion of OH^- ions determines the decomposition rate of HA. In a reverse reaction, it defines the reconstruction of HA from OHA or TCP/TTCP. The higher the reconstruction rate, the higher is the reactivity of OHA or TCP/TTCP. Figure 35b presents the rate of mass change during heating during the TG test. Consequently, the high temperature of the plasma jet causes a higher amount of OH vacancies in HA than in HAP900 or HAP1000. Similarly, the HAP1000 has a higher amount of OH vacancies than the HAP900. After immersion of the plasma-sprayed bioceramic coatings for a certain time in r-SBF, some OH vacancies will be reoccupied. This causes a decrease of the diffusion rate of OH^- ions along the c-axis in the HA lattice. Therefore, the water adsorption rate of the coatings clearly decreases during the TG test (compare ΔW of the sample boundary/as-sprayed with that of the sample boundary/12w). Since the reactivity relates directly to the amount of free enthalpy in a system one can say that the free enthalpy of the coatings is reduced during the immersion process. Interestingly, the weight change rates at high temperature (900°C – 1200°C) are the same for the samples surface/as-sprayed, boundary/as-sprayed and boundary/12w. In other words, the diffusion of OH^- ions in the temperature range 900 – 1200°C is nearly independent of the thermal history of the HA powder.

At low temperatures the diffusion rate (a temperature dependent factor) of OH^- ion is very low. This directly affects the slow reconstruction rate of distorted HA towards HA. This reason is, among other causes, responsible for the existence of residual hydroxylapatite with a defect structure within the coatings after incubation in r-SBF for a long time.

Figure 37 shows the heat flow during the TG experiment. An increase of the heat flow rate in the temperature range 25 – ca. 600°C is established by the

transformation of a glassy amorphous phase within the plasma-sprayed coating into crystalline phases. Due to high loss of physically absorbed water, the heat release of the sample prepared from the surface of the coating immersed for 12 week is less sharp than that of the sample boundary/12w. Finally, burn-out of organic compounds in the sample surface/12w is responsible for the second heat flow peak at approximate 800°C. This strongly supports the idea that the buffer compound is well enclosed in the newly formed bioconductive layer on the coating.

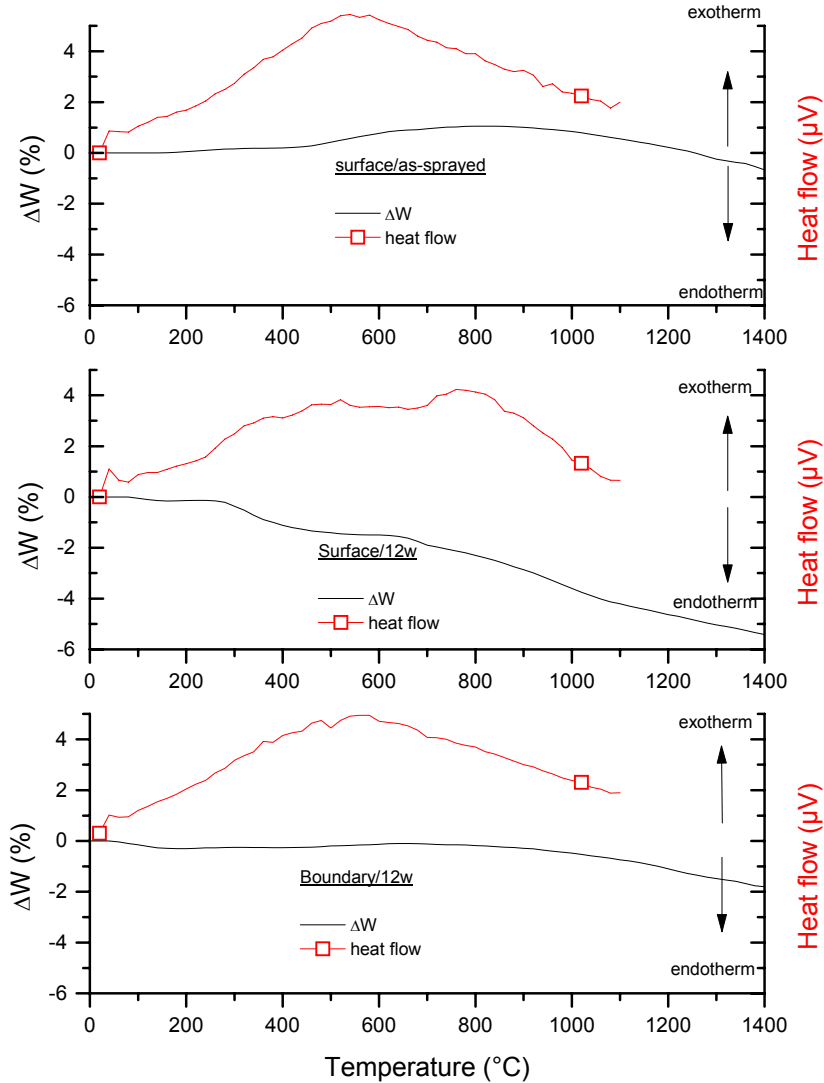


Figure 37: Weight change (ΔW) and heat flow curves of some samples investigated.

3.5 Changes of the coating composition and morphology during incubation

The SEM images show no clear difference of the morphology of the surfaces and the cross-sections between coatings with and without a bond coat (Fig.38).

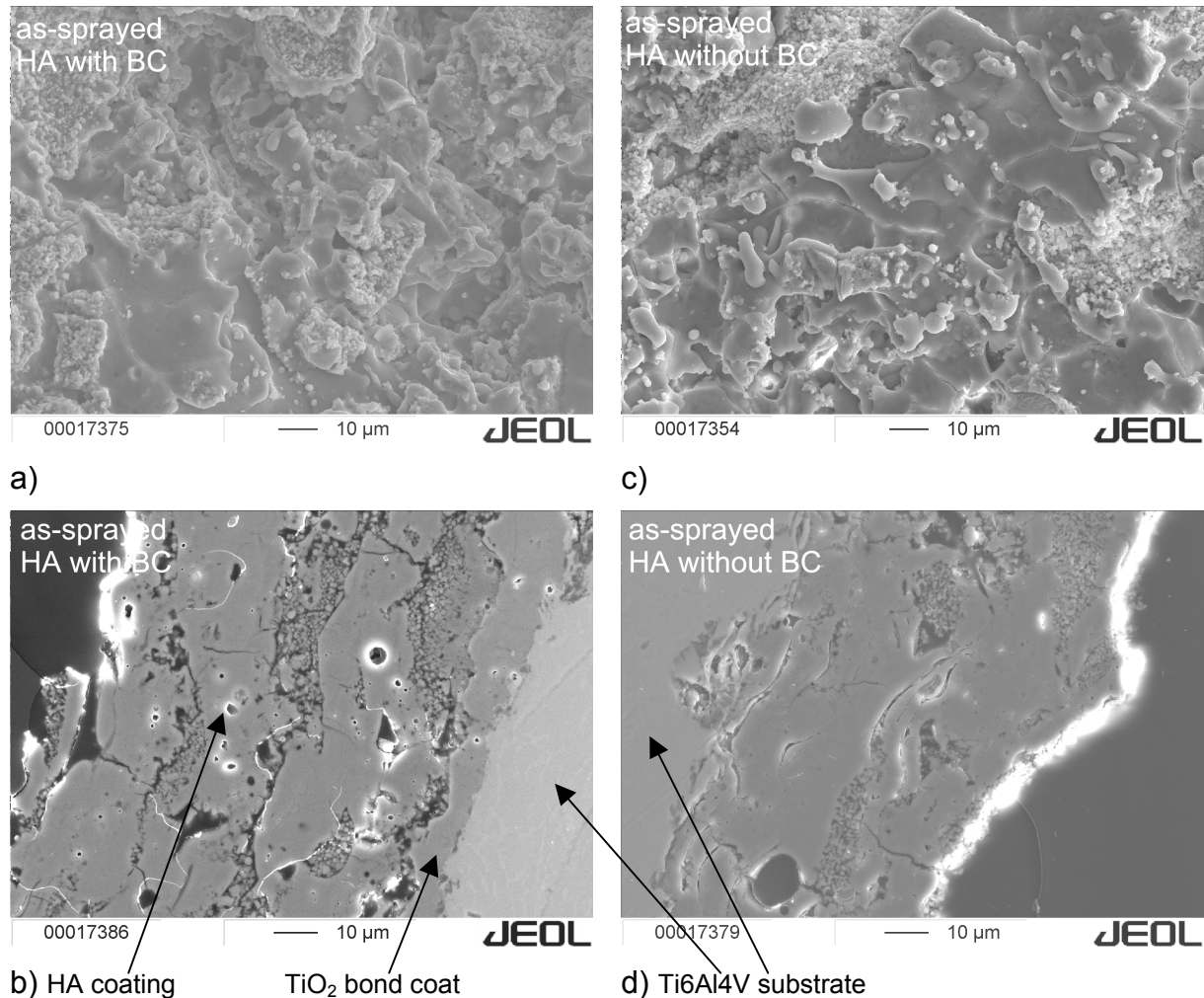


Figure 38: SEM images of as-sprayed coatings: a) surface and b) cross-section of a coating with a bond coat; c) surface and d) cross-section of a coating without a bond coat.

A dense layer of TiO₂ (see chapter 2.2.1) is visible in the sample with a bond coat (Fig.38b). Some cracks formed due to tensile stresses within the coatings, which occurred during quenching of molten HA particles. This phenomenon is independent of the types of sample (simple coatings or coatings with a bond coat). In the as-sprayed coatings un-molten particles (loose primary HA particles) are found attached to well molten ones. A cause for these loose HA particles may be the impact of solid, brittle HA particles with high velocity onto a relatively cold substrate. Such un-molten

HA aggregates are in spongy areas of the cross sections of samples. Their presence may assist in stopping crack propagation through the whole coating down to the substrate.

After being incubated in r-SBF for 1 week, primary fine HA particles are not found anymore at the surface of the coatings, but still exist within the coatings. A thin layer of newly precipitated HA forms on the bulk coatings (s. LRS-results in chapter 3.2). The precipitation transformed the surface from a sharp-edged morphology to rounded forms (Fig.39). These shapes are similar to those pictured in /60/. The thickness of the new HA layer is found to increase with immersion time (Fig.40).

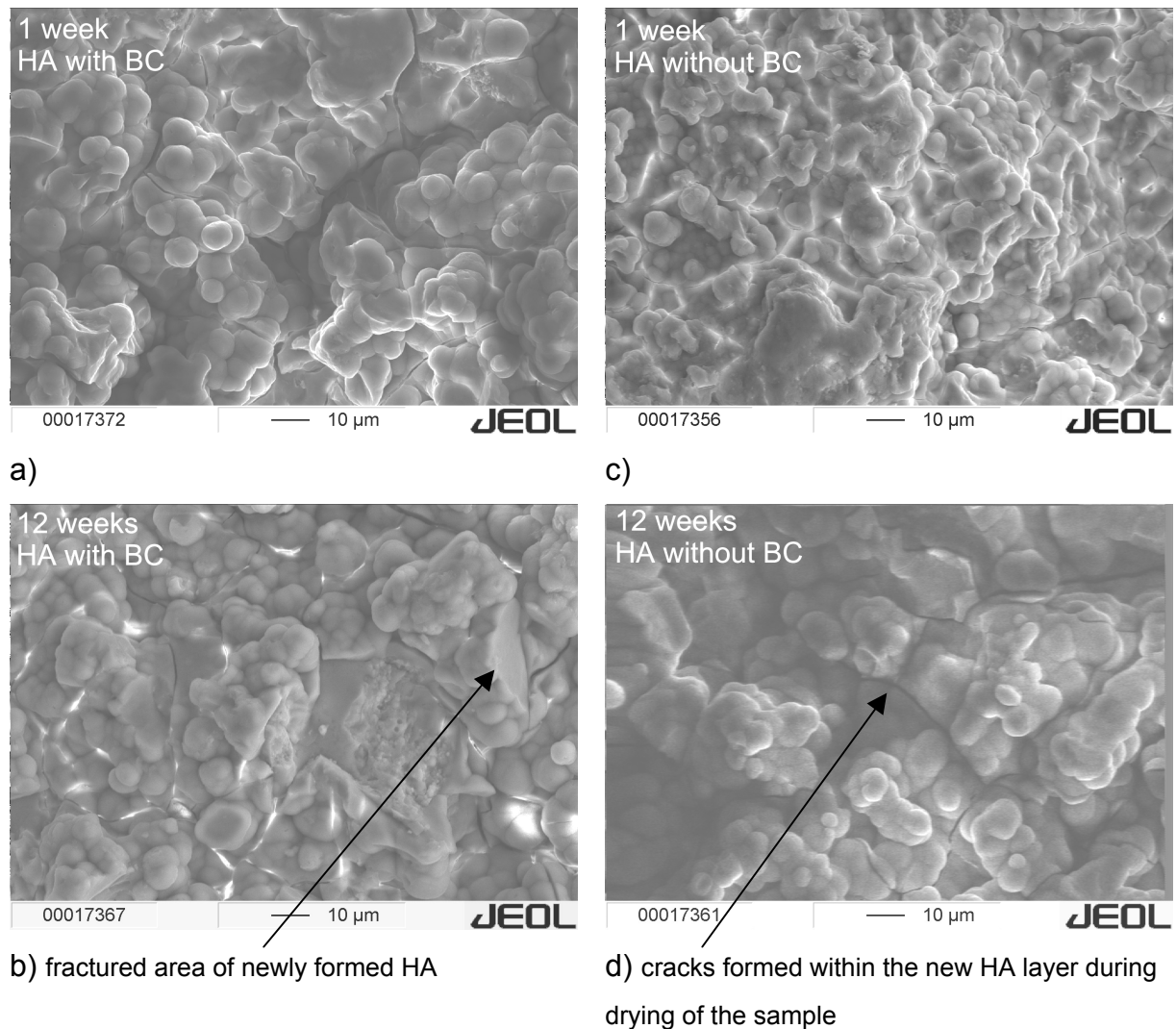


Figure 39: Surfaces of a) coating with a bond coat after immersion for 1 week; b) coating with a bond coat after immersion for 12 weeks; c) coating without a bond coat after immersion for 1 week; d) coating without a bond coat after immersion for 12 weeks.

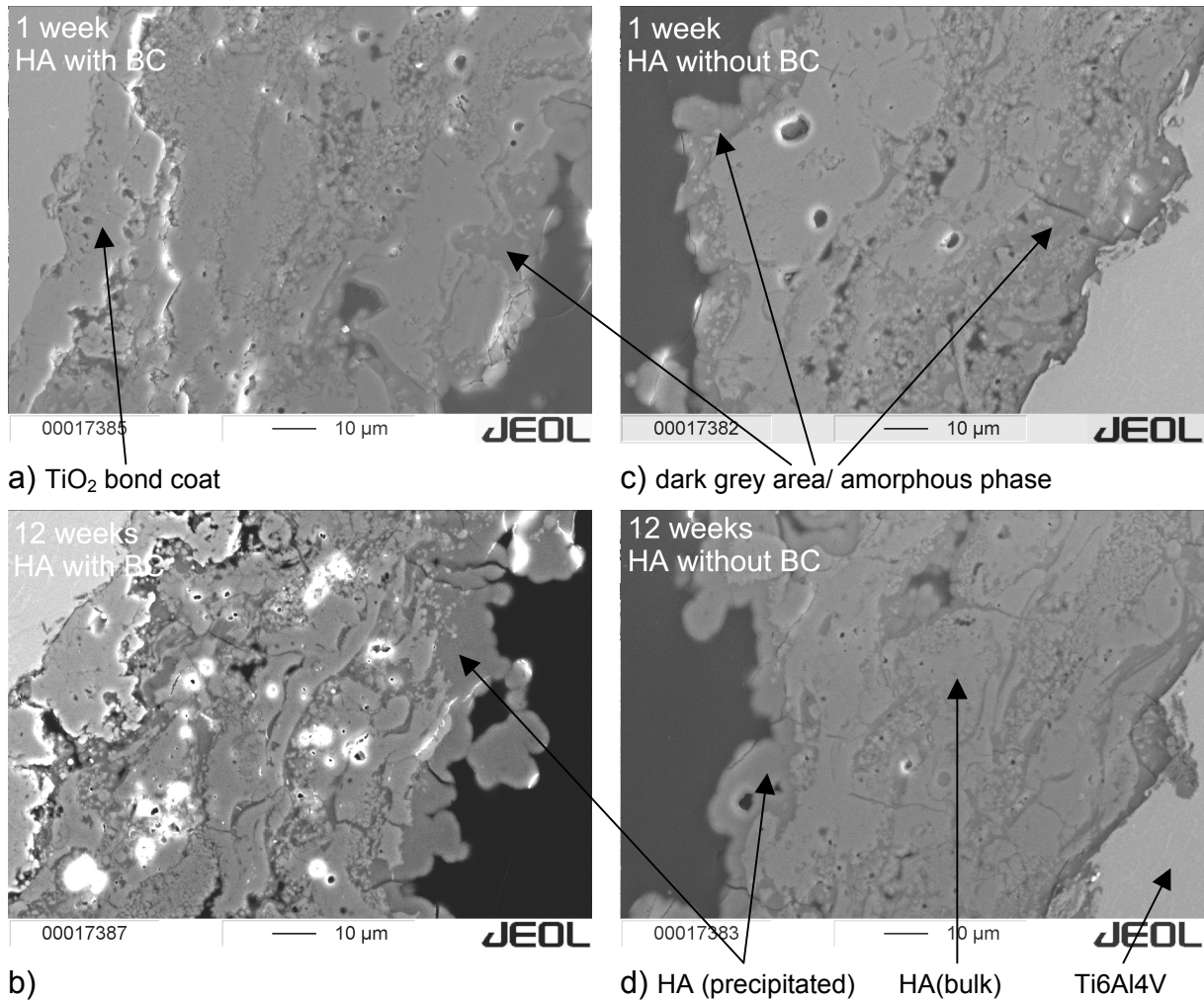


Figure 40: Cross-sections of a) coating with a bond coat after immersion for 1 week; b) coating with a bond coat after immersion for 12 weeks; c) coating without a bond coat after immersion for 1 week; d) coating without a bond coat after immersion for 12 weeks.

The kinetics of the growth of hydroxylapatite in aqueous solutions was thoroughly studied by several researchers, e.g. /123,112/. HA can incorporate a small percentage of magnesium into its structure, changing the structure and inhibiting further formation of HA. The presence of carbonate ions may also affect precipitation of HA, either by blocking phosphate nucleation sites, or by inducing calcium carbonate formation instead. A small quantity of Mg was detected in the newly formed layer on the coatings (s. EDX result below; Fig.41). Mg^{2+} - and HCO_3^{2-} ions available in the r-SBF inhibit the formation of apatite so that only extremely fine crystals of a few nanometer in size could precipitate /6/. That explains the rounded/ cauliflower-like shapes on the surface of incubated samples. Moreover, it should not be ignored that the buffer substance HEPES, an organic compound, may participate

in the crystal growth of HA. Adsorption of ligands on the active growth sites of the “mother” HA (coating) or phospho-organic complexes which forms on the active growth sites can inhibit the precipitation kinetics. Consequently, amorphous HA is prevented to transform into a more stable crystalline calcium phosphate. The crystallization inhibitors will prevent successive mineralization, and this effect provides time and space for proper attachment of biomolecules and cells after implantation /124/. In general, the newly formed calcium phosphate belongs to the am-CP/II type. A recent study /125/ also identified spontaneous precipitation of amorphous hydroxylapatite in solution containing calcium and phosphate ions.

Götze et al. /92/ spray-coated Ti6Al4V coupons with the same Mn-doped HA powder used in the present study. They incubated the coatings in a standard SBF (after Kokubo) which contains less HCO_3^{2-} and no HEPES buffer agent compared with the r-SBF /93/. After incubation for 4 weeks, fine HA crystals were formed on the coatings. However, distinct growth of the HA crystals was identified only after 8 weeks. Comparing this result with the results obtained in the present work leads to the conclusion that crystal growth of hydroxylapatite from simulated body fluid is very sensibly regulated by environmental conditions. Hydroxylapatite crystals existing in bone are of nanometer-size. From a mechanical point of view, small crystals precipitated on the coatings may re-enforce the strength of ingrown bone at the interface between the implant and the living bone. Hence, the coatings investigated in this study are considered favourable for medical applications.

Cracks on the surfaces of incubated coatings are attributed to the fact that the newly formed layer contains much water. During preparation of samples for the SEM investigation in vacuum this water is lost, leading to high shrinkage of the precipitated HA layer, and consequently crack formation.

It was also observed that in the incubated bioconductive coatings spongy zones disappeared gradually by in filling with new calcium phosphates. The longer the exposure period of coatings to the r-SBF, the denser the structure of coatings (Fig. 40) will be. Formerly small holes of some micrometers in the plasma-sprayed coatings are completely absent after immersion for 12 weeks. The rate of dissolution of the loose primary HA (un-molten) and other phases (TCP, TTCP or am-CP/I) and the rate of formation of am-CP/II are controlled by the diffusion of the reagents through the coatings.

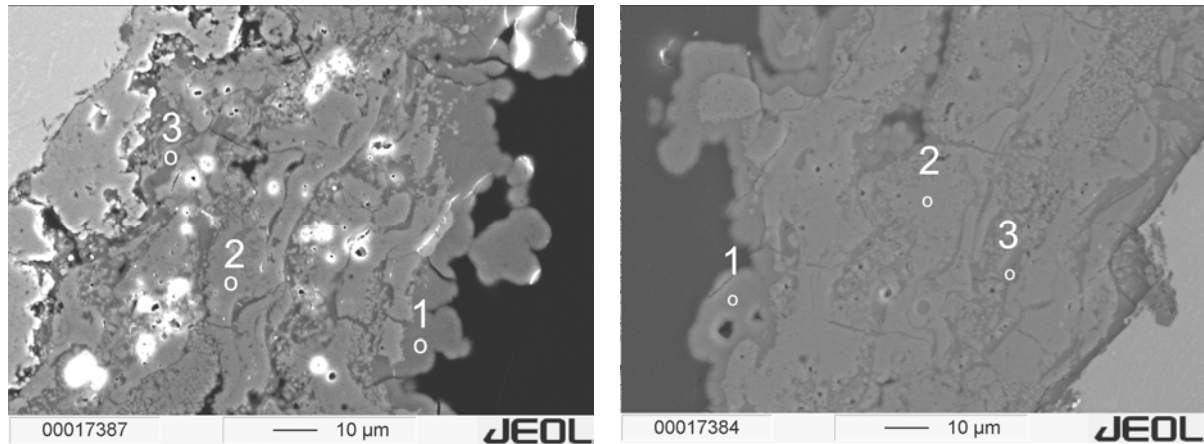
Some measurements by EDX were performed to determine the Ca/P ratio. The as-sprayed coating exhibits a molar Ca/P ratio of 1.73. Similar values were also found by other authors [126,127]. This high value does not contradict the results by Götze et al. (Ca/P= 1.61-1.85 in [92]), because the as-sprayed coatings in the present study contain some tetracalcium phosphate with a Ca/P ratio of 2.

The dense areas in the SEM images (Fig.38b/d, Fig.40a/b/c/d) indicate well molten and crystallized HA. The composition of this HA phase does hardly change during the immersion period in r-SFB, since its Ca/P ratio is nearly constant with 1.73. This points to very high chemical stability of the crystal phases. The newly formed calcium phosphates after 1 week are Ca-deficient HA (Ca/P = 1.59 – 1.61), with a low grade of crystallization (s. chapter 3.2). During a long-term *in-vitro* test for several weeks, the chemical composition of the precipitated CPs changes to higher Ca/P ratios because of a dissolution/ recrystallization process. The Ca/P ratio of the precipitated calcium phosphate phases approximates then 1.70-1.76, which is roughly equal to that of the as-sprayed coating. Obviously, the compounds of the r-SBF participate in the formation of the new CP within the porous bioceramic coating. The presence of Mg^{2+} is clear evidence for this (Fig.41). Such a phenomenon did not occur in the dense area of the coating. No diffusion of cations and anions (except OH^-) from the solution took place through the coating. Water exclusively enables the dissolution of soluble CPs (e.g. TCP, TTCP, am-CP/I) and occurrence of sequential precipitation of new HA in spongy zones within the coating.

It is interesting that applying a bond coat does not change the structural morphology of the HA coatings.

The dark grey areas in the SEM images (Fig.40 a, c) are assigned to am-CP/II, a precipitation product generated by dissolution of soluble components such as TCP, TTCP or am-CP/I. The amorphous phase is more often found at the interface substrate/ coating in the sample without a bond coat than in the sample with a bond coat. That is an indirect evidence for reduced formation of the amorphous phases during plasma spraying at the interface of the HA coating in the presence of a suitable bond coat. This result can be attributed to the lower thermal conductivity of TiO_2 compared to Ti6Al4V alloy (TiO_2 : 6.69 W/mK [128] and Ti6Al4V-alloys: 7.2 W/mK [129]). It is thought that the bond coat supports the formation of stable phases in coatings and promotes a good long-term bonding between the bioconductive coating

and the Ti6Al4V substrate. This observation clearly confirms the approach described by Heimann et al. /130/.



a) Coating with a TiO₂ bond coat

- Point 1: newly formed HA layer; Mg content amounts to 6.05 mol%
- Point 2: dense area; Mg content amounts to 0 mol%
- Point 3: newly formed HA within the coating; Mg content amounts to 1.54 mol%

b) Coating without bond coat

- Point 1: newly formed HA layer; Mg content amounts to 5.97 mol%
- Point 2: dense area; Mg content amounts to 0.22 mol%
- Point 3: newly formed HA within the coating; Mg content amounts to 1.49 mol%

Figure 41: Cross-sections of coatings immersed in r-SBF for 12 weeks with marked points analysed by EDX.

3.6 Probing the behaviour of the HA coating during the incubation process by cathodoluminescence

Cathodoluminescence (CL) is a very sensitive method to characterize the real structure of solids and hence is thought to contribute to clear up the resorption behaviour of the HA coatings. The luminescence properties of apatite are associated either with intrinsic electronic defects in the crystal lattice or with extrinsic defects caused by incorporation of trace elements in the crystal structure /108/.

Coatings of hydroxylapatite without doping with trace elements show only a visible blue CL colour /92/. Intrinsic energy emission occurring due to electronic lattice defects causes the emission in the blue and ultraviolet spectral range. However,

doping HA with manganese changes the CL colour to orange-red (Fig.42). Originally manganese is heterogeneously distributed in the HA spray powder (Fig.42a). Plasma spraying leads to a homogeneous luminescence colour in the coating (Fig.42b).

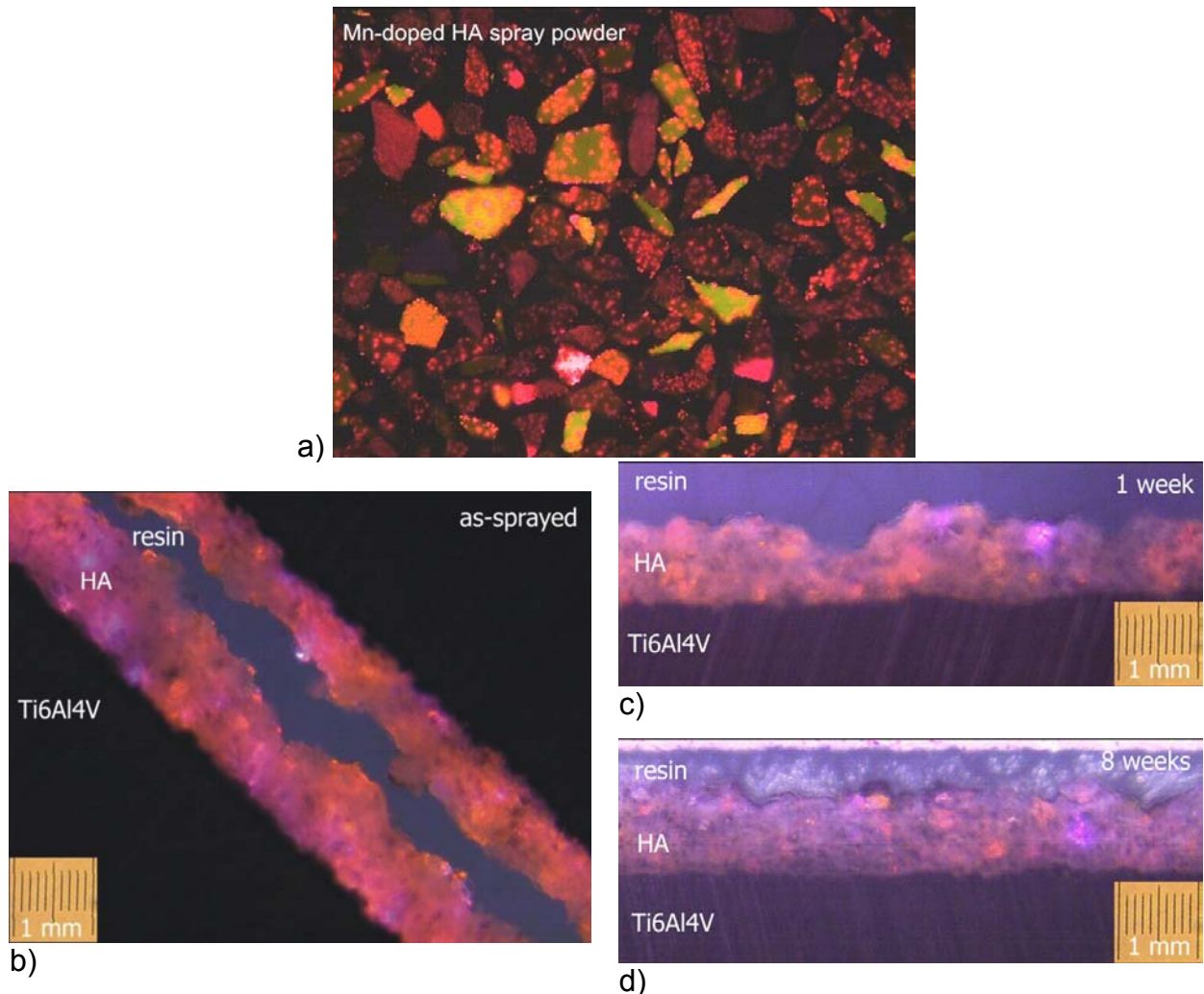


Figure 42: CL-micrographs of a) Mn-doped HA spray powder, b) as-sprayed coating /91/, c) coatings incubated in r-SBF for 1 week and d) coatings incubated in r-SBF for 8 weeks.

The CL investigation demonstrates altered luminescence behaviour of the HA coating during the incubation process. Dissolution of the thermal decomposition products of HA such as CaO, TCP, TTCP (and defect OHA) consecutively accompanies the release of the Mn^{2+} ions. This is responsible for a decline of the CL intensity. Different colours in the coating incubated in the r-SBF point to zones with different leaching behaviour within the plasma-sprayed coating. Orange-red luminescent areas in the incubated samples (for 1 or 8 weeks, Fig.42c, d) belong to

stable crystalline phase HA/ OHA. When Mn^{2+} is gradually released from the coating, the extrinsic emission effect (orange-red colour) is decreasing (extrinsic defects by impurity ions), while the intrinsic emission (blue colour) is becoming more visible (defects by vacancies or by distortions). The patches of blue CL colour in the coating incubated for 8 weeks (Fig.42d) substantiate again the existence of residual distorted calcium phosphates in the plasma-sprayed coatings even after a long-term *in-vitro* test. While the statements made above refer to only a qualitative description of the HA behaviour during the incubation process, quantification is principally possible by recording CL spectra of the dopant ions, e.g. Mn^{2+} /92/. This result harmonizes well with findings obtained by NMR, LRS and TG.

3.7 Characterization of as-sprayed coatings in cross-section

In chapter 3.4 it was attempted to find difference between the coating materials in the area near the surface and at the interface coating/ bond coat by thermogravimetry. In this chapter, Raman spectroscopy will be used to generate different responses of structural vibrations, by which any structural changes could be identified.

Figure 43 represents Raman-spectra recorded at different locations of cross-sections of coatings without or with a TiO_2 bond coat. It is evident that on approaching the interface, the intensity of vibrational bands decreases, and the line widths broaden concurrently. This means indirectly that the crystallinity of the material at the interface coating/ substrate is lower than that of the material near the surface. In particular, the behaviour becomes more distinct in the coating without a TiO_2 bond coat. This difference is attributed to thermal insulation of the HA by the bond coat that promotes the re-crystallization of molten HA splats. The thermal conductivities of Ti6Al4V-alloys and of TiO_2 are 7.2 W/mK /129/ and 6.69 W/mK /128/, respectively. Hence the LRS results coincide well with the SEM observations (chapter 3.5) and support also the conjecture that the bond coat results in structural changes of the HA coating towards a stoichiometric, well-crystallized material.

The increase of the crystallinity in the direction from the interface to the surface of the coating is a consequence of the coating microstructure. Since the thermal conductivity of HA (3 W/mK /131/) is much lower than that of Ti6Al4V (7.2 W/mK

/129/), HA splats recrystallize in later stages of the spray process more than at the beginning.

On the point of chemical stability, the area at the interface between the coating and the substrate would present a weak point compared to the bulk coating, since low-crystalline interface HA could be more easily degraded by aqueous solutions than the higher-crystalline surface/ bulk coating due to the certain open porosity of the coating. It is assumed that application of a bioinert TiO_2 bond coat essentially minimizes this problem.

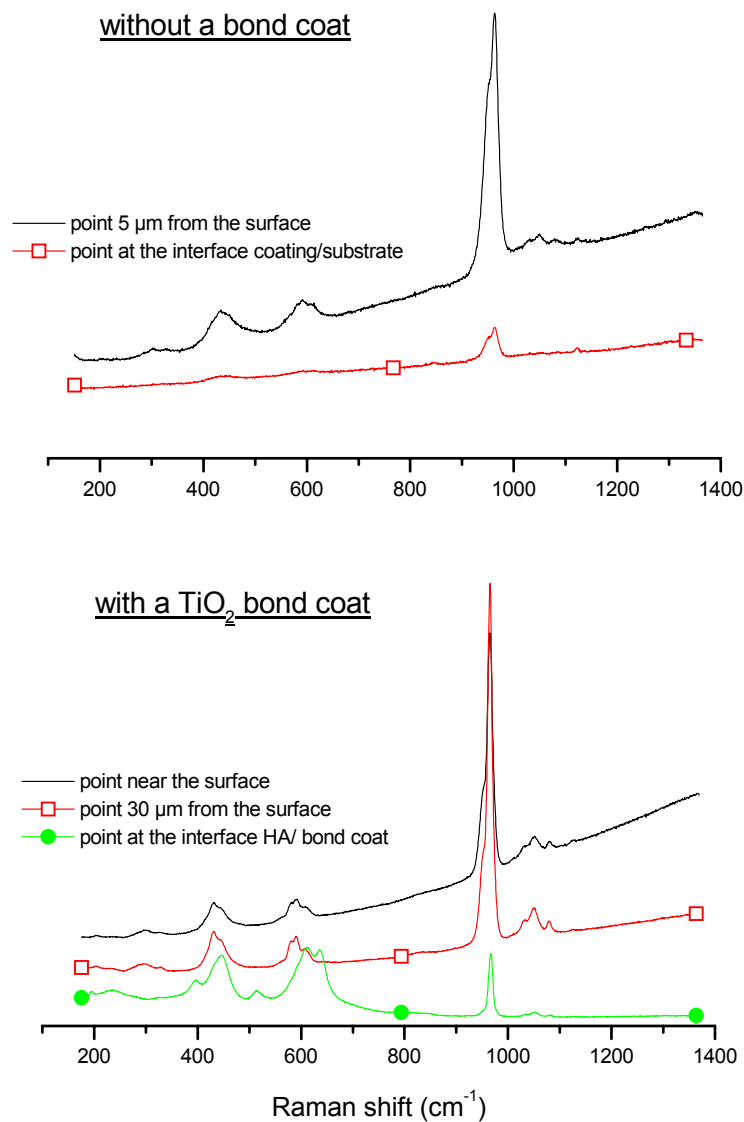


Figure 43: LR spectra at different points of the cross-sections of as-sprayed hydroxylapatite coatings without or with a TiO_2 bond coat.

3.8 Effect of thermal post-treatment on the microstructure of coatings

In chapter 3.4 it was highlighted that heating the plasma-sprayed HA coating give water vapour the opportunity to diffuse to the OH-vacancies of the hydroxylapatite lattice. Thermal treatment of sprayed samples at 630°C for 24 h in air is a useful tool to achieve fully crystalline coatings. The XRD experiments show sharp peaks without any sloping background (Fig.44). This indicates the presence of only crystalline hydroxylapatite-like phase in the post-tempered samples. Accordingly, the reaction partners (TCP and TTCP or OHA) required to form HA had to be very close to each other. Since this requires a very small distance between the reaction partners, the plasma spray-process fulfils almost ideally such suitable condition for the above reactions. Other authors /19/ heated hydroxylapatite up to 1500°C in air and subsequently cooled it down. They confirmed the decomposition process of HA and observed that TCP and TTCP reconstruct directly into OA at around 1350°C. When the temperature decreased to 1290°C, OHA was formed by a direct re-hydroxylation reaction of TTCP and TCP, and OA incorporated H₂O changing to oxyhydroxylapatite. At 1100°C, the remainder of TTCP and TCP converted into OHA. The results of the present work agree well with those obtained in Ref./19/.

It should be mentioned again that heat treatment at a lower temperature (e.g. 630°C) than the transformation temperature of Ti6Al4V (880°C, s. also chapter 3.4) can result in bioconductive coatings with higher crystallinity, associated with higher chemical stability. There is no decrease in adhesion strength between the coating and the substrate since the thermal stresses at the boundary coating/ substrate will be minimized.

Sharp peaks can be seen in the Laser-Raman spectra of the tempered samples, which are typically ascribed to HA with high crystallinity (Fig.45). The band at 3576 cm⁻¹ assigned to the vibrational stretching mode of OH in hydroxylapatite is well-defined in the LR- spectra. The simulated band is determined by a single peak and coincides well with the peak at 962 cm⁻¹, the symmetric stretching mode of the P-O bonds of well-crystallized, stoichiometric HA. Hence, the result of the LRS measurements points to hydroxylapatite with well-ordered PO₄³⁻-tetrahedra in the tempered samples.

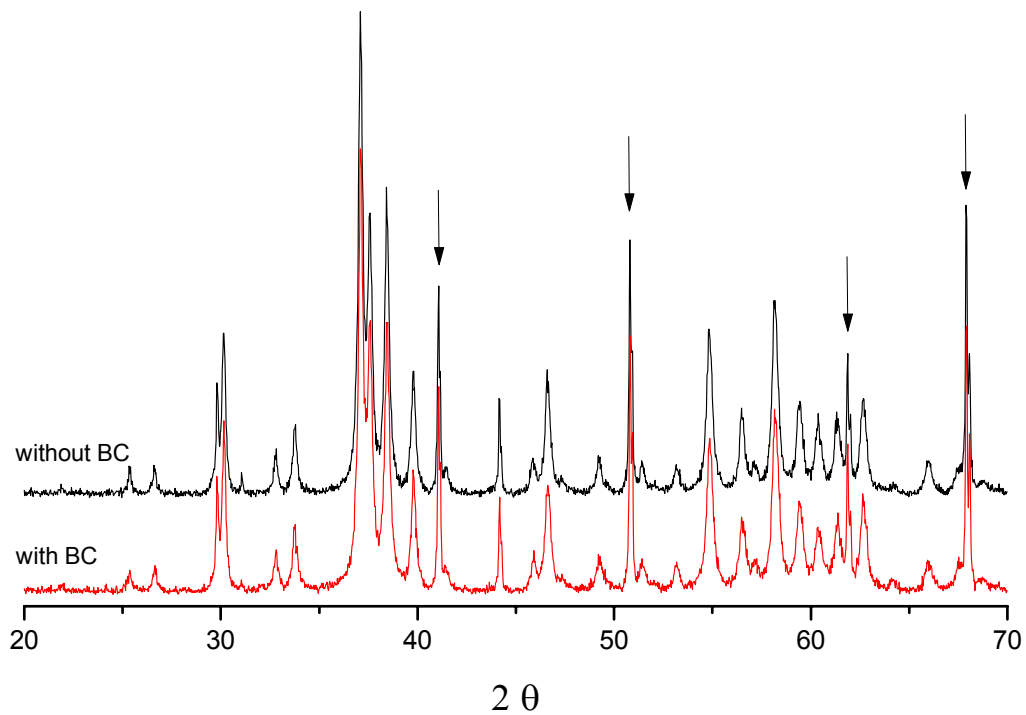


Figure 44: XRD pattern of the as-sprayed coatings after heat treatment at 630°C for 24 h. Arrows mark reflexes of corundum, which was added to the powder to determine the quantity of amorphous phases. No discernible amorphous phases are present in the thermally treated coatings.

This finding confirms again that the decomposition of hydroxylapatite during plasma spraying is reversible. Thermal post-treatment of an HA coating enhances not only the incorporation of OH^- ions, but also rearranges the electronic environment of PO_4^{3-} groups of (oxy)hydroxylapatite, indicated by disappearance of the bands B, D and C (typically for distorted PO_4^{3-}) in the ^{31}P -NMR spectrum [132].

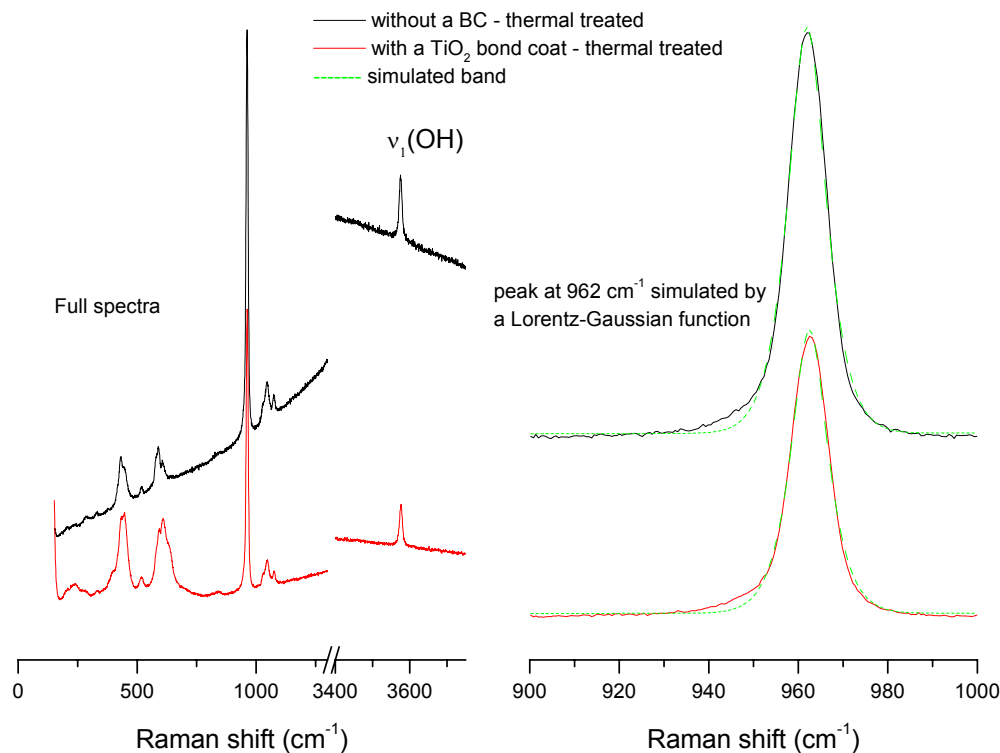


Figure 45: Raman spectra of HA coatings with (red) and without a TiO₂ bond coat (black) tempered at 630°C for 24 h in air atmosphere (left) and 962 cm⁻¹ band simulated by a Lorentzian-Gaussian function (right).

3.9 Influence of the bond coat thickness on the coating structure

In previous chapters it was shown that the microstructure of the plasma-sprayed coatings of hydroxylapatite will essentially change when a bond coat of titanium oxide is applied between the HA coating and the Ti6Al4V substrate. The thickness of such a bond coat was nearly 15 μm in these investigations (coupons of **set 1**). In the following the effect of the bond coat thickness on the coating structure will be further elaborated (coupons of **set 2**).

Microstructure of coatings

Figure 46 shows the ³¹P-MAS-NMR spectra of as-sprayed and incubated coatings with different thickness of the bond coat. Lorentzian deconvolution shows the four known band positions A, B, C, and D can clearly be seen. The existence of these

band positions appears to be independent of the applied bond coat thickness. This means the structural change of hydroxylapatite is mainly caused during heating within the plasma jet.

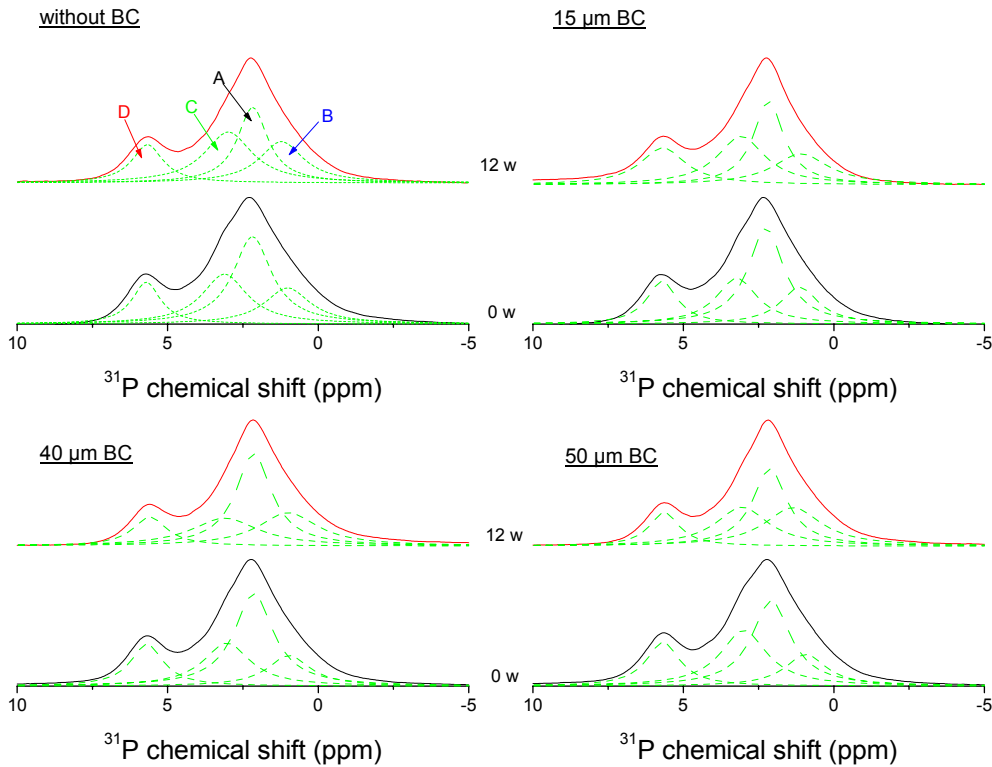


Figure 46: ^{31}P -MAS-NMR spectra of as-sprayed coatings (0 w) and of coatings incubated in r-SBF for 12 weeks (12 w) with different bond coat thickness.

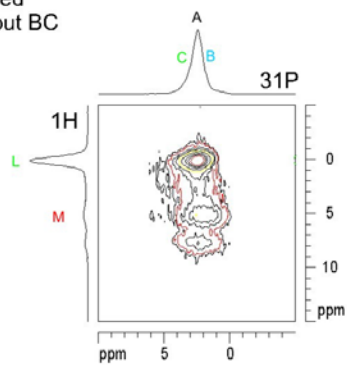
Figure 47 shows double quantum ^1H - ^{31}P -HETCOR NMR spectra of coatings without a bond coat and coatings with different bond coat thickness. These coatings are in the as-sprayed state (left) or incubated in r-SBF for 12 weeks (right). An elliptic form of the centres at approximately 2.3 ppm (^{31}P axis) – 0 ppm (^1H axis) and at 1.5 ppm (^{31}P axis) - 5 ppm (^1H axis) points to the presence of several correlation states of PO_4^{3-} and protons. The following signals are visible on the spectra: A-L, B-L, C-L, B-M, and C-M (top left). Their interpretation is given in chapter 3.1. The signal (at 7.5 ppm ^1H) of isolated OH^- group in the channel of sintered HA is found in the HETCOR spectra. This signal is absent when coatings produced from HA powder 1 (Mn doped powder) were investigated. With the same plasma spray parameter set, the finer hydroxylapatite powder 2 was more strongly heated than the hydroxapatite powder 1

during the spray process. That may leads to the existence of the ^1H position at 7.5 ppm. The NMR analysis characterizes the different behaviour of the hydroxylapatite powder 1 and powder 2 during the thermal spraying.

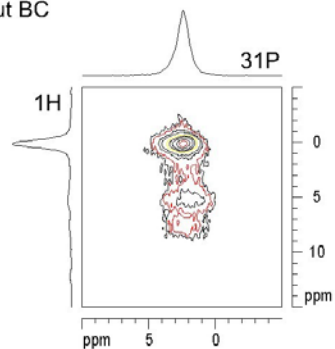
It can be observed that the HETCOR spectra do not distinguish among the variation of the bond coat thickness. The coatings incubated in r-SBF for 12 weeks retain hydroxylapatite with a distorted structure, whereas the elliptic form of the centres at 2.3 ppm (^{31}P axis) - 0 ppm (^1H axis) still dominates.

The relative intensities of all band positions were determined. They are presented in Fig.48. It is deduced from this result that the quantitative structural change of a hydroxylapatite coating is almost independent of the thickness of a TiO_2 bond coat up to 50 μm . After incubation in r-SBF for 12 weeks, there is a slight change of the relative intensity of the peaks A, C, B and D. The intensity of the peak A decreases. A dense structure of the HA coatings (s. below) hinders both the diffusion of OH^- ions from water into the OH channel in HA crystals and the dissolution-precipitation process of calcium phosphates within the bulk coating. This explains the existence of residual hydroxylapatite with a distorted structure in the coatings incubated for up to 12 weeks.

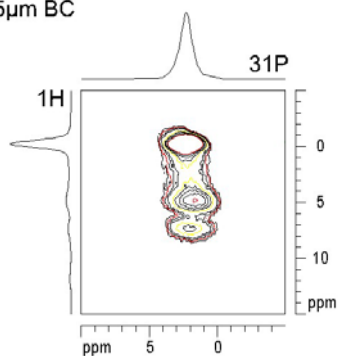
as-sprayed
HA without BC



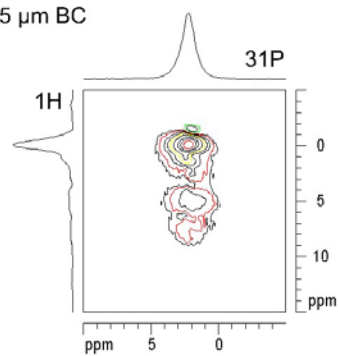
12 weeks
HA without BC



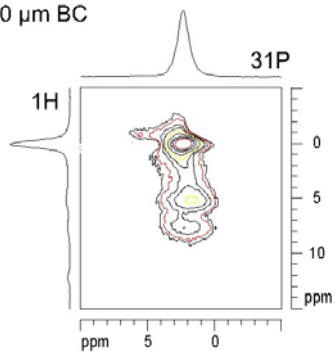
as-sprayed
HA with 15µm BC



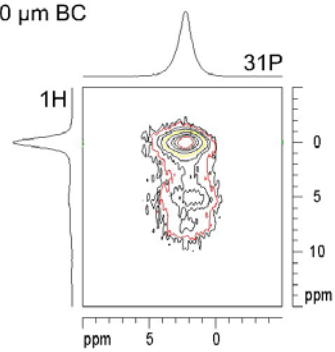
12 weeks
HA with 15 µm BC



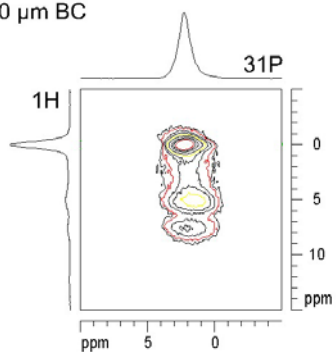
as-sprayed
HA with 40 µm BC



12 weeks
HA with 40 µm BC



as-sprayed
HA with 50 µm BC



12 weeks
HA with 50 µm BC

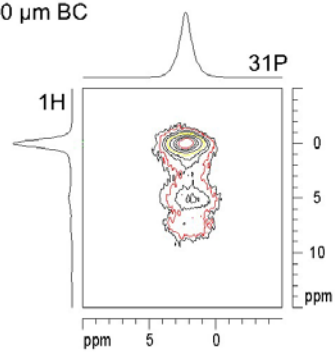


Figure 47: 2D ^1H - ^{31}P -HETCOR spectra of the coating without and with different TiO_2 bond coat thickness as-sprayed (left) and incubated in the r-SBF for 12 weeks (right).

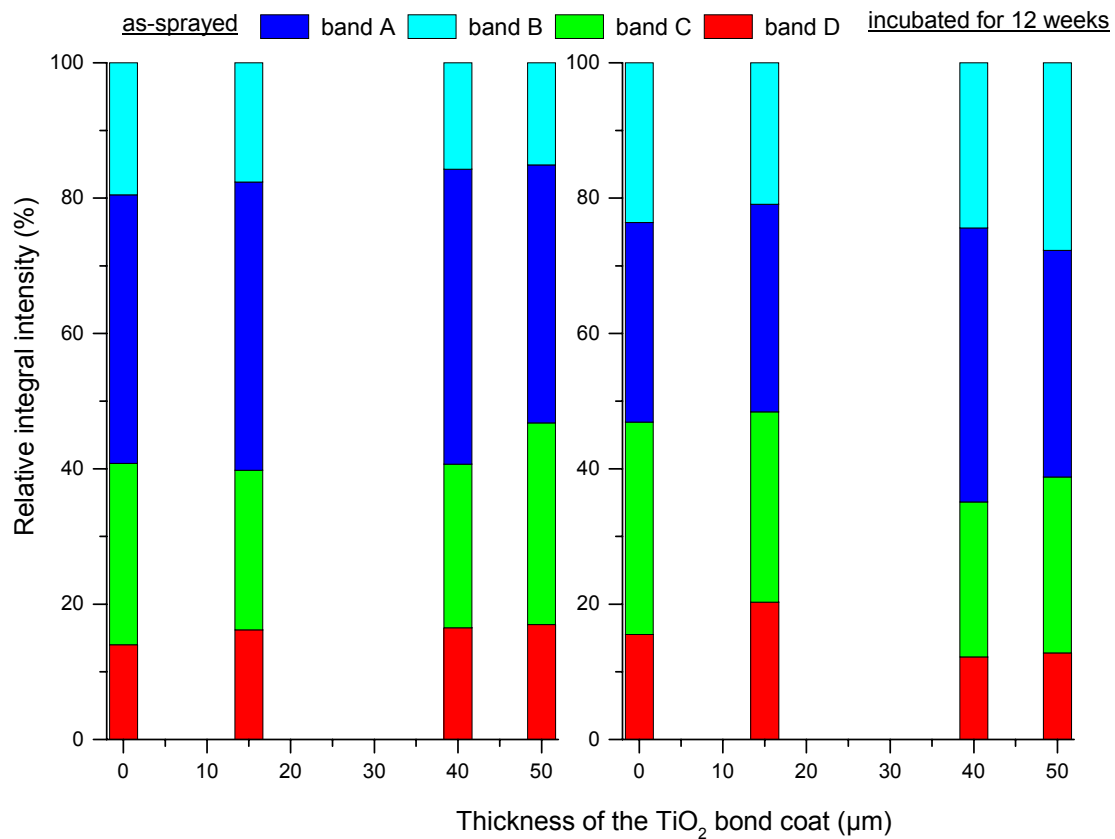


Figure 48: Relative integral intensity of the four band positions A, B, C and D of the as-sprayed HA coatings with different TiO₂ bond coat thickness (left panel) and incubated in r-SBF for 12 weeks (right panel).

Coating surfaces

The recorded Raman spectra of the coatings resulted in four frequencies ν_1 , ν_2 , ν_3 and ν_4 of PO₄³⁻-tetrahedra, which split in several peaks (Fig.49) and a weak frequency ν_1 of the OH⁻-group. All peaks in the spectra can be assigned to hydroxylapatite. Deconvoluting the peak at 962 cm⁻¹ by a Lorentzian-Gaussian function confirms the triple nature of the peak (see also Fig.25 for understanding). The peaks at 971 and 949 cm⁻¹ are associated with distorted PO₄³⁻-tetrahedra and with nano-crystalline HA, respectively (see also chapter 3.2). Not surprisingly, the bond coat thickness hardly affects the phase composition at the surface, which is presented as percentage of integral peak intensity (Fig.50). It leads to the finding that in the presence of bond coats with thickness within the range between 0- 50 μm, the

phase composition at the surface is only determined by the plasma spray parameters (e.g., powder characteristics, plasma energy, carrier gas, flow rate, powder feed rate, spray distance, etc.).

Incubation of the coatings causes a significant change of the phase composition (Fig. 50). The intensity of the peak at 962 cm^{-1} , typical of well-crystallized hydroxylapatite, decreases noticeably, while the peaks at 949 and 971 cm^{-1} increase in intensity. This is consistent with the fact that due to the low lateral resolution Raman spectra could be recorded only from the newly formed layer at the coating surface. This layer consists of very fine crystals with an apatitic structure (see also chapter 3.2 and SEM images below). The new layer formed biomimetically by dissolution of the coating and precipitation of hydroxylapatite from the r-SBF. Hence, the phase composition of the new layer is not influenced by the bond coat thickness.

The full width at half maximum height (FWHM) of the peak 962 cm^{-1} may be an indicator of the crystallinity of HA. It considerably decreases for all coatings after an incubation time of 12 weeks (Fig.51), indicating that the crystallinity of the coating surface increases when being incubated in r-SBF. As shown in Tab.5, the crystallinity of the HA surface layer increase in the presence of a bond coat with increasing incubation time beyond 4 weeks.

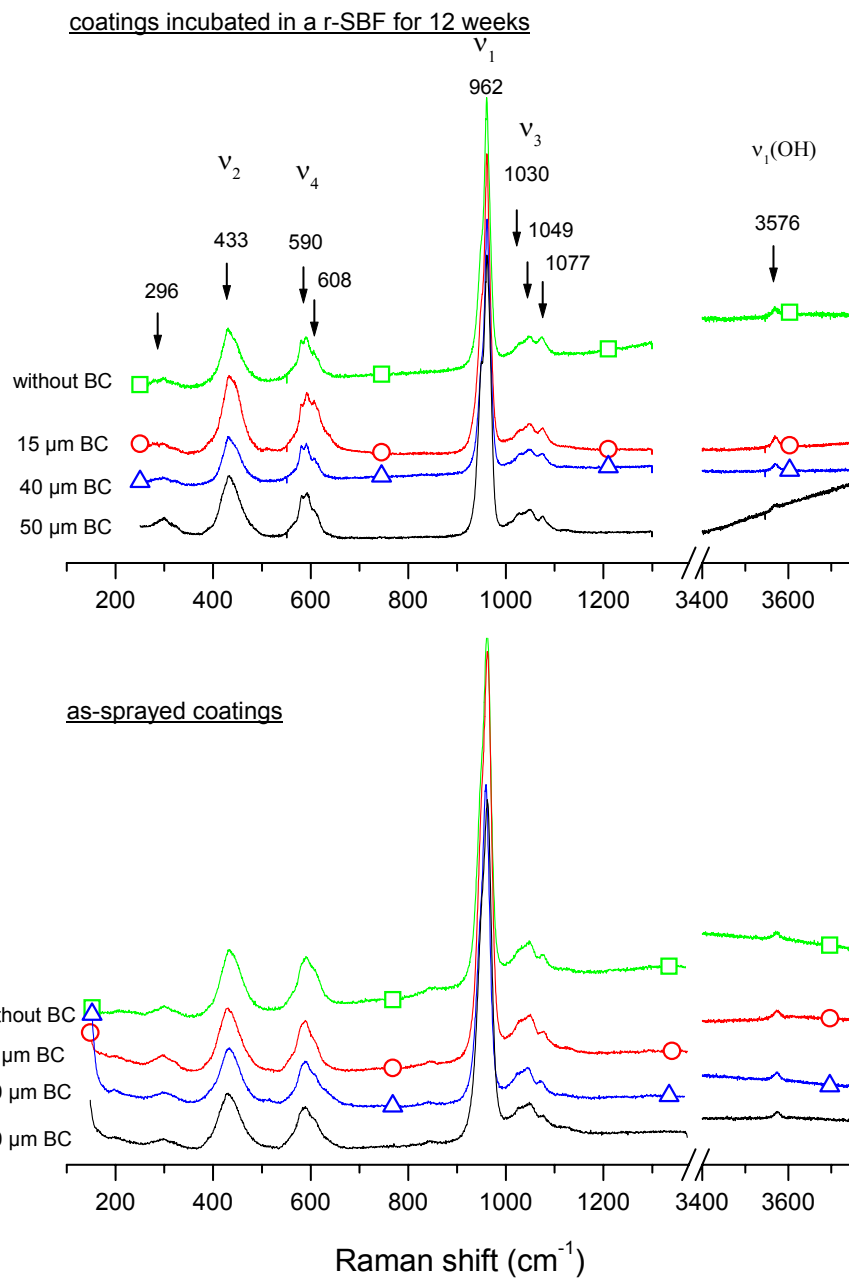


Figure 49: Raman spectra of the as-sprayed HA coatings without and with different bond coat thickness (bottom) and coatings incubated for 12 weeks in r-SBF (top).

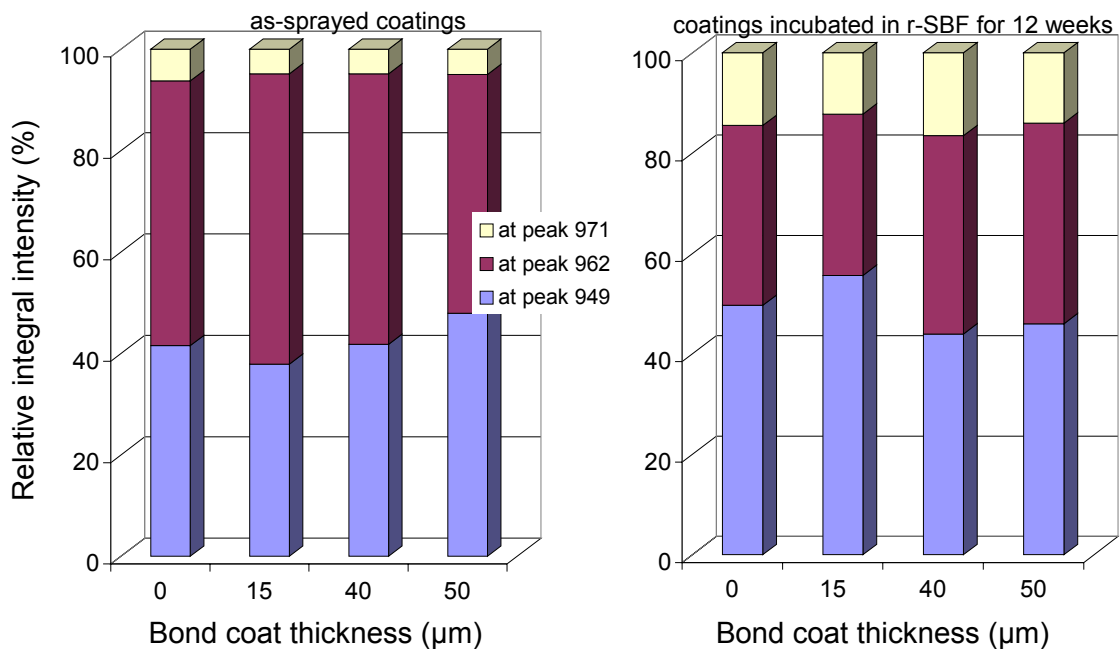


Figure 50: Relative integral intensity of the peaks at 949, 962 and 971 cm^{-1} in HA coatings with different bond coat thickness.

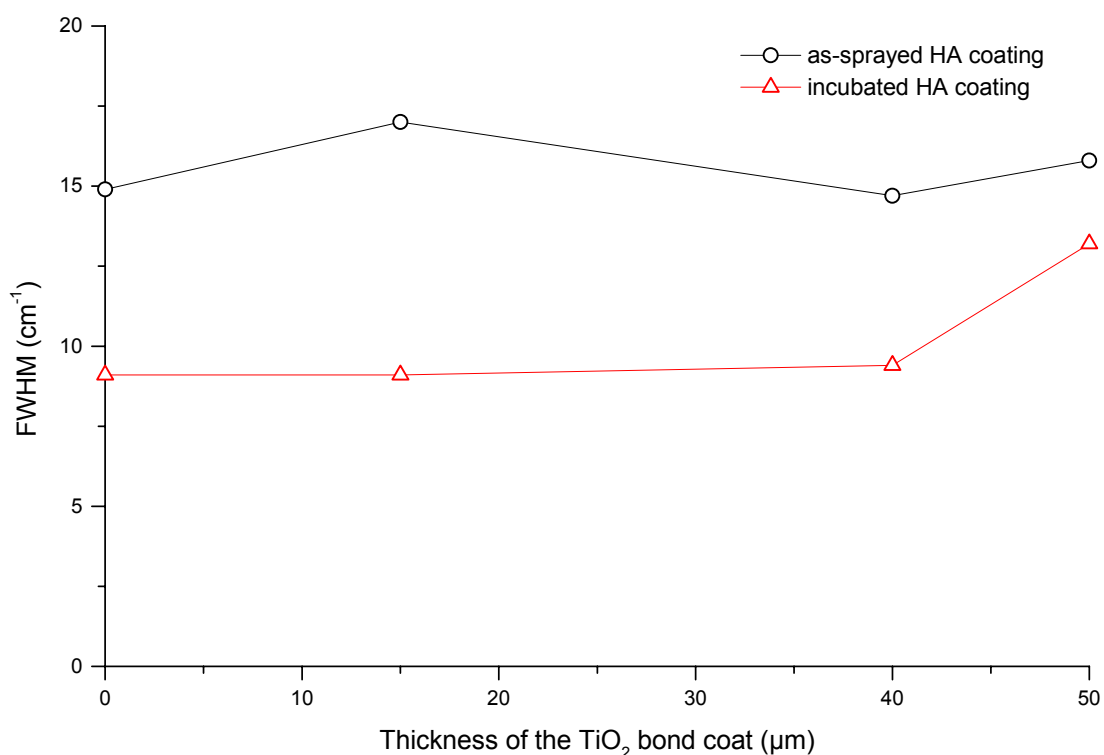


Figure 51: Influence of the bond coat thickness on the full width at half maximum height (FWHM) of peak 962 cm^{-1} of the HA coatings incubated in r-SBF for 12 weeks.

Phase analysis

A significant change of the amount of crystalline phases is achieved by application of a bond coat (Fig.52). The plasma-sprayed coating without a bond coat contains about 80 mass % hydroxylapatite (i.e. phases with a hydroxylapatite-like structure), β -tricalcium phosphate, tetracalcium phosphate (about 19 mass %) and CaO (ca. 1.1%) as crystalline phases. Bond coats of up to 50 μm suppress the formation of tricalcium phosphate, while the CaO amount also decreases (< 0.4 %). It is assumed that the bond coat can effectively hinder the thermal loss of molten spray particles by impacting on the substrate surface. As a consequence, tricalcium phosphate may react with tetracalcium phosphate to form oxyapatite according to $\text{Ca}_4(\text{PO}_4)_2\text{O} + 2\text{Ca}_3(\text{PO}_4)_2 = \text{Ca}_{10}(\text{PO}_4)_6\text{O}$. This phenomenon would be akin the thermal treatment plasma-sprayed coating for a very short time.

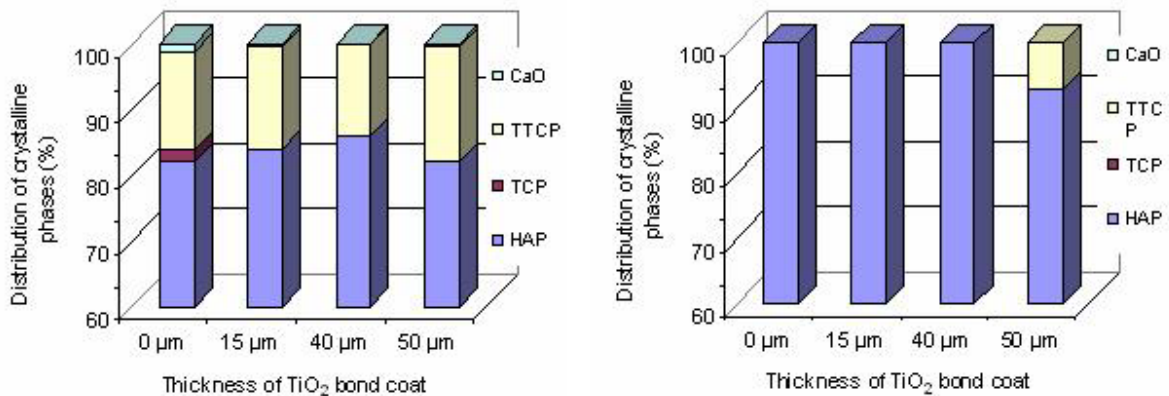


Figure 52: Distribution of the crystalline phases in the HA coatings with different TiO₂ bond coat thickness. Left: as-sprayed coatings; Right: coatings incubated for 12 weeks.

After incubating the as-sprayed HA coatings in r-SBF for 12 weeks, only hydroxylapatite was detected as crystalline phase by XRD in the coating without and with a bond coat of up to 40 μm , while the coating with a 50 μm bond coat still provides about 7 % TTC P and 93 % HA (Fig.52). An increase of HA in the crystalline phases is attributed to dissolving TCP, CaO and TTC P from the coatings as well as to precipitating new HA crystals from the revised simulated body fluid or by the reaction of TCP and TTC P during the incubation process.

The phase compositions of the as-sprayed coatings without or with a 15 μm TiO_2 bond coat in Fig.52 differ clearly from that presented in Fig.31. The difference is attributed to different HA powders used in the experiments. For the coatings in Fig.31 the powder 1 was used which was doped with Mn and contains 91.7 % hydroxylapatite and 8.3 % β -tricalcium phosphate. Fig.52 shows the data of the coatings with the powder 2, which consists of 100 % hydroxylapatite.

Morphology of coatings

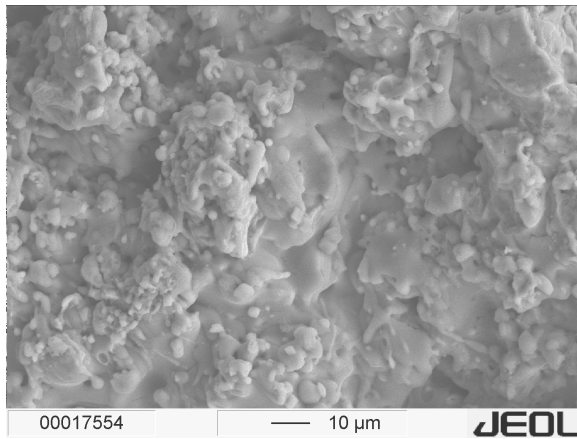
Applying plasma power of 32 kW led to fully molten HA particles. Well-molten splats can be seen on the surface of coatings (Fig.53a). Consequently, spongy zones do not exist within the as-sprayed coatings (Fig.53c). On the subject of bone ingrowth, this structure is disadvantageous in term of bone anchoring, because pores of a diameter of 50-100 μm within the coating are desirable for better bone integration /134/. These large pores are not present in the coatings shown in Fig.53.

Immersing the plasma-sprayed coatings in r-SBF for 12 weeks causes the surface to attain a “cauliflower” shape (Fig.53b). The cross section of the incubated coating shows an apparently dense layer of nano-crystalline HA (Fig.53d), which formed during incubation. Indeed, this new HA layer consists of very fine crystals and several nano-pores, which are filled with water and/ or organic compounds (s. also chapter 3.4). They make the precipitated layer to be unintentionally dense. The newly precipitated layer seems to bond firmly to the bulk HA coating. Structural changes of the HA bulk coating are not observed.

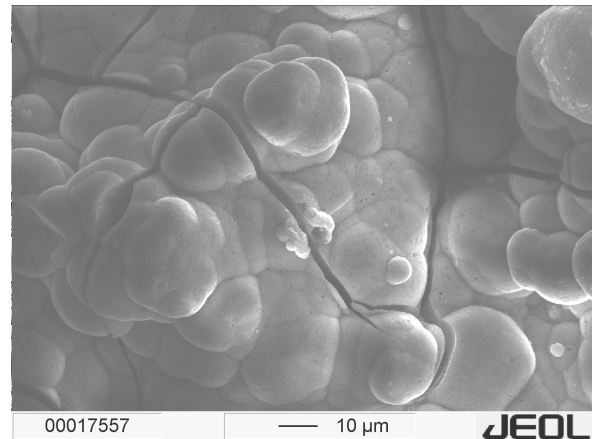
The influence of the bond coat thickness on the morphology of coatings appears to be insignificant for the powder used here (HA - powder 2).

as-sprayed

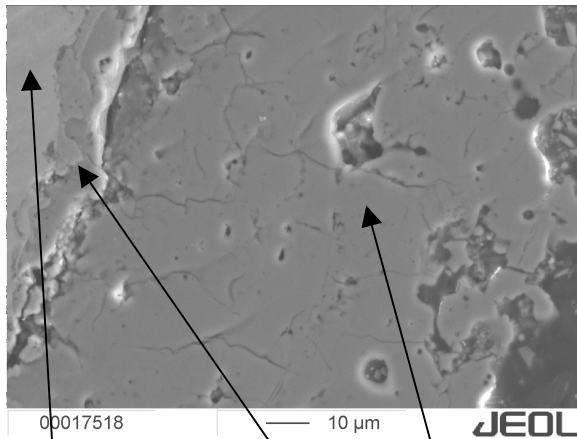
incubated in r-SBF for 12 weeks



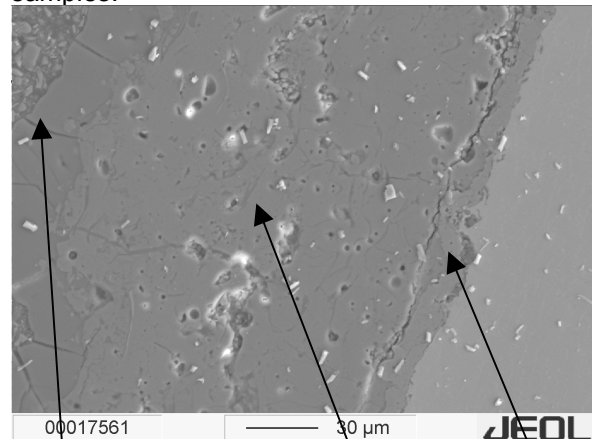
a) Representative surface for all coatings without a bond coat or with a bond coat, well melted spray particles



b) Representative surface for all coatings without a bond coat or with a bond coat, extremely fine HA crystals formed during incubation. Cracks were caused by drying of samples.



c) Ti6Al4V TiO₂ bond coat HA coating
Dense HA layer is also seen in the coating without a bond coat.
Representative cross section for as-sprayed coatings



d) newly precipitated HA layer bulk HA coating TiO₂ bond coat
Representative cross section for all coatings incubated for 12 weeks

Figure 53: SEM images of HA coatings.

3.10 Behaviour of coatings in different incubation solutions

In this chapter, the coatings were investigated by nuclear magnetic resonance (NMR) spectroscopy using a BRUKER Avance™ 400 MHz WB system, at the Department of Analytical Chemistry, TU Bergakademie Freiberg. The chemical shifts were referred to a solution of phosphoric acid (85%) for ³¹P and Q8M8 at 0.16 ppm (relative to

Tetramethylsilane) for ^1H NMR, respectively. ^{31}P spectra were measured with a rotation rate of 10 kHz, ^1H spectra with 15 kHz.

In these analyses only coupons of set 2 (HA powder 2) without a bond coat were investigated. The coatings were incubated in different solutions. These *in-vitro* experiments will show the influence of the simulated body solution on the coating composition and microstructure. The ion concentrations of the twofluids used are listed in Tab.7.

Table 7: Ion concentration of normal simulated body fluid (SBF), and revised simulated body fluid (r-SBF) according to /93/

Ions	SBF (mmol/l)	r-SBF (mmol/l)
Na^+	142.0	142.0
K^+	5.0	5.0
Mg^{2+}	1.5	1.5
Ca^{2+}	2.5	2.5
Cl^-	148.8	103
HCO_3^-	4.2	27
HPO_4^{2-}	1.0	1.0
SO_4^{2-}	0.5	0.5
others	TRIS (50 mmol/l)+ HCl (45 mmol/l)	HEPES (11.928 g/l)+NaOH 1M (15ml/l)

Figure 54 shows the ^{31}P -NMR spectra of the incubated HA coatings. In these coatings, incubated for 8 weeks, hydroxylapatite with a distorted structure is still present. The band positions A-B-C-D clearly indicate its presence. The new band position X belongs to a proton-free PO_4 environment, which was confirmed by a ^1H - ^{31}P -cross polarization (CP) spectrum. The position X does not appear in the ^1H - ^{31}P -CP spectrum (Fig.55). Furthermore, the ^{31}P -NMR spectrum of the as-sprayed HA coating shows only the four characteristic peaks A-D (s. also Fig.18). Hence, the position X may be assigned to a substance, which is presumably not contained in the

coating. It precipitated from the simulated body fluid and is physically absorbed on the coating. This substance has been not identified yet.

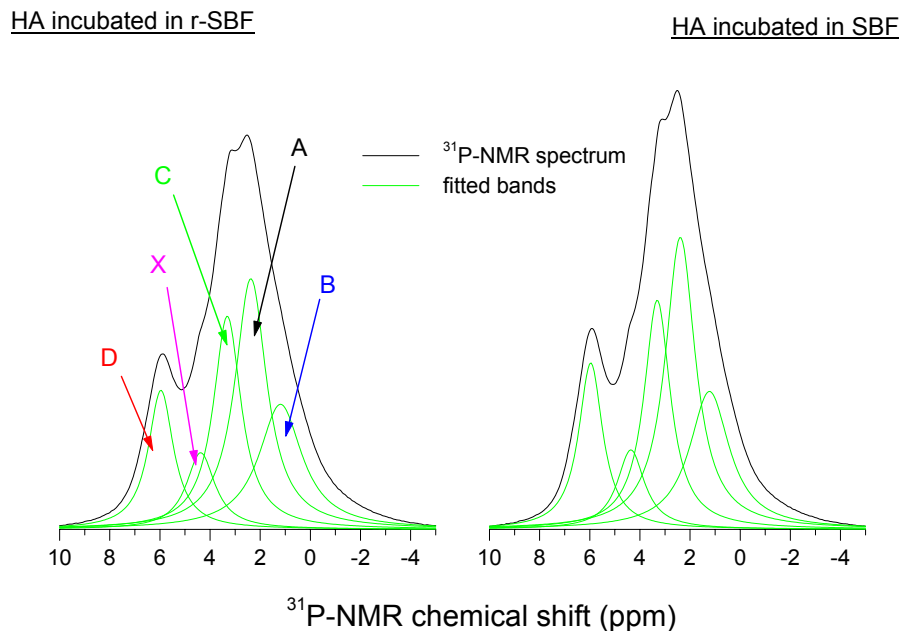


Figure 54: ^{31}P -MAS-NMR spectra of a HA coating incubated in different biological solutions for 8 weeks (left: incubated in r-SBF, right: incubated in SBF). Fitting by a Lorentzian function gives the band positions A at 2.3 ± 0.1 ppm, B at 1.5 ± 0.2 ppm, C at 3.0 ± 0.2 ppm, D at 5.6 ± 0.2 ppm, X at approximately 4.4 ppm.

The results of the NMR experiment reiterate again that hydroxylapatite with a distorted structure remains in the bioconductive coating even after long-term *in-vitro* tests, independent of the solutions used.

From tab.8 it is evident that the band positions of calcium phosphate are slightly broader in coatings incubated in r-SBF in comparison with coatings incubated in SBF. This finding may be attributed to the organic buffer compound HEPES and or to the higher content of the $\text{CO}_3^{2-}/\text{HCO}_3^-$ ions in the r-SBF. An increase of the carbonate content in the incubation solution does not change the integral intensities of the positions A-D (Tab.8).

The amount of the crystalline phases in the incubated coatings was determined. Concerning the phases, the coating incubated in r-SBF does not differ from the

coating incubated in SBF during the first incubation week (Fig.56). Differences between incubation in the r-SBF and in the SBF occur when the coating is incubated for 1 – 8 weeks. After being incubated for > 8 weeks, the amount of the crystalline phases in the coating is equal for the both solutions.

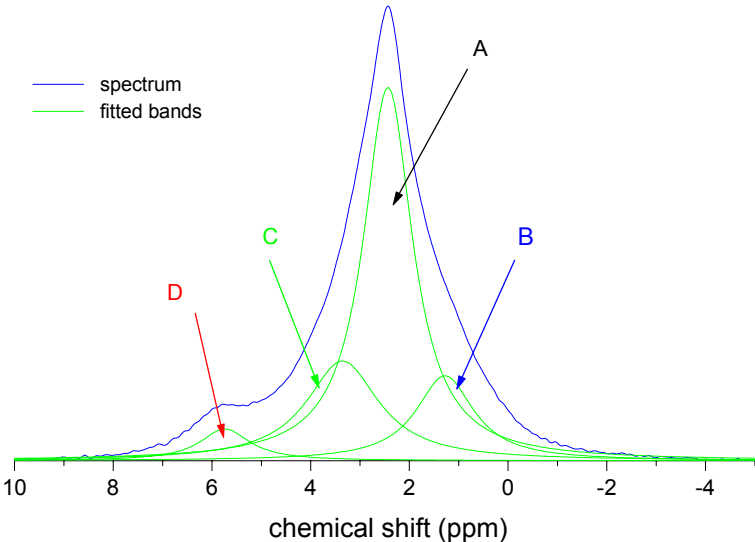


Figure 55: ^1H - ^{31}P - cross polarization (CP) spectrum of a coating incubated in SFB for 8 weeks. This spectrum is also representative for the coating incubated in r-SFB. Fitting by a Lorentzian function gives the band positions A at 2.3 ± 0.1 ppm, B at 1.5 ± 0.2 ppm, C at 3.0 ± 0.2 ppm, D at 5.6 ± 0.2 ppm.

Table 8: Characteristics of the band positions A-D, typical of plasma-sprayed hydroxylapatite. The relative integral intensities are referred to the sum of these positions (total of calcium phosphate). Values for the coating incubated in r-SBF and for the coating incubated in the SBF are shown.

Band positions	Coating incubated in r-SFB		Coating incubated in SBF	
	FWHM (ppm)	Relative integral intensity (%)	FWHM (ppm)	Relative integral intensity (%)
A	1,54	35	1,45	36
B	2,09	24	1,93	23
C	1,34	26	1,28	25
D	1,21	15	1,16	16

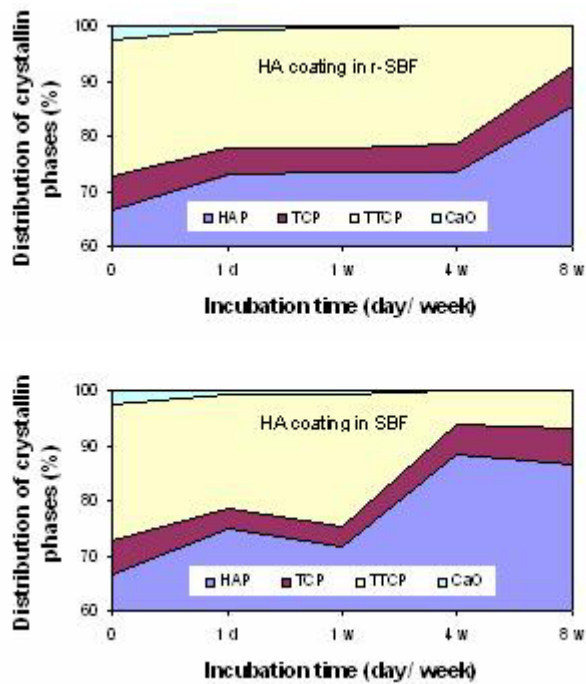


Figure 56: Amount of the crystalline phases of coatings incubated in different solutions for 8 weeks (top: r-SBF; bottom: SBF).

The surface morphology of the coatings incubated in the two solutions is shown in Fig.57. The r-SBF is favourable for the formation of new nano-crystals of calcium phosphate or amorphous calcium phosphate; type am-CP/II. As discussed in chapter 3.5, the higher concentration of carbonate ions and the presence of the organic substance HEPES in r-SBF are responsible for the microcrystals on the bioconductive coating. The formation of calcium phosphate on the plasma-sprayed hydroxylapatite coating appears to be more uniformly in r-SBF than in SBF (Fig.57).

The newly formed calcium phosphate layer is visible in the micrographs of cross-sections of coatings incubated in r-SBF (Fig.58a, b). Obviously, a calcium phosphate layer was formed on the coating incubated in the SBF too. But this layer was unfortunately damaged during the sample grinding/ polishing for SEM. So a gap is formed between the coating and the fixing resin (Fig.58c, d). The lamellar structure of the coating is a typical characteristic of the plasma spraying technology.

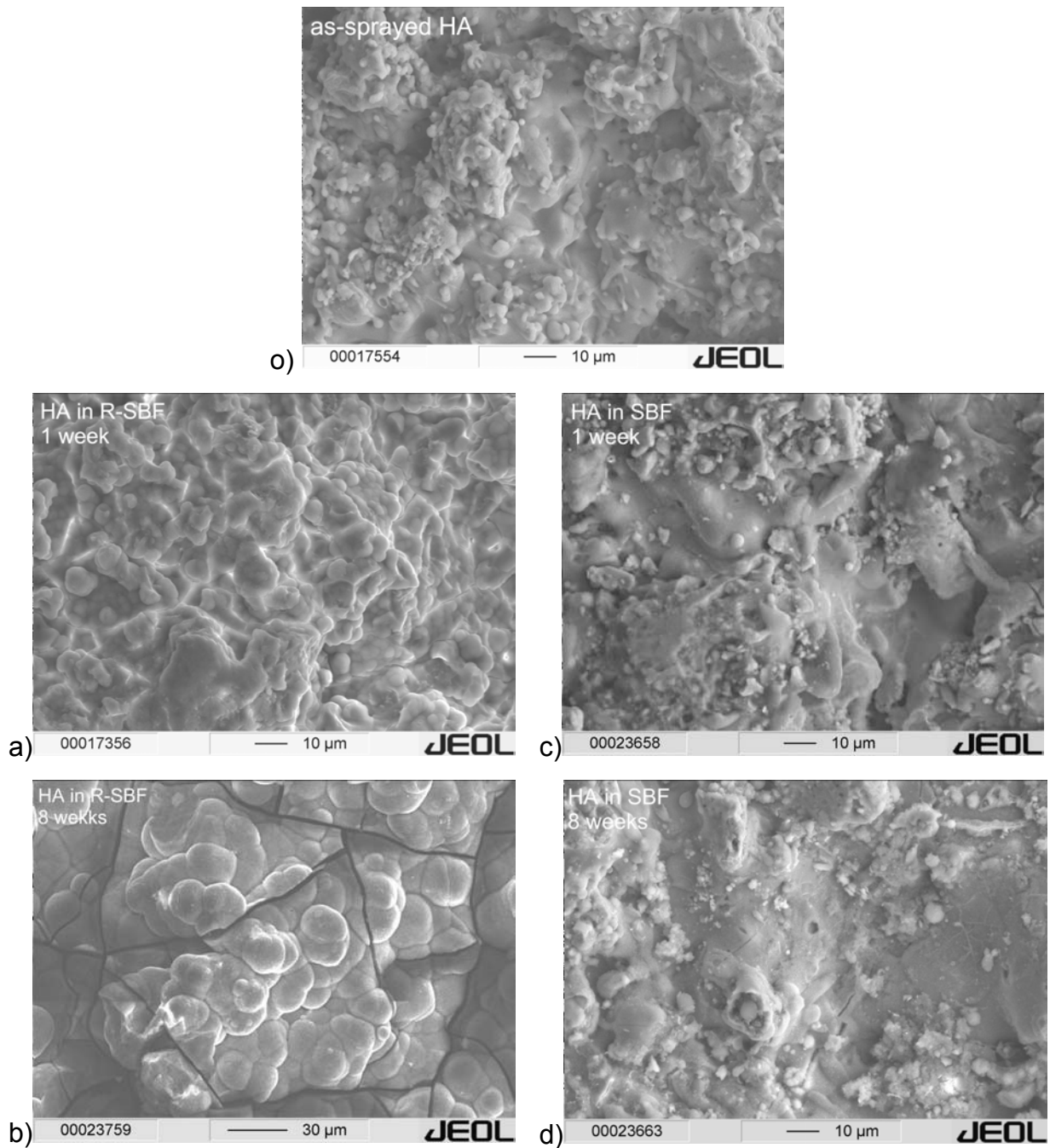


Figure 57: Micrographs of the surface: o) the as-sprayed HA coating, a+c) the coatings incubated in r-SFB or SFB for 1 week, b+d) the coatings incubated in r-SFB or SFB for 8 weeks, respectively. The formation of new calcium phosphate on the HA coating is relatively irregular when incubated in SBF. The r-SBF enables the balanced formation of the calcium phosphate layer. Cracks are caused during the sample preparation for SEM.

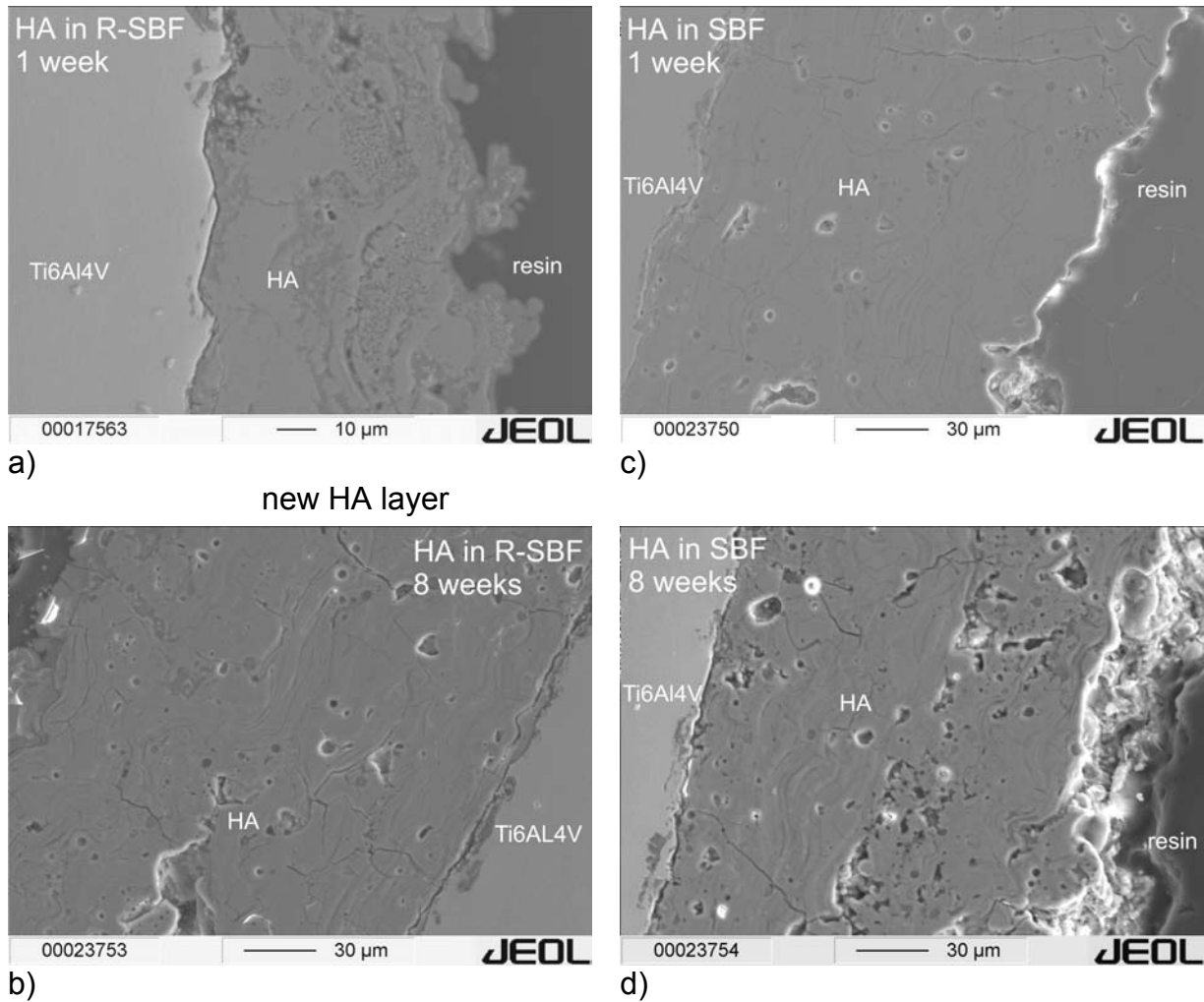


Figure 58: Micrographs of cross-section of HA coatings incubated in r-SBF or in SBF for 1 week and 8 weeks, respectively.

4 Conclusion

In the present study hydroxylapatite was plasma-sprayed onto Ti6Al4V substrates without a bond coat as well as with a TiO₂ bond coat. Several coupons were incubated in a “revised simulated body fluid” (r-SBF) and “simulated body fluid” (SBF) for different times up to 24 weeks. Several analytical methods, such as nuclear magnetic resonance spectroscopy (NMR), Laser Raman spectroscopy (LRS), thermogravimetry (TG), X-ray diffractometry (XRD), cathodoluminescence (CL), and scanning electron microscopy (SEM) were applied to investigate the thermal dehydroxylation and decomposition of hydroxylapatite, as well as the reconstruction of a distorted hydroxylapatite phase after incubation in SBF, and r-SBF. The main results are as follows:

- Plasma spraying essentially changes the structure of hydroxylapatite towards partially dehydroxylized hydroxylapatite, β -tricalcium phosphate, tetracalcium phosphate, CaO and amorphous phase and causes formation of fine crystals.
- Different local environments of protons were considered by NMR. The ^1H NMR spectra represent the 3 characteristic bands of the plasma-sprayed HA coating: the well-known proton band position (L) of the crystalline stoichiometric hydroxylapatite, the isotropic shift band (L^*) of protons in distorted hydroxylapatite short-range structure and the band position (M) of isolated pairs of strongly coupled protons in the channel structure. In the ^{31}P NMR spectra of the HA coating three further bands (B, C, and D) are found beside the band A typical of the stoichiometric hydroxylapatite. These bands B, C and D are caused by distorted HA structure. A long-term incubation in a protein-free simulated body fluid for up to 24 weeks still show states with distorted PO_4^{3-} / undistorted OH^- environment.
- The OH^- diffuses from simulated body fluid into the coating during incubation and the distorted crystal structures gradually rearrange. This process is more rapidly in the coating with a bond coat. However, after a very long-term *in-vitro* test, the hydroxylapatite coatings still show certain amounts of hydroxylapatite with distorted structure. The dense structure of the coatings hinders the OH^- diffusion through the bioceramic coatings. This leads to retention of distorted oxyhydroxylapatite after long-term incubation.
- Oxyhydroxylapatite is considered partially dehydroxylated hydroxylapatite with a distorted crystal structure. The OH vacancies in this structure can be proved by the additional bands in the NMR spectra. Therefore, the NMR is able to distinguish between HA and OHA.
- Broadening of LRS- peak at 962 cm^{-1} and the appearance of shoulder peaks at 949 and 971 cm^{-1} point to the formation of OH^- -deficient hydroxylapatite with high crystallinity (e.g. in thermal treated powders

HAP900 and HAP1000) and quasi-amorphous calcium phosphates (nano-crystalline HA precipitating in an incubation process). The intensity ratio of the 962 cm^{-1} peak to sum of peaks 949 and 971 cm^{-1} can be used to estimate the ordering degree of the HA crystal structure. It is evident that a bond coat reduces noticeably the distortion of hydroxylapatite coating during plasma spraying.

- Rapid quenching of HA spray particles caused by impact onto the substrate surface generates thermal non-equilibrium states. This means that several incompatible mineral phases coexist within the coating (see p. 52). During incubation in simulated body fluid the transformation front of decomposition products of HA, generated by plasma spraying, moves from the coating surface towards the substrate interface. This progress is mainly regulated by the diffusion rate of OH^- ions. Thermogravimetry is a useful tool to quantify the amount of the OH vacancies, which were re-occupied.
- Layers near the interface between the substrate and the coating contain more amorphous phases compared to layers near the coating surface. With a suitable bond coat, the amorphous phase at the interface between coating and substrate is reduced. It is also observed that the crystallinity of coating increases in the direction from the interface to the surface of the coating
- Incubation of the plasma sprayed coatings in a simulated body fluid generates of fine crystals of secondary hydroxylapatite at the coating surface. This new layer consists of “bone-like” apatite crystals. It supports essentially the integration of HA coated implant with the surrounding tissue. A bond coat of $\text{Ti}_n\text{O}_{2n-1}$ advantageously influences the formation of a new bioconductive layer on the coating. The new HA crystals form more easily on the coating with a bond coat than on the coating without bond coat.
- As shown by EDX analysis, most ions present (e.g., SO_4^{2-} , Na^+ , K^+) in the simulated body fluid do not participate in the transformation

process. Mg^{2+} is found in the area of the newly formed calcium phosphate.

- Cathodoluminescence is able to make the distorted structure of hydroxylapatite coatings visible. Blue is the intrinsic colour attributed to defects in crystals and is emitted in the coating incubated for 8 weeks. That substantiates the existence of residual distorted calcium phosphates.
- LRS analysis of cross sections of coatings reveals oxyhydroxylapatite with different distortion degrees. Furthermore, this investigation highlights again that application of a bioinert Ti_2O_{2n-1} bond coat forces the formation of well-crystallized material at the interface between the substrate and the HA coating.
- Thermal post-treatment of plasma-sprayed hydroxylapatite coating results in coatings with high crystallinity, whereby the defect apatite structure rearranges to a well-ordered structure. The optimal parameters (maximum temperature applied, heating rate) for the thermal post-treatment are dependent on the thermal history of the hydroxylapatite coatings. These parameters may be deduced from the TG results.
- Varying the thickness of bond coat does not appreciably influence the decomposition and structure change of HA. A bond coat less than 40 μm thick should be preferred.

5 Outlook and future work

- Oxyhydroxylapatite exists in plasma-sprayed hydroxylapatite coating even after long-term incubation in r-SBF. Concerning the ordering of PO_4^{3-} groups, this oxyhydroxylapatite has several distorted states. Its *in-vitro/ in-vivo* stability appears to depend on the OH content and the degree of lattice distortion. The dissolution kinetics of different types of oxyhydroxylapatite should be understood. Thus, the set of plasma

parameter should be optimized for tailoring bioconductive coatings with desirable bone integration properties.

- The consequence of the above step is the need for preparation of dense sintered oxyhydroxylapatite powders with different OH contents. These powders will be plasma sprayed. Dense sintering may reduce the OH loss during plasma spray process, whereas the structure of oxyhydroxylapatite will be retained. Fast-firing by microwave heating is one suitable technique for producing dense HA spray particles with minimum OH loss. However, for better bone ingrowth into the HA coating, an optimum macroporosity should be generated by adjusting the plasma spray parameters.
- The existence of distorted hydroxylapatite after incubation in a SFB is regulated by the exchange of ions between the coatings and the surrounding environment. Therefore, the effect of the OH⁻ permeability of coating on the transformation of distorted hydroxylapatite should be studied in the future. The higher the OH⁻ permeability, the faster this transformation.
- In further investigations a bond coat should be applied because of its favourable influence on the formation of new mineral phases on the implant surface. The thickness of such the bond coat is ideally 10 – 15 μm. Thinner bond coats are impossible due to the limitations of the plasma spray process. Thicker bond coats do not improve the chemical stability of the coatings.
- As discussed in chapter 3, the OH⁻ diffusion determines decisively the reconstruction kinetics of oxyhydroxylapatite and of the reaction TCP+TTCP+OH⁻ within the coating. An NMR study of the cross section of the coating will give some detailed information about the movement of the conversion front from the coating surface towards the boundary.
- The reconstruction time of oxyhydroxylapatite within the plasma-sprayed coating could possibly be substantially reduced, when the diffusion of the OH⁻ groups is enhanced in an electric field. The influence of electric fields on the diffusion kinetics of OH⁻ ions should be studied. One can postulate that an electric field with the metallic implant as a positive electrode

facilitates the movement of OH⁻ ions into the coating. Therefore, the reconstruction process of distorted HA towards to well-crystalline HA would be shortened if a plasma-sprayed HA coating was incubated in a SBF and an electric field was applied. This approach can be used to post-treat a HA coating to reach a well-ordered hydroxylapatite structure.

- NMR experiments on plasma-sprayed HA coatings treated with deuterated water will help to understand the re-occupation process of OH vacancies in the structural channel. Such experiments can show how each distorted environment changes during incubation in a simulated body fluid.

6 Acknowledgements

First of all, I would like to thank Professor Dr. Robert B. Heimann for giving me the opportunity to study for my PhD at TU Bergakademie Freiberg by joining his research group. At the same time, I am thankful for his proper guidance, advice and the time he spent on my work.

Special thanks go to Dr. Peter Hartmann (formerly at the Department of Optics and Quantum Electronics, Friedrich Schiller University of Jena), who kindly spent much time to measure the NMR spectra, the main part of my thesis.

Thanks are due to Mrs. Dipl.-Chem Margitta Hengst (Department of Mineralogy, Freiberg) for plasma spraying, Prof. Dr. Gert Irmer (Department of Theoretical Physics, Freiberg) for laser Raman analyses, and Dr. Erica Brendler (Department of Analytical Chemistry, Freiberg) for additional NMR analyses.

I owe also thanks to Dr. Reinhard Kleeberg (XRD analyses), Dr. Ulf Kempe (SEM and EDX), and Dr. Jens Götze (Cathodoluminescence), all three at Department of Mineralogy, Freiberg.

Many thanks go to Professor Dr. Berthold Thomas (Department of Analytical Chemistry, Freiberg) and Dr. Georg Berger (Federal Institute of Materials and Testing (BAM), Berlin) for co-refereeing my thesis.

Thank to everyone who helped me during the time I studied for my PhD in Freiberg.

And finally, thank to my parent and my husband for their support and encouragement, without which I could never have completed my PhD.

7 References

- /1/ G.Heimke
“Bone replacements: Implant materials and the modes of implant fixation“
Adv. Mater 10(1989); 345-348
- /2/ D.F.Williams
Materials science and technology. Volume 14: Medical and dental materials”
Wiley Europe, 1992
- /3/ G.Heimke
Biomaterials Highlights IV
The “State of the Art”
Adv. Mater 2(1990), 45-49
- /4/ G.Heimke
“Bioconductive ceramics“
Adv. Mater 3(1991); 320-322
- /5/ L.L.Hench
“Bioceramics: from concept to clinic”
Am.Cer.Soc.Bull. April 1993; 93-98
- /6/ J.C.Elliott
“Structure and chemistry of the apatites and other calcium orthophosphates”
Elsevier, Amsterdam – London – NewYork – Tokyo, 1994
- /7/ B.M.Tracy, R.H.Doremus
“Direct electron microscopy studies of the bone-hydroxylapatite interface “
J.Biomed.Mater.Res 18(1984); 719-726
- /8/ S.N.Bhaskar, J.M.Brady, L.Getter, M.F.Grower and T.Driskell
“Biodegradable ceramic implant in bone“
Oral.Surg 32(1971); 336-346
- /9/ P.Roux, D.Louër, G.Bonel
“Sur une nouvelle forme cristalline de phosphate tricalcique”
Compt.Rend.Acad.Sci (Paris) Ser. C 286 (1978); 549-551
- /10/ M.Mathew, S.Takagi
“Structures of biological minerals in dental research”
J.Res.Natl.Inst.Stand.Technol 106(2001); 1035-1044
- /11/ U.Posset, E.Löcklin, R.Thull, W.Kiefer
“Vibration spectroscopic study of tetracalcium phosphate in pure polycrystalline form and as a constituent of a self-setting bone cement”
J.Biomed.Mater.Res 40(1998); 640-645

- /12/ D.F. Williams
"Biocompatibility: an overview"
Concise Encyclopedia of Medical and Dental Materials
Pergamon Press, Oxford, New York, 1990; p.51
- /13/ B.S.H.Royce
"The effect of structure and ionic transport properties of calcium apatite"
J.Phys.Suppl, 34(1973), (C9) 327-332
- /14/ T.Takahashi, S.Tanase, O.Yamamoto
"Electrical conductivity of some hydroxyapatites"
Electrochem. Acta 23(1978); 369-373
- /15/ J.C.Elliott, P.E.Mackie, R.A.Young
"Monoclinic hydroxylapatite"
Science 180(1973); 1055-1057
- /16/ J.C.Trombe, G.Montel
"Some features of the incorporation of oxygen in different oxidation states in the apatitic lattice-I : On the existence of calcium and strontium oxyapatite"
J.Inorg.Nucl.Chem 40(1978); 15-21
- /17/ J.C.Trombe, G.Montel
"Some features of the incorporation of oxygen in different oxidation states in the apatitic lattice-III: Synthesis and properties of some oxygenated apatites"
J.Inorg.Nucl.Chem 40(1978); 27-30
- /18/ P.Hartmann, C.Jäger, St.Barth, J.Vogel, K.Meyer
"Solid state NMR, X-ray diffraction, and infrared characterization of local structure in heat-treated oxyhydroxyapatite microcrystals: an analog of the thermal decomposition of hydroxyapatite during plasma-spray procedure"
J.Solid State Chem. 160(2001); 460-468
- /19/ Chun-Jen-Liao, Feng-Huei Lin, Ko-Shao Chen, Jui-Sheng Sun
"Thermal decomposition and reconstitution of hydroxyapatite in air atmosphere"
Biomaterials 20(1999); 1807-1813
- /20/ A.M.J.H.Seuter
"Existence region of calcium hydroxyapatite and the equilibrium with coexisting phases at elevated temperatures"
Reactivity of Solids, London, Chapman and Hall, 1972; 806-812
- /21/ R.Z.Le Geros, J.P.Le Geros
Phosphate Minerals
Edited by J.O. Nriagu and P.B. Moore, Springer Verlag, 1984

- /22/ B.V.Rejda, J.G.J.Peelen, K.de Groot
“Tricalcium phosphate as a bone substitute”
J. Bioeng 1(1977); 93-97
- /23/ R.A.Young, D.W.Holcomb
“Variability of hydroxylapatite preparations”
Calcif. Tissue Int. 34 (1982); Suppl 2; S17-S32
- /24/ Xilin Yin, M.J.Stott
“ α - and β - tricalcium phosphate: a density functional study”
Physical Review. B68(2003); 205205(1-8)
- /25/ T.Hattori, Y.Iwadata
“Hydrothermal preparation of calcium hydroxylapatite powders”
J.Am.Cer.Soc, 73(1990); 1803-1805
- /26/ K.Umatsu, M.Takagi, T.Honda, N.Uchida, K.Saito
“Transparent hydroxylapatite prepared by hot isostatic pressing of filter cake”
J.Am.Cer.Soc 72(1989); p.1476-1478
- /27/ J.M.Hughes, M.Cameron, K.D.Crowley
“Structural variations in natural F, OH, and Cl apatites”
Am.Min 74(1989); 870-876
- /28/ J.M.Hughes, M.Cameron, K.D.Crowley
“Crystal structures of natural ternary apatites: Solid solution in the $\text{Ca}_5(\text{PO}_4)_3\text{X}$ (X= F, OH, Cl) system”
Am.Min 75(1990); 295-304
- /29/ K.Sudarsanan, R.A.Young”
“Structural interactions of F, CL and OH in apatites”
Acta Crystallogr B34(1978); 1401-1407
- /30/ L.L.Hench, E.C.Ethridge
“Biomaterials: An interfacial approach”
Academic Press, Inc, New York, 1982
- /31/ Hsin-Yi Lin
“Short term observations of in vitro biocorrosion of two commonly used implant alloys”
PhD thesis, Department of Agricultural and Biological Engineering,
Mississippi State University, USA, 2002
- /32/ R.B.Heimann, T.A.Vu, M.L.Wayman
“Bioceramic coatings: state-of-the-art and recent development trends”
Eur.J.Mineral 9(1997); 597-615

- /33/ K.de Groot, C.P.A.T.Klein, J.G.C.Wolke, J.M.A.de Blicck-Hogervorst
“Plasma-sprayed coatings of calcium phosphate “
Handbook of Bioconductive Ceramics 1990, Vol. 2; 133-142
- /34/ Company brochure at www.haydencorp.com
- /35/ R.B.Heimann
“Plasma-Spray Coating: Principles and application”
VCH, Weinheim-New York- Basel- Cambridge- Tokyo, 1996
- /36/ K.S.Drellishak
Ph.D. Thesis, Northwestern University, Evanstown, IL, 1963
- /37/ M.Vardelle, A.Vardelle, P.Fauchais, M.I.Boulos
“Plasma-particle momentum and heat transfer, modelling and measurements”
AIChE J 29(1983); 236
- /38/ K.de Groot
“Degradable ceramics“
Biocompatibility of clinical implant materials Vol. 1(1981); 199-222
- /39/ J.Sodek, Q.Zhang, H.A.Goldberg, C.Domenicucci, S.Kasuga, J.L.Wrana, H.Shapiro, J.Chen
“Non-collagenous bone proteins and their role in substrate-induced bioactivity”
The Bone-Biomaterial Interface
J.E.Davies (ed)
University of Toronto Press: Toronto, Buffalo, London 1991; p.97
- /40/ S.D.Cook, K.A.Thomas, J.F.Kay, M.Jarcho
“Hydroxylapatite coated titanium for orthopaedic implant applications”
Clin.Orthop 232(1988); 225-243
- /41/ G.L.de Lange, K.Donath
“Interface between bone tissue and implants of solid hydroxylapatite or hydroxyapatite- coated titanium implants”
Biomaterials 10(1989); 121-125
- /42/ P.Ducheyne, K.E.Healy
“The effect of plasma-sprayed calcium phosphate ceramic coatings on the metal ion release from porous titanium and cobalt-chromium alloys”
J.Biomed.Mater.Res 22(1988); 1137-1163
- /43/ H.Ji, C.B.Ponton, P.M.Marquis
“Microstructural characterization of hydroxyapatite coating on titanium”
J.Mat.Sci:Mat.Med 3(1992); 283-287

- /44/ K.A.Khur, P.Cheng
“Characterization of plasma sprayed hydroxyapatite powders and coatings”
Proceedings of the National Thermal Spray Conference, Anaheim, CA, 7-11 June 1993; 347-352
- /45/ K.A.Gross, C.C.Berndt, D.D.Goldschlag, V.J.Iacono
“In vitro changes of hydroxyapatite coatings”
Int. J. Oral. Maxillofac Implants 12(1997); 589-597
- /46/ E.Park, R.A.Condrate, D.Lee, K.Kociba, P.K.Gallagher
“Characterization of hydroxylapatite: before and after plasma spraying”
J.Mat.Sci:Mat.Med 13(2002); 211-218
- /47/ P.Ducheyne, S.W.van Raemdonck, J.C.Heughebaert, M.Heughebaert
“Structural analysis of hydroxyapatite coatings on titanium”
Biomaterials 7(1986); 97-103
- /48/ P.Hartmann, St.Barth, J.Vogel, Ch.Jäger
“Investigations of structural changes in plasma-sprayed hydroxyapatite coatings”
Applied Mineralogy Vol.1; 147-150, Balkema, Rotterdam
Proc.6th Intern.Conf.Appl.Min.(ICAM), July 17-19, 2000, Göttingen, Germany
- /49/ R.McPherson, N.Gane, T.J.Bastow
“Structural characterization of plasma-sprayed hydroxyapatite coatings”
J.Mater.Sci:Mater.Med 6(1995); 327-334
- /50/ M.Weilaender, J.Beumer III, E.B.Kenney, P.K.Moy, F.Adar
“Raman microprobe investigation of the calcium phosphate phase of three commercially available plasma-flame-sprayed hydroxyapatite coated dental implants”
J.Mat.Sci:Mat.Med 3(1992); 397-401
- /51/ E.Park, R.A.Condrate SR, D.T.Hoelzer, G.S.Fischman
“Interfacial characterization of plasma-spray coated calcium phosphate on Ti-6Al-4V”
J.Mater.Sci:Mater.Med 9(1998); 643-649
- /52/ V.Palka, E.Postrkova, H.K.Koerten
“Some characteristics of hydroxyapatite powder particles after plasma spraying”
Biomaterials 19(1998); 1763-1772
- /53/ S.R.Randin, P.Ducheyne
“Plasma spraying induced changes of calcium phosphate ceramic characteristics and the effect on in vitro stability”
J.Mat.Sci:Mat.Med 3(1992); 33-42

- /54/ C.Y.Yang, B.C.Wang, E.Chang, J.D.Wu
 “The influence of plasma spraying parameters on the characteristics of hydroxyapatite coatings: A quantitative study”
 J.Mat.Sci:Mat.Med 6(1995); 249-257
- /55/ D.M.Liu, H.M.Chou, J.D.Wu
 “Plasma-sprayed hydroxyapatite coating: effect of different calcium phosphate ceramics”
 J.Mat.Sci:Mat.Med 5(1994); 147-153
- /56/ K.A.Gross, C.C.Berndt
 “In vitro testing of plasma-sprayed hydroxyapatite coatings”
 J.Mat.Sci:Mat.Med 5(1994); 219-224
- /57/ R.B.Heimann, O.Graßmann:
 ”Biomimetic processes during in vitro leaching of plasma-sprayed hydroxylapatite coatings for endoprosthetic applications”
 3rd Interdisc. Essen-Symposium 'Biomaterials: Fundamentals and Clinical Applications', Mat.-wiss. u. Werkstofftechn 32(2001); 913-921
- /58/ R.Y.Whitehead, L.C.Lucas, W.R.Lacefield
 “The effect of dissolution on plasma sprayed hydroxyapatite coatings on titanium”
 Clinical Materials 12(1993); 31-39
- /59/ J.Weng, Q.Liu, J.G.C.Wolke, X.Zhang, K.de Groot
 “Formation and characteristics of the apatite layer on plasma-sprayed hydroxyapatite coatings in simulated body fluid “
 Biomaterials 18(1997); 1027-1035
- /60/ J.Weng, Q.Liu, J.G.C.Wolke, D.Zhang, K.de Groot
 “The role of amorphous phase in nucleating bone-like apatite on plasma-sprayed hydroxyapatite coatings in simulated body fluid”
 J.Mat.Sci.Lett 16(1997); 335-337
- /61/ C.Y.Yang, R.M. Lin, B.C.Wang, T.M.Lee, E.Chang, Y.S.Hang, P.Q.Chen
 “In vitro and vivo mechanical evaluations of plasma-sprayed hydroxyapatite coatings on titanium implants: the effect of coating characteristics”
 J.Biomed.Mat.Res 37(1998); 335-345
- /62/ O.Graßmann
 “Herstellung biokeramischer Funktionsschichten und Schichtcharakterisierung nach Langzeitkontakt mit simulierter Körperflüssigkeit“
 Diplomarbeit, Institut für Mineralogie, TU Bergakademie Freiberg 1999

- /63/ P.Ducheyne, S.Radin, L.King
“The effect of calcium phosphate ceramic composition and structure on in vitro behaviour: Dissolution”
J.Biomed.Mat.Res 27(1993); 25-34
- /64/ D.I.Hay, E.C.Moreno
“Differential adsorption and chemical affinities of proteins for apatitic surfaces”
J.Dent.Res. (Special issue B) 58(B)(1978); 930-940
- /65/ A.Bennick, M.Cannon, G.Madapallimattam
“The nature of the hydroxyapatite-binding site in salivary acidic proline-rich proteins”
Biochem.J 183(1979); 115-126
- /66/ A.Bennick, D.Kells, G.Madapallimattam
“Interaction of calcium ions and salivary acidic proline-rich proteins with hydroxyapatite”
Biochem.J 213(1983); 11-20
- /67/ M.Johnsson, C.F.Richardson, E.J.Bergey, M.J.Levine, G.H.Nancollas
“The effects of human salivary cystatins and statherin on hydroxyapatite crystallization”
Archs.Oral.Biol 36(9)(1991); 631-639
- /68/ Y.Do, R.Okuda, Y.Takezawa et al.
“Osteonectin inhibiting de novo formation of apatite in the presence of collagen”
Calcified Tissue Int 44(1989); 200-208
- /69/ A.A.Campbell, A.Abrahimpour, L.Perez, S.A.Smesko, G.H.Nancollas
“The dual role of polyelectrolytes and proteins as mineralization promoters and inhibitors of calcium oxalate monohydrate”
Calcif.Tissue Int 45(1989); 122-128
- /70/ D.P.Rivero, J.Fox, A.K.Skipor, R.M.Urban, J.O.Galante
“Calcium phosphate coated porous titanium implants for enhanced skeletal fixation”
J.Biomed.Mater.Res 22(1988); 191-201
- /71/ J.A.Jansen, J.P.C.M.van der Waerden
“Histologic investigation of the biologic behaviour of different hydroxyapatite plasma-sprayed coatings in rabbits”
J.Biomed.Mater.Res 27(1993); 603-610
- /72/ K.A.Thomas, S.D.Cook, R.J.Haddad, J.F.Kay, M.J.Jarcho
“Biologic response to hydroxyapatite-coated titanium hips”
The Journal of Arthroplasty (1989); 43-53

- /73/ H.Caulier, S.Vercaigne, I.Naert, J.P.C.M.van der Waerden, J.G.C.Wolke, W.Kalk, J.A.Jansen
„The effects of Ca-P plasma-sprayed coating on the initial bone healing of oral implants: an experimental study in the goat“
J.Biomed.Mat.Res 34(1997); 121-128
- /74/ R.G.T.Geesink, K.de Groot, C.P.A.T.Klein
“Bonding of bone to apatite-coated implants“
J.Bone.Joint.Surg (Br) 70-B(1988); 17-22
- /75/ H.Oonishi, H.Ishimaru, M.Yamamoto, E.Tsuji, S.Kushitani, M.Aono, T.Nabeshima
“Comparison of bone ingrowth into porous Ti-6Al-4V beads with and without a plasma spray hydroxyapatite coating“
CRC Handbook of bioconductive ceramics, Wilson; Vol. II; 1990; 155-162
- /76/ W.Xue, S.Tao, X.Liu, X.Zheng, C.Ding
“In vivo evaluation of plasma sprayed hydroxyapatite coatings having different crystallinity“
Biomaterias 25(2004); 415-421
- /77/ L.Claes, H.J.Wilke, H.Kiefer, A.Meschenmoser
“Bone defect bridging with different implant materials”
CRC Handbook of Bioconductive Ceramics, Wilson; Vol. II; 1990; 77-86
- /78/ M.Weilaender, E.B.Kenney, V.Lekovic, J. Beumer III, PK.Moy, S.Lewis
“Histomorphometry of bone apposition around three types of endosseous dental implants“
Int.J.Oral Maxillofac Implants 7(1992); 491-496
- /79/ M.Gottlander, T.Alberektsen
“Histomorphometric analyses of hydroxyapatite-coated and uncoated titanium implants. The importance of the implant design”
Clin.Oral.Imp.Res 3(1992); 71-76
- /80/ F.Lintner, G.Böhm, M.Huber, R.Scholz
“Ist nach Verlust der Hydroxylapatitbeschichtung bei totalen Hüftendoprothesen nach mehrjähriger Liegezeit eine Knochenneubesiedelung der Titanlegierungs Oberfläche möglich?“
Osteologie 10(1) (2001); 40 – 53
- /81/ F.Brossa, A.Ciagada, R.Chiesa, L.Paracchini, C.Consonni
“Post-deposition treatment effects on hydroxyapatite vacuum plasma spray coatings”
J.Mat.Sci:Mat.Med 5(1994); 855-857

- /82/ B.C.Wang, E.Chang, T.M.Lee and C.Y.Yang
“Changes in phases and crystallinity of plasma-sprayed hydroxyapatite coatings under heat treatment: a quantitative study”
J.Biomed.Mat.Res 29(1995); 1483-1492
- /83/ M.J.Filiaggi, R.M.Pilliar and N.A.Coombs
“Post-plasma-spraying heat treatment of the HA coating/Ti-6Al-4V implant system”
J.Biomed.Mat.Res 27(1993); 191-198
- /84/ J.Wang, X.G.Liu, X.D. Li, X.D.Zhang
“Intrinsic factor of apatite influencing its amorphization during plasma-spray coating”
Biomaterials 16(1995); 39-44
- /85/ H.Kurzweg, R.B.Heimann, T.Troczynski, M.L.Wayman
“Development of plasma-sprayed bioceramic coatings with bond coats based on titania and zirconia”
Biomaterials 19(1998); 1507-1511
- /86/ B.-Y.Chou, E.Chang
“Plasma-sprayed zirconia bond coat as an intermediate layer for hydroxyapatite coating on titanium alloy substrate”
J.Mat.Sci:Mat.Med 13(2002); 589-595
- /87/ R.B.Heimann
“Recent trends towards improved plasma-sprayed advanced bioceramic coatings on Ti6Al4V”
Mat.-wiss. u. Werkstofftech 30 (1999); 775-782
- /88/ C.C.Ribeiro, M.A.Barbosa, A.A.S.C.Machado, A.tudor, M.C.Davies
“Modification in the molecular structure of hydroxyapatite induced by titanium ions”
J.Mat.Sci:Mat.Med 6(1995); 829-834
- /89/ S.R.Sousa, M.A.Barbosa
“The effect of hydroxyapatite thickness on metal ion release from stainless steel substrates”
J.Mat.Sci:Mat.Med 6(1995); 818-823
- /90/ H.Kurzweg, R.B.Heimann, T.Troczynski
“Adhesion of thermally sprayed hydroxyapatite-bond coat systems measured by a novel peel test”
J.Mater.Sci:Mater.Med 9(1998); 9-16

- /91/ H.Hildebrandt
“Charakterisierung des Resorptionsverhaltens plasmagespritzter dotierter biokeramischer Schichten beim Kontakt mit protein-freier simulierter Körperflüssigkeit (pf-SBF) “
Diplomarbeit, Institut für Mineralogie, TU Bergakademie Freiberg, 2000
- /92/ J.Götze, H.Hildebrandt, R.B.Heimann
“Charakterisierung des in-vitro-Resorptionsverhaltens von plasmagespritzten Hydroxylapatit-Schichten“
Biomaterialien 2(2001); 54-60
- /93/ H.M.Kim, T.Miyazaki, T.Kokubo, T.Nakamura
“Revised simulated body fluid”
Bioceramics 13(2001); 47-50
- /94/ H.M.Kim, K.Kishimoto, F.Miyaji, T.Kokubo, T.Yao, Y.Suetsugu, J.Tanaka, T.Nakamura
“Composition and structure of apatite formed on organic polymer in simulated body fluid with a high content of carbonate ion”
J.Mater.Sci:Mater.Med 11(2000); 421-426
- /95/ B.Kasemo
“Biocompatibility of titanium implants: surface science aspects”
J.Prosth.Dent 49(1983); 832
- /96/ T.A.Vu, R.B.Heimann
“Influence of the CaO/TiO₂ ratio on thermal stability of hydroxylapatite in the system Ca₅(PO₄)₃OH-CaO-TiO₂”
J.Mater.Sci.Lett 16(1997); 1680-1682
- /97/ H.Friebolin
“One and two dimensional NMR spectroscopy “
Wiley-VCH,1999
- /98/ E.R.Andrew, A.Bradbury, R.G.Eades
“Nuclear magnetic resonance spectra from a crystal rotated at high speed”
Nature 182(1958); 1659
- /99/ J.Keeler
Lectures by James Keeler “Understanding NMR spectroscopy”
<http://www-keeler.ch.cam.ac.uk/lectures/>
- /100/ R.A.Kellner, M.Otto, J.-M.Mermet, H.M.Widmer
“Analytical chemistry”
Wiley-VCH, Weinheim – Berlin – New York - Chichester – Brisbane – Singapore – Toronto, 1998

- /101/ K.E.Zeigler, R.J.Lascola, L.L.Tovo
"Fiber-optic Laser Raman Spectroscopy sensor"
Westinghouse Savannah River Company, Aiken, SC 29808, June 2003
- /102/ B.Schrader
„Infrared and Raman spectroscopy: methods and application“
VCH, Weinheim-Basel-Cambridge-New York, Tokyo, 1995
- /103/ D.A.Skoog, J.J.Leary
"Principles of instrumental analysis"
Saunders College Publishing, New York, 1992
- /104/ B.Koch, J.G.C.Wolke, K.de.Groot
"X-ray diffraction studies on plasma-sprayed calcium phosphate-coated implants"
J.Biomed.Mat.Res 24(1990); 655-667
- /105/ DIN 51007 Ausgabe:1994-06
Thermische Analyse (TA); Differenzthermoanalyse (DTA); Grundlagen
- /106/ R.W.Cahn, P.Haasen, E.J.Kramer
"Materials science and technology: A comprehensive treatment "
Vol.2A, Characterization of materials
VCH, Weinheim-New York-Basel-Cambridge 1992
- /107/ A.Gucsik, Ch.Koebert, E.Libowitzky, W.U.Reimold
"Scanning electron microscopy, cathodoluminescence, and Raman spectroscopy of experimentally shock metamorphosed quartzite"
Lunar and Planetary Sci. XXXIV (2003)
- /108/ J.Götze
"Cathodoluminescence microscopy and spectroscopy in applied mineralogy"
Freiberger Forschungshefte / C 485, TU Bergakademie Freiberg,
Habilitationsschr., 2000
- /109/ J.M.Houben
"Relation of the adhesion of plasma sprayed coatings to the process parameters size, velocity and heat content of the spray particles"
Doctoral thesis, TU Eindhoven, The Netherlands, 1988
- /110/ W.P.Aue, A.H.Roufosse, M.J.Glimcher, R.G.Griffin
"Solid-state phosphorous-31 nuclear magnetic resonance studies of synthetic solid phases of calcium phosphate: potential models of bone mineral"
Biochemistry 23(1984); 6110-6114
- /111/ J.Weng, X.Liu, X.Zhang, K.de Groot
"Integrity and thermal decomposition of apatite in coatings influenced by underlying titanium during plasma spraying and post-heat-treatment."
J.Biomed.Mat.Res 30(1996); 5-11

- /112/ W.A.House
“The physico-chemical conditions for the precipitation of phosphate with calcium”
Environ.Technol., 20 (1999), 727-733
- /113/ R.Cusco, F.Guitian, S.de Aza, L.Artus
“Differentiation between hydroxyapatite and β -tricalcium phosphate by means of μ -Raman spectroscopy”
J.Eur.Ceram.Soc 18(1998); 1301-1305
- /114/ Z.Iqbal, V.P.Tomaselli, O.Fahrenfeld, K.D.Möller, F.A.Ruszala, E.Kostiner
“Polarized Raman scattering and low frequency infrared study of hydroxylapatite”
J.Phys.Chem.Solids 38(1977); 923-927
- /115/ B.O.Fowler
“Infrared studies of apatite. I. Vibrational assignments for calcium, strontium, and barium hydroxyapatite utilizing isotopic substitution”
Inorganic Chemistry 13(1973); 194-207
- /116/ Professor Gert Irmer, Department of Theoretical Physics, TU Bergakademie Freiberg, personal communication
- /117/ D.G.A.Nelson, B.E.Williamson
“Low-temperature laser Raman spectroscopy of synthetic carbonated apatites and dental enamel”
Aust.J.Chem 35(1982); 715-727
- /118/ F.F.M.de Mul , M.H.J.Hottenhuis, P.Bouter, J.Greve, J.Arends, J.J.Bosch
“Micro-Raman line broadening in synthetic carbonated hydroxyapatite”
J.Dent.Res 65(1986); 437-440
- /119/ K.de Groot
“Medical applications of calcium phosphate bioceramics”
J.Cer.Soc.Japan 10(1991); 917 – 926
- /120/ H.Keller
“Biokompatible Werkstoffe: Herstellung und Charakterisierung von plasmagespritzten Hydroxylapatitschichten auf Femurschäften von Titan-Hüftprothesen“
Dissertation thesis 1992, Tübingen
- /121/ Handbook of Chemistry and Physics
74th Edition, CRC press, Boca Raton, FL, 1993/1994; 4-31

- /122/ R.Z.LeGeros, I.Orly, M.Gregoire, G.Daculsi
“Substrate surface dissolution and interfacial biological mineralization”
The Bone-Biomaterial Interface
J.E.Davies (ed)
University of Toronto Press: Toronto, Buffalo, London 1991; p.26
- /123/ F.Abbona
“Crystallization of calcium and magnesium phosphates from solutions of low concentration”
J.Cryst.Growth 104(1990); 661-671
- /124/ H.Zeng, K.K.Chittur, W.R.Lacefield
“Dissolution/ reprecipitation of calcium phosphate thin film produced by ion beam sputter deposition technique”
Biomaterials 20(1999); 443-451
- /125/ J.A.M.van der Houwen, E.Valsami-Jones
“The application of calcium phosphate precipitation chemistry to phosphorus recovery: the influence of organic ligands”
Environ.Technol 22 (2001); 1325-1335
- /126/ S.A.Bender, J.D.Baumgardner, M.D.Roach, K.Bessho, J.L.Ong
“Effect of protein on the dissolution of HA coatings”
Biomaterials 21(2000); 299-305
- /127/ K.A.Gross, C.C.Berndt
“Thermal processing of hydroxyapatite for coating production”
J.Biomed.Mat.Res 39(1998); 580-587
- /128/ J.F.Shackleford, W.Alexander, J.S.Park,
The CRC Materials Science and Engineering Handbook
CRC Press, April, 1994; p.284
- /129/ www.azom.com; Azom home – metals ceramics, polymers, composites
- /130/ R.B.Heimann, H.Kurzweg, T.A.Vu
“Hydroxylapatite –bond coat systems for improved mechanical and biological performance of hip implants”
Proceedings of the 15th International Thermal Spray Conference 25-29 May 1998, Nice, France; 999-1005
- /131/ H.H.Moroi, K.Okimoto, R.Moroi, Y.Terada
“Numeric approach to the biomechanical analysis of thermal effects in coated implants”.
Int.J.Prostodont 6(1993);564-572.

- /132/ J.Vogel, C.Rüssel, G.Günther, P.Hartmann, F.Vizethum, N.Bergner
 “Characterization of plasma-sprayed hydroxyapatite by ^{31}P -MAS-NMR and the effect of subsequent annealing”
 J.Mater.Sci:Mater.Med 7(1996); 495-499
- /133/ J.Weng, Y.Cao, J.Chen, X.Zhang
 “Significance of water promoting amorphous to crystalline conversion of apatite in plasma sprayed coatings”
 J.Mat.Sci.Lett 14(1995); 211-213
- /134/ K.de Groot
 “Die klinische Anwendbarkeit von Calciumphosphat-Keramiken“
 Zahnärztl. Mitt 75(1985); 1938
- /135/ B.Barden
 “Failure mechanisms in total hip and knee arthroplasty”
 Proc. 1st Essen Symposium ‘Biomaterials: Fundamentals and Clinical Appl.’,
 Essen, Germany, Oct. 8-9. 1998, p.44
- /136/ P.V.Riboud
 “Composition et stabilité des phase à structure d’apatite dans le système
 CaO-P₂O₅-oxide de fer-H₂O à haute temperature”
 Ann.Chim 8 (1973); 381
- /137/ G.Daculsi, J.M.Bouler
 “Bone bioconductive ceramic interface: a dynamic process”
 Knochenersatzmaterialie und Wachstumsfaktoren
 Georg Thieme Verlag: Stuttgart, New York 1997; p.23
- /138/ J.Beight, S.Radin, J.Cuckler, P. Ducheyne
 “Effect of solubility of calcium phosphate coatings on mechanical fixation of porous ingrown implants”
 Trans.35th Annual Meeting Orthop.Res.Soc 14(1989); 334
- /139/ A.P.M.Kentgens
 “A practical guide to solid-state NMR of half integer quadrupolar nuclei with some applications to disordered systems”
 Geoderma 80(1997); 271-306
- /140/ R.B.Heimann
 “Modern Bioceramic Materials: Design, Testing and Clinical Application”
 Engineering Mineralogy of Ceramic Materials. Proceedings of the
 International School Earth and Planetary Sciences. Siena 2002; 117-134
- /141/ O.Graßmann, R.B.Heimann
 “Compositional and microstructural changes of engineered plasma-sprayed hydroxylapatite coatings on Ti6Al4V substrates during incubation in protein-free simulated body fluid”
 Biomed.Mater.Res.; Appl. Biomater. 56(2000); 685-693

- /142/ R.B.Heimann, H.V.Tran, P.Hartmann
“Laser-Raman and Nuclear Magnetic Resonance (NMR) studies on plasma-sprayed hydroxyapatite coatings: Influence of bioinert bond coats on phase composition and resorption kinetics in simulated body fluid”
Materialwissenschaft und Werkstofftechnologie, in the press.

8 Curriculum vitae

Name: Thi Hong Van TRAN

Date of birth: 16.07.1970 in Hanoi, Vietnam

Citizenship: Vietnamese

Family status: Married

1976-1989 Public school and High school in Hanoi, Vietnam

1989-1994 Study of construction materials at the University of Civil Engineering of Hanoi, Vietnam.

"Dipl.-Eng."

1995-1999 Work in Thanh Tri Sanitary Ware company, Hanoi, Vietnam

2000-2001 Work in Construction and Building material development consultants company, Hanoi, Vietnam

2001- 2004 PhD Thesis "Investigation into the thermal dehydroxylation and decomposition of hydroxylapatite during atmospheric plasma spraying: NMR and Raman spectroscopic study of as-sprayed coatings and coatings incubated in simulated body fluid" with Prof.Dr. R.B.Heimann at the Department of Mineralogy, TU-Bergakademie Freiberg

11th.Feb.2005 Oral presentation of the doctoral thesis